ISSN 1000-9620

海洋通报

Marine Science Bulletin

NATIONAL MARINE DATD AND
INFORMATION SERVICE OF CHINA

2012
Volume 14
Number 2

NOAA
U.S. DEPARTMENT OF COMMERCE
NATIONAL OCEANIC AND ATMOSPHERIC ADMINISTRATION

LIBRARY
APR 10 2013
National Oceanic & Atmospheric Administration
U.S. Dept. of Commerce

MARINE SCIENCE BULLETIN

Vol. 14 No. 2 Oct. 2012

CONTENTS

Preliminary analysis on the interdecadal variation characteristics of typhoon over the Northwestern Pacific in the past sixty years ····· YU Fan et al. (03)

Internal tides in the northern South China Sea from 20-day in-situ mooring observations in 1998 ····· CAI Yang et al. (12)

Comparison of spectral partitioning techniques for wind wave and swell ·····LI Shui-qing et al. (24)

Analysis of tidal and residual currents across semi-enclosed bay mouth based on shipboard ADCP measurements ·····LI Xi-bin et al. (37)

An approach to estimate tidal dissipation with single-point high-frequency ground wave radar data ····· MAO Hua-bin et al. (46)

Distribution of clay minerals in surface sediments off Yangtze River estuary ····· LAN Xian-hong et al. (56)

Changes in magnetic susceptibility and grain size of Holocene sediments of the Pearl River estuary and climate changes reflected by them ····· CAO Ling-long et al. (70)

Correction of seabed layer thickness in processing the subbottom profile data ·····WANG Fang-qi et al. (83)

LIBRARY
Pacific Islands Fisheries Science Center
NOAA Fisheries
Honolulu, Hawai'i

海 洋 通 报（英文版）

HAIYANG TONGBAO

2012 年 10 月 第 14 卷 第 2 期

目 次

近 60 年西北太平洋台风年代际变化特征及成因的初步分析…… 余 帆 等 (11)

1998 年南海北部 20 天定点连续观测的内潮分析 …… 蔡 扬 等 (23)

风浪和涌浪分离方法的比较 …… 李水清 等 (36)

基于船载 ADCP 观测对半封闭海湾湾口断面潮流及余流的分析 …… 李希彬 等 (45)

单点高频地波雷达资料估算潮能耗散的方法 …… 毛华斌 等 (55)

长江口外表层沉积物黏土矿物分布特征…… 蓝先洪 等 (69)

珠江口全新世沉积物粒度与磁化率的变化特征及其所反映的气候环境变化

…… 曹玲珑 等 (82)

浅地层剖面资料处理中的地层厚度校正 …… 王方旗 等 (96)

Preliminary analysis on the interdecadal variation characteristics of typhoon over the Northwestern Pacific in the past sixty years

YU Fan, ZHANG Tao, LI Pei, LI Xiang-jun

Navy Oceanic Hydrometeorological Center, Beijing 100161, *China*

Abstract: Using typhoon data over the Northwestern Pacific (NWP) in 60 years (1950-2009), the interdecadal variations of typhoon frequency, track and intensity are statistically analyzed. The results showed that the frequency of typhoon over the NWP was high in 1960s and low in 1970s. From the late 1990s, the frequency is low again. The track of typhoon was mainly shifting, and the average track was at the southern NWP in 1960s and 1970s, but in recent 10 years, the track was at the northern NWP. The intensity of typhoon was strong in 1950s and 1960s, but becomes weak in recent 25 years. In high frequency periods of typhoon, the subtropical high of NWP was weak and its position appears easternly. The distribution of Sea Surface Temperature (SST) shows characteristics of "La Nina" event. In low frequency periods of typhoon, the subtropical high of NWP is strong and its position appears westernly. The distribution of SST shows characteristics of "El Nino" event.

Keywords: typhoon over the NWP; frequency; track; intensity; interdecadal variation characteristics

1 Introduction

Tropical cyclone is one of the most important weather systems over the tropical ocean. It is very devastating, especially typhoon (wind speed exceeding 32.7 m/s). Because its intensity is strong and influence time is long, it often causes life lost and economic loss. The Northwestern Pacific (NWP) is the main source of the tropical cyclone, and China is the country which suffers the catastrophic natural phenomena. So it is important to forecast the typhoon activity by studying the variation rule of typhoon and mastering the characteristics [1-2].

Received on July 26, 2012

Corresponding author: yufannavy@sina.com

2 Data description

According to the intensity, the tropical cyclones include tropical depression(TD), tropical storm(TS),strong tropical storm(STS),typhoon(TY), strong typhoon(STY) and Super typhoon(Super TY). In this paper, typhoon means the strong tropical cyclone whose wind speed exceeds 32.7 m/s. Most data used in this paper come from the tropical cyclone annual of CMA (1950-2009), others from climate report of NCC.

3 Interdecadal statistical analysis of typhoon over the NWP

3.1 Interdecadal variation of typhoon frequency over the NWP

The number of typhoon was 1012 over the NWP in the year 1950 - 2009, average number was 17. The maximum was 25(1967 and 1971); the minimum was 6(1998 and 1999). The frequency of typhoon over the NWP was high in 1960s, having positive anomalies in sequential 9 years (1960 - 1968); the frequency of typhoon over the NWP was low in 1970s, having negative anomalies in 7 years. From the early 1990s, the frequency was high, but in the late 1990s, the frequency was low again. The running average lines show that the frequency has a slow interdecadal variation. It was top in 1960s; bottom from 1970s; top in early 1990s ; bottom from late 1990s again.

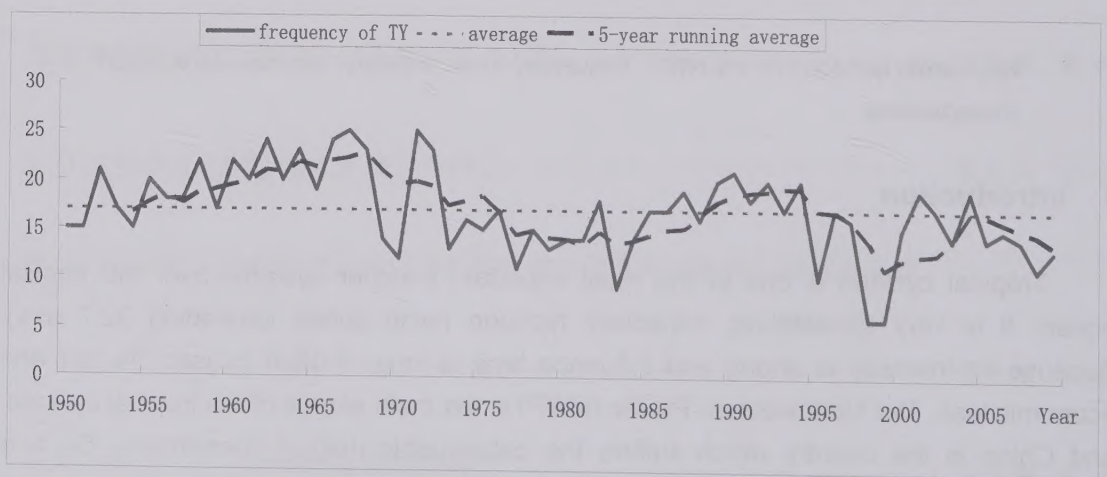

Fig. 1 Annual variation of typhoon frequency over the NWP in 1950 - 2009

3.2 Interdecadal variation of typhoon source over the NWP

Fig. 2 shows that the number of typhoon is increasing near the middle of Pacific Ocean in recent 30 years. The distribution looks more dispersed. For understanding the

distribution of typhoon source well, we analyze from latitude and longitude respectively. Fig. 3a shows typhoon source focuses on the area between 135° - 154°E from longitude, and the number is almost over 20 except 141°E; Fig. 3b shows typhoon source focuses on the area between 7°-19°N from latitude, and the number is over 40. So we believe that the main area of typhoon source locates at 135°-154°E and 7° - 19°N (the shadow of Fig. 4), with the typhoon frequency in the area accounting for half of total.

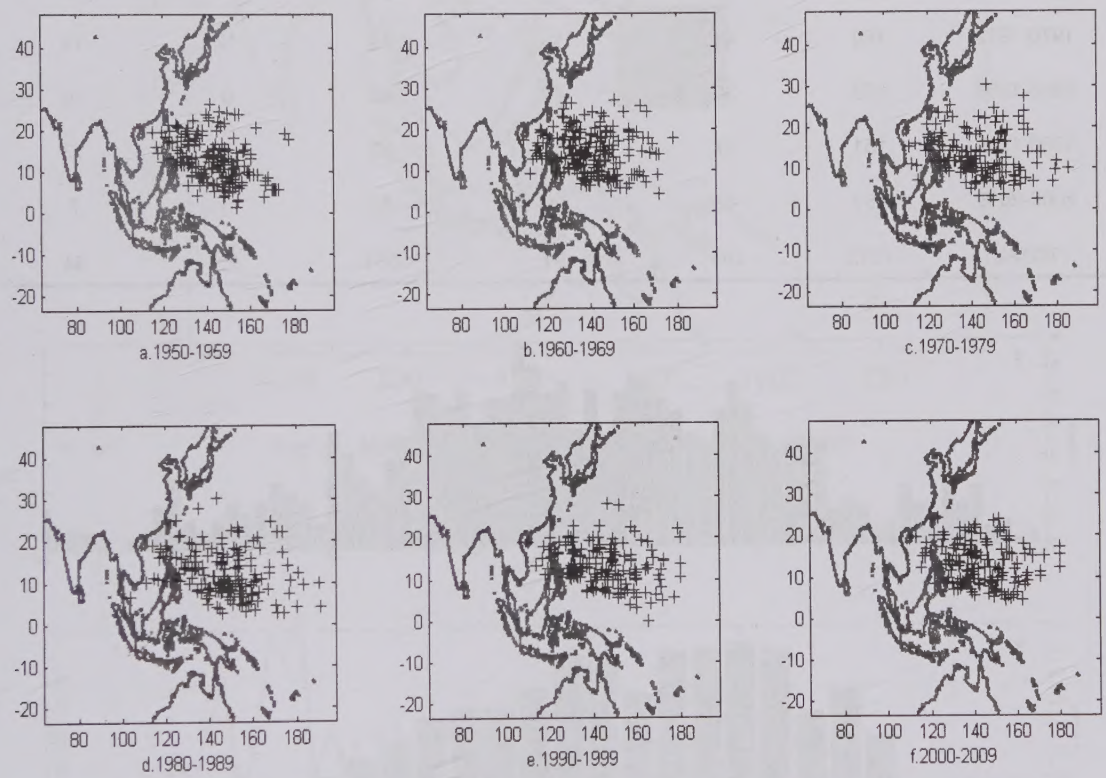

Fig. 2 Interdecadal variation of typhoon source over the NWP in 1950 - 2009

3.3 Interdecadal variation of typhoon track over the NWP

The tracks of typhoon over the NWP mainly include western track, northwestern track and shifting track (Fig. 4 shows).The typhoon of South China Sea is classified as SCS track alone. Other tracks such as Eastern track, snake track and turning track are classified as others.

Tab. 1 shows the distribution of typhoon track over the NWP in recent 60 years. The track of typhoon is mainly shifting, accounting for 52% of all. In 1960s and 1970s the typhoon number of western and SCS track was more, but in recent 10 years the number of northwestern track was relatively more. This shows the average track was at the southern NWP in 1960s and 1970s, but in recent 10 years, the track is at the northern NWP.

Tab. 1 Distribution of typhoon track over the NWP in 1950 - 2009

	number	western	northwestern	shifting	SCS	others
1950-1959	178	39	17	94	6	22
1960-1969	214	50	19	112	16	18
1970-1979	160	47	13	74	12	14
1980-1989	158	39	11	82	6	20
1990-1999	151	37	11	83	7	13
2000-2009	151	32	20	86	6	7
TOTAL	1012	244	91	531	53	94

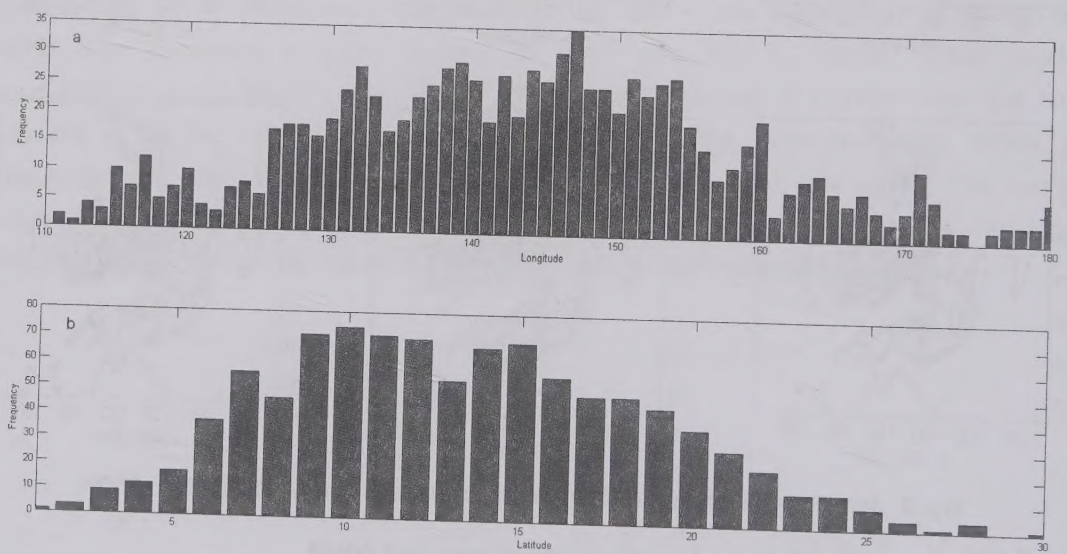

Fig. 3 Distribution of typhoon frequency over the NWP

3.4 Interdecadal variation of typhoon intensity over the NWP

Fig. 5 shows the intensity of typhoon was strong over the NWP in 1950s and 1960s, as a whole was weak in 1970s, and in the early 1980s, the intensity became little strong again, from the middle 1980s, the intensity was weak all the time. But in recent 10 years the intensity was increasing gradually. There was research before that and because of the limitation of typhoon observation technology in 1950s and 1960s, the maximum wind speed had errors[3].So it needs more studies to clarify that the intensity variation of Fig. 5 in 1950s and 1960s was natural variation or was caused by observation technology.

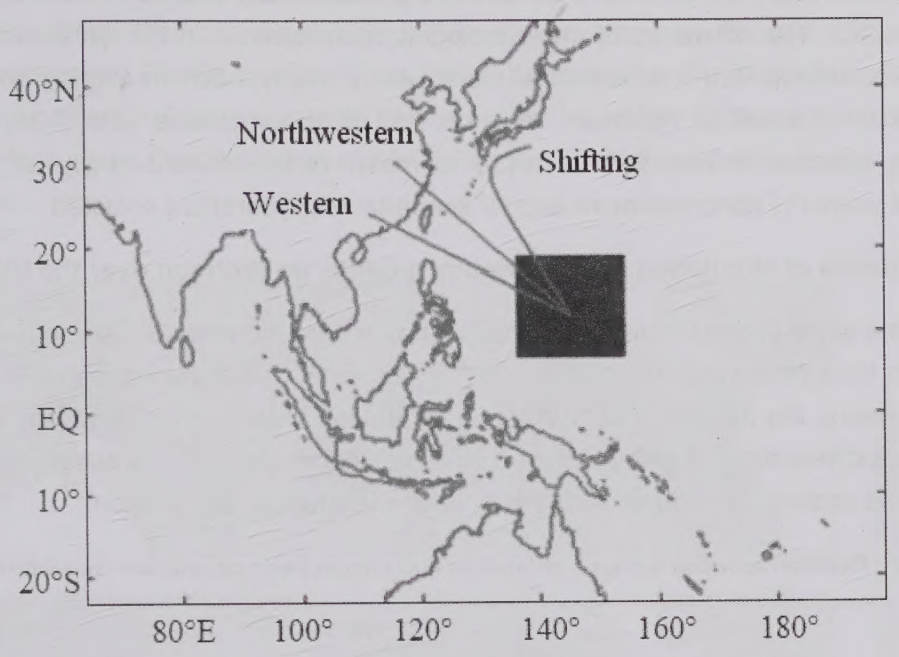

Fig. 4 Main area of typhoon source over the NWP

(which the shadow area shows)

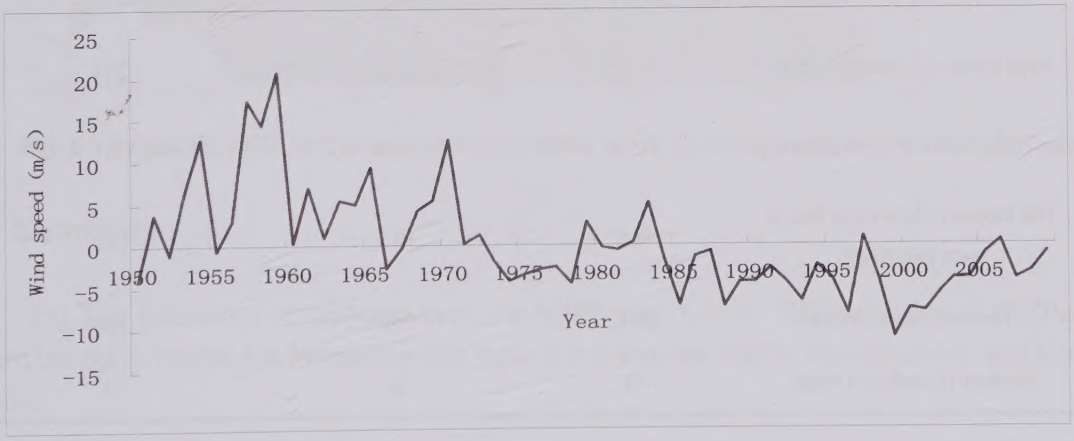

Fig. 5 Annual average maximum wind speed anomalies over the NWP in 1950 - 2009

4 Relation between the anomaly of NWP typhoon and the factors of large-scale circulation

Among the factors affecting the NWP typhoon, the large-scale circulation factors, such as western Pacific subtropical high, intertropical convergence zone (ITCZ), SST in the

Pacific Ocean, et al., are the most important and primary. Many studies [8-9] have been done in this respect. The difference of these factors is more obvious in the typhoon abnormal years. It is defined that it is abnormal-more year if the typhoon frequency anomaly is greater than or equal to the mean variance, and is abnormal-less year if the typhoon frequency anomaly is less than or equal to mean variance. Accordingly, 21 typhoon abnormal years (11 abnormal-more and 10 abnormal-less years) are selected.

4.1 Influence of circulation characteristics quantity on typhoon over the NWP

Some atmospheric circulation characteristics indices are selected, which are in close relation to the typhoon over the NWP. It can be seen from Tab. 2, during the NWP typhoon anomaly years, the difference of NWP subtropical high index is more obvious, while the other index difference is smaller. In abnormal-more year of typhoon, the subtropical high is weaker and eastern; while in abnormal-less year, it is stronger and western.

Tab. 2 Relation between typhoon anomalies and atmospheric circulation characteristics

	average	abnormal-more (11 years)	abnormal-less (10 years)
Frequency	17	23	10
Intensity index of subtropical high	335	250	451
Area index of subtropical high	188	148	234
West ridge point of subtropical high	117.8	126.4	111
The location of the ridge line of subtropical high	18.6	18.5	19.1
Tibetan Plateau index	551	552	553
Southern Oscillation Index	-17	3	-1

4.2 Influence of SST on typhoon over the NWP

Typhoon activity is closely related to the tropical large-scale circulation. El Nino event is a strong signal of the atmospheric circulation and climate change, which affects inevitably on the typhoon activity anomaly. Since the 1980s, lots of in-depth studies[4-7] had been carried out in Pacific SST and the NWP typhoon, which showed that in El Nino years typhoon frequency was less than normal, while in La Nina years, more than normal.

It can be seen from synthetic SSTA (Fig. 6), the SST is the anti-phase distribution

during the typhoon anomaly years. In typhoon abnormal-more years, the SST in the eastern equatorial Pacific is lower than that in the normal year, and the SST over the middle and western Pacific is higher than that in the normal year, and the distribution of SST over the Pacific Ocean is similar to that in the " La Nina " year; while in typhoon abnormal-less years, the distribution of SST in the Pacific Ocean is similar to that in the " El Nino " year.

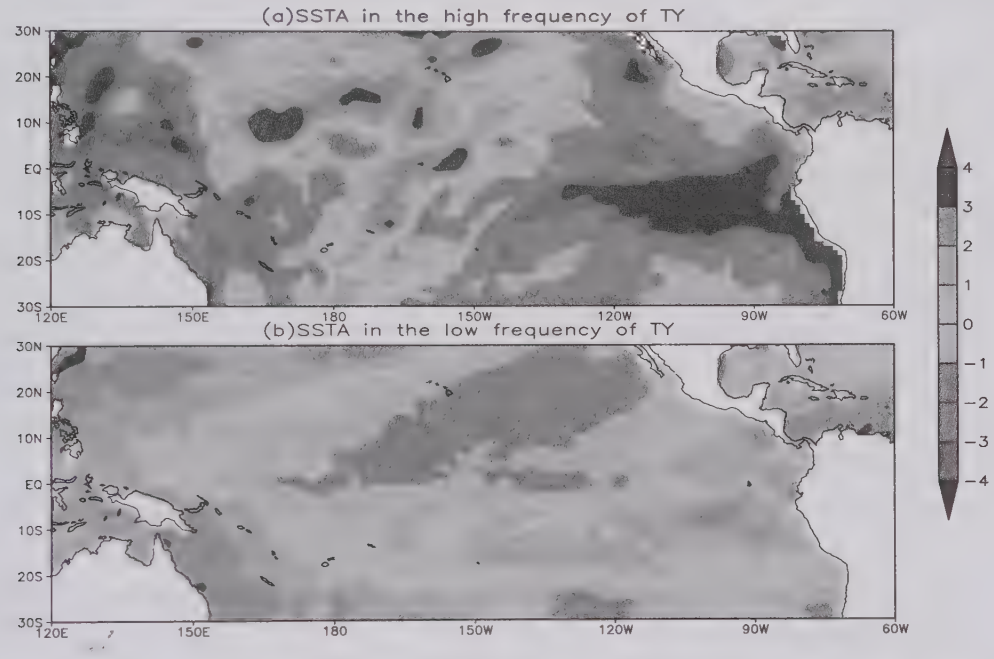

Fig. 6 Synthetic SSTA in typhoon abnormal-more years (a) and abnormal-less years (b)

5 Summary

(1) The frequency of typhoon over the NWP was high in 1960s and low in 1970s. From the early 1990s, the frequency was high, but in the late 1990s, the frequency was low again.

(2) The main area of typhoon source locate at 135° - 154°E and 7° - 19°N, and the typhoon frequency in the area accounts for half of total.

(3) The track of typhoon was mainly shifting, the average track was at the southern NWP in 1960s and 1970s, but in recent 10 years, the track was at the northern NWP.

(4) The intensity of typhoon was strong in 1950s and 1960s; became weak in recent 25 years. But in recent 10 years, the intensity was increasing gradually.

(5) In high frequency periods of typhoon, the subtropical high of NWP is weak and its position appears easterly. The distribution of SST shows characteristics of "La Nina" event. In low frequency periods of typhoon, the subtropical high of NWP is strong and its position appears westerly. The distribution of SST shows characteristics of "El Nino" event.

References

[1] Chen M, Zheng Y G, Tao Z Y. Climatological characteristics reanalysis of tropical cyclone over the Northwestern Pacific about 50 years (1949 - 1996) [J]. J. T. Meteor., 1999, 15(1): 10 - 16.

[2] Chen L S, Meng Z Y. An overview on tropical cyclone research progress in China during the past ten years [J]. J. Atmos. Sci., 2001, 25(3): 420 - 432.

[3] Chen X Z. Some climatological characteristics of tropical cyclone intensity over the Northwestern Pacific [J]. Marine Science Bulletin, 1997, 16(4): 16 - 25.

[4] Li C Y. Typhoon activity in the Northwestern Pacific in relation to El Nino event [J]. Science Bulletin, 1985, 14: 1 087 - 1 089.

[5] He M, Song W L, Chen X F. Typhoon activity in the Northwestern Pacific in relation to El Nino/ La Nina events [J]. J. T. Meteor., 1999, 15(1): 17 - 25.

[6] Lu Q Z, Hu B H, Wang X Z, et al. Large scale circulation associated with interdecadal variations of typhoon activity over the NorthPacific [J].J. T. Meteor., 2007, 23(6): 629 - 635.

[7] Wu G X. Tropical Storm Formation in response to sea surface temperature anomaly [J]. J. Atmos. Sci., 1992, 16(3): 322 - 332.

[8] Ye Y, Dong B. Interannual change of the severe tropical cyclone activities over the Northwest Pacific [J]. Meteor. Mon., 1998, 24(7): 29 - 34.

[9] Zhang G Z, Zhang X G, Wei F Y. A study on the variations of annual frequency for tropical cyclone in Northwest Pacific during the last hundred years [J]. J. T. Meteor., 1995, 11(4): 315 - 323.

近60年西北太平洋台风年代际变化特征及成因的初步分析

余 帆，张 涛，李 培，李向军

（海军海洋水文气象中心，北京 100161）

摘 要：利用60年台风资料，对西北太平洋台风的频数、路径和强度变化做统计分析。结果表明：西北太平洋的台风活动在20世纪60年代是高峰期，70年代则是低谷期，从20世纪90年代后期开始，台风活动总体处于低谷期；台风路径主要以转向为主，在20世纪60、70年代平均路径比较偏南，而进入21世纪后平均路径比较偏北；强度在20世纪50、60年代总体较强，后25年总体较弱；西北太平洋台风异常偏多时，西北太平洋副高弱且位置偏东，太平洋海温分布呈“拉尼娜”特征；台风异常偏少时，副高强且位置偏西，太平洋海温分布呈“厄尔尼诺”特征。

关键词：西北太平洋台风；频数；路径；强度；年代际

Internal tides in the northern South China Sea from 20-day in-situ mooring observations in 1998

CAI Yang[1], GUO Pu[2*], FANG Wen-dong[2]

1. *South China Sea Marine Prediction Center of SOA, Guangzhou* 510300, *Guangdong province, China*

2. *State Key Laboratory of Tropical Oceanography, South China Sea Institute of Oceanology, Chinese Academy of Sciences, Guangzhou* 510301, *Guangdong province, China.*

Abstract: 20-day in-situ ADCP current and CTD data are used to investigate the characteristics and energy of the internal tides in the northern South China Sea (NSCS). The results show that the O_1, K_1, M_2 and S_2 constituents of internal tides are energetic and diurnal constituents (O_1 and K_1) are dominating. In the observational period, the current vectors of these four constituents all rotate clockwise and the maximum semi-major axe of internal tidal ellipses is more than 14 cm/s. The variation of ocean temperature shows that the internal tides present obvious quasi-diurnal oscillation and the average amplitude reaches 50 m. Furthermore, these internal tides carry high energy and appear to be intermittent. The maximum values of KE (PE) during the observational period are up to 2 (3.5) kJ/m^2 for diurnal internal tides, and up to 1 (1.5) kJ/m^2 for semidiurnal internal tides.

Keyword: internal tides; in-situ mooring observations; northern South China Sea; energy

1 Introduction

Internal tides in the ocean are internal gravity waves with tidal period that have been observed on the continental shelf and slope [1-5]. Strong internal tides contribute to the ocean mixing and ocean circulation through the propagation and dissipation of their baroclinic energy. Therefore, the distribution of nutrient and the ecological environment in the ocean are influenced by the internal tides which pass through [6-8].

Internal tides with large amplitude are often observed by remote sensing data [9-11] and in-situ observations [12-15] in the northern South China Sea (NSCS). It is now accepted that most of these internal tides are generated by tide-topography interaction near Luzon Strait, where tremendous ridges are on the seabed, and propagate westward or northwestward. It was found that the internal tides in the NSCS have largest vertical amplitude up to 100 m [12, 13]. These Internal tides are of interest because of their significant

Received on June 5, 2012

Corresponding author: guopu@scsio.ac.cn

influence on both physical and ecological environments in the ocean. Characteristics and energy fluxes of the internal tides in the NSCS have been investigated with various models [16-18] and in-situ observations [14, 19, 20], especially the western and eastern areas off Dongsha Island. Previous studies suggested that the characteristics of internal tides made changes significantly near Dongsha Island during the shoaling process and, therefore great energy dissipates and contributes to the local mixing, possibly accompanied by the generation of internal solitary waves [21-23].

To understand more comprehensively the internal tides near Dongsha Island, in this paper, we processed 20-day mooring observations for currents and temperatures carried out by South China Sea Monsoon Experiment (SCSMEX) in June 1998. The mooring site was the southern area off Dongsha Island, where the in-situ observations of SCSMEX in May 1998 have been analyzed and reported for studying the internal tides [15]. We now study the internal tides at the same site but another period, to reveal the change and the difference of internal tides in the two periods.

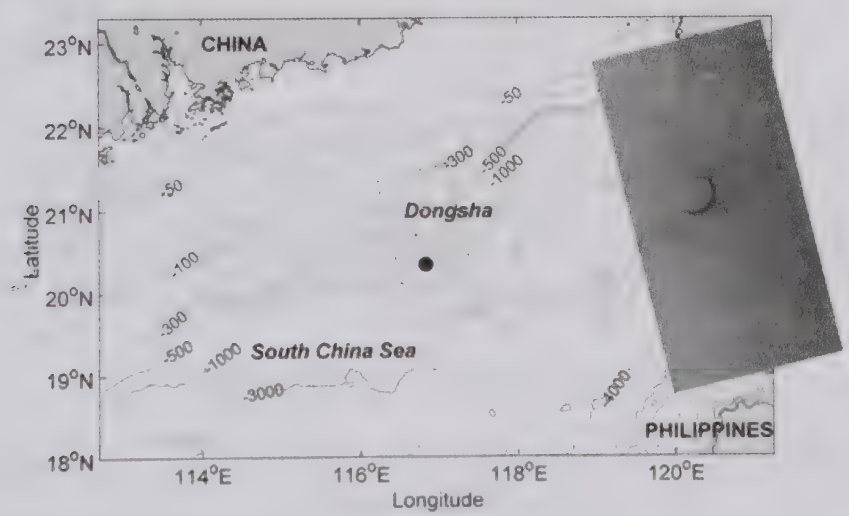

Fig. 1 Map of the northeastern South China Sea (NSCS) with isobaths (units: m) and the SAR image taken on June 23, 1998 (denoted by the dotted rectangle and shown in the right of this figure). The location of ship-anchored by R/V Shiyan 3 (black circle) in June was southwest off Dongsha Island.

2 Data and methods

2.1 Observations

SCSMEX, conducted in 1998, carried out long-time oceanographic observations at a

site (116°50.6′E, 20°21.3′N) southern off Dongsha Island (Fig. 1). The observational period was from 3 June to 23 June, 1998 and R/V Shiyan 3 anchored was the major observational platform at sea. The site is over the continental shelf-break with water depth of about 500 m. Many Satellite synthetic aperture radars (SAR) images around the mooring site show energetic internal waves in this study area. As an example, a SAR image taking during the observational period (on 23 June 1998) is shown in Fig. 1, which indicates the internal waves propagating westward in the study area. Ship-mounted VM-300 kHz ADCP and MKIII CTD were used to record the current and temperature, respectively. The vertical sampling interval for ADCP was set at 3 mins and the measurement covered the depth from 10 m to 134 m with 4 m intervals. The CTD was cast once every 3 hours and the vertical resolution was 1 m.

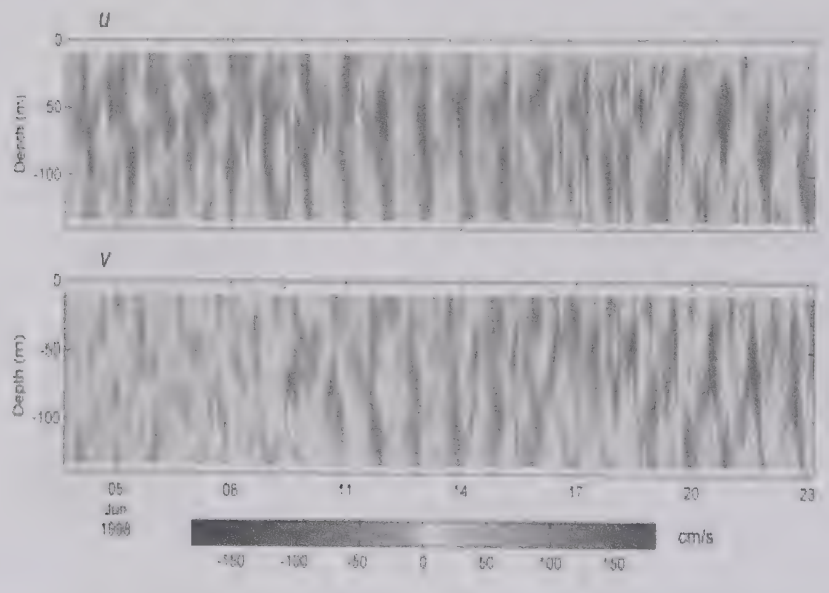

Fig. 2 Eastward u (top) and northward v (bottom) components of raw current during the observational period

The observations have higher quality. A linear interpolation is made to replace some occasional, unrealistic extreme values or missing values in the raw data, using the data at the time nearest to the missing data. Fig. 2 and Fig. 3 show the profiles of observed raw horizontal current and temperature, respectively. There are more than one shear layers of horizontal current in the vertical direction, and the quasi-diurnal variation of the time series of current is also shown in Fig. 2. Significant quasi-diurnal oscillations of isotherm can be seen in Fig. 3, in which the greatest vertical amplitude exceeds 100 m. These oscillations suggest that there are energetic diurnal internal tides in the ocean. To study the characteristics of internal tides, we extract the baroclinic current U_{bc} from the observed

current and subtract the barotropic current U_{bt}, which is defined as the depth-averaged current here. The currents and temperature data are analyzed in the following sections.

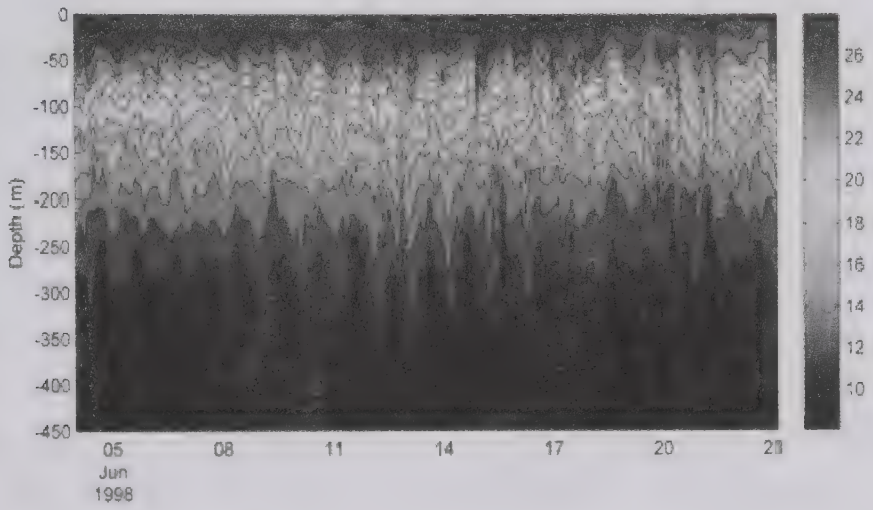

Fig. 3 Time series of isotherm depths from June 5 to 23, 1998

2.2 Methods

We use power spectral analysis and harmonic analysis to identify the primary constituents of internal tides during the observational period. The energetic constituents have the remarkable peaks in the spectral plot [24]. Furthermore, harmonic analysis is used here to isolate the components of the main specific constituents from the baroclinic current. We obtain harmonic constants and baroclinic current at various depths by performing the Matlab program T_Tide [25].

Energy of internal tides denotes the potential effect on the ocean mixing when the internal tides propagate and evolve in the ocean. The kinetic and potential energy of internal tides are calculated respectively to get the total internal tidal energy. The depth-integrated horizontal baroclinic kinetic energy density (KE) is computed by

$$\mathrm{KE} = \frac{1}{2}\overline{\rho}\int_{-H}^{0} U_{bc}^{2}(z)dz\,, \tag{1}$$

with the unit of kJ/m^2, where $\overline{\rho}$ is the vertically averaged water density. The depth-integrated potential energy density (PE) is computed by

$$\mathrm{PE} = \frac{1}{2}\overline{\rho}\int_{-H}^{0} N^{2}(z)\eta^{2}(z)dz\,, \tag{2}$$

with the unit of kJ/m^2, where η is the vertical displacement of internal tides and N is the

buoyancy frequency. Then the total energy density E is calculated by

$$E = KE + PE \tag{3}$$

Because the propagations of internal tides are usually not stable, the components estimated by harmonic analysis are not suitable to calculate the energy at specific frequency band. Therefore, we use the fourth-order Butterworth filter to extract the baroclinic currents at specific frequency band which include the primary constituents of internal tides. Then the total internal tidal energy of primary constituents can be calculated by the formulas given above.

3 Results

3.1 The hydrographic structures

The isotherms in observational period are shown in Fig. 3 on the basis of temperature data series. It can be seen that the isotherm presents significant quasi-diurnal oscillations with most of vertical amplitudes up to 50 m. These isotherm oscillations suggest that seawater is dominated by the diurnal internal tidal waves.

The mean temperature, salinity, density and buoyancy frequency of seawater during the observation period are calculated and shown in Fig. 4 to represent the hydrographic structures. The "double peak" structure near 50 m can be seen from the buoyancy frequency in Fig. 4, suggesting the influence of barrier layer which exists universally in spring, summer and autumn in the NSCS [26-28].

3.2 Primary constituents of Internal Tides

The power spectral densities of ocean temperature at different ocean depths are calculated and Fig. 5 show the spectra plot at 5 layers form ocean surface to bottom. The diurnal and semidiurnal peaks are remarkable in Fig. 5 and diurnal peak value is larger than semidiurnal peak value. So the spectral plot indicates that diurnal and semidiurnal internal tides are dominated in the study area, especially the diurnal constituents.

Harmonic analysis is performed on the baroclinic current then gives the main diurnal (O_1 and K_1) and semidiurnal (M_2 and S_2) constituents. Internal tidal ellipses representing the variation of internal tidal currents are shown in Fig. 6. It can be seen in this figure that the diurnal internal tides (O_1 and K_1) are stronger than the semidiurnal (M_2 and S_2) internal tides. K_1 constituent is the strongest during the observational period with the maximum current larger than 14 cm/s, and S_2 constituent is the weakest with the maximum current less than 4 cm/s.

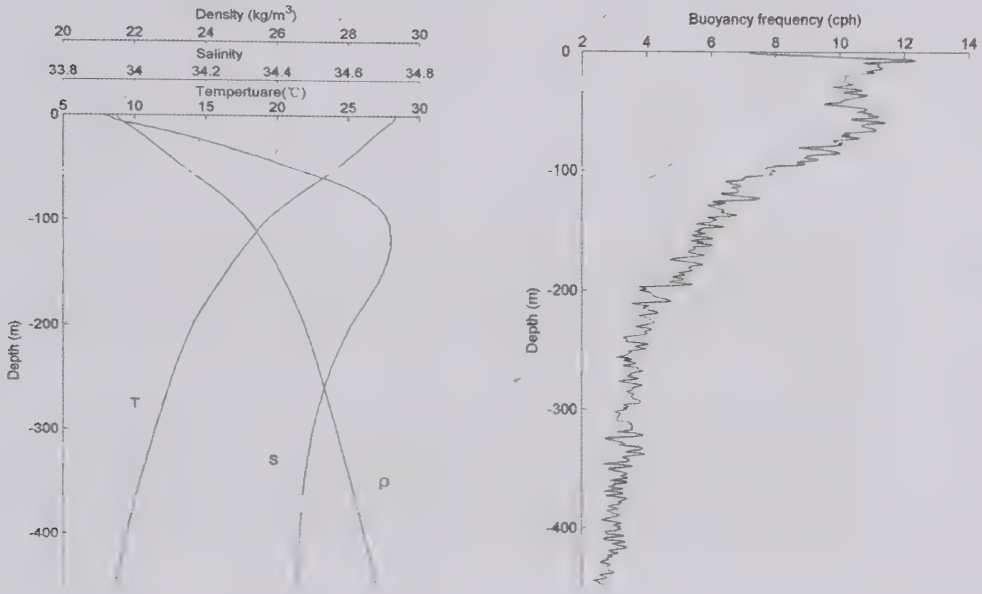

Fig. 4 Mean temperature T, salinity S and density ρ at the mooring site in the observational period (left); buoyancy frequency (right)

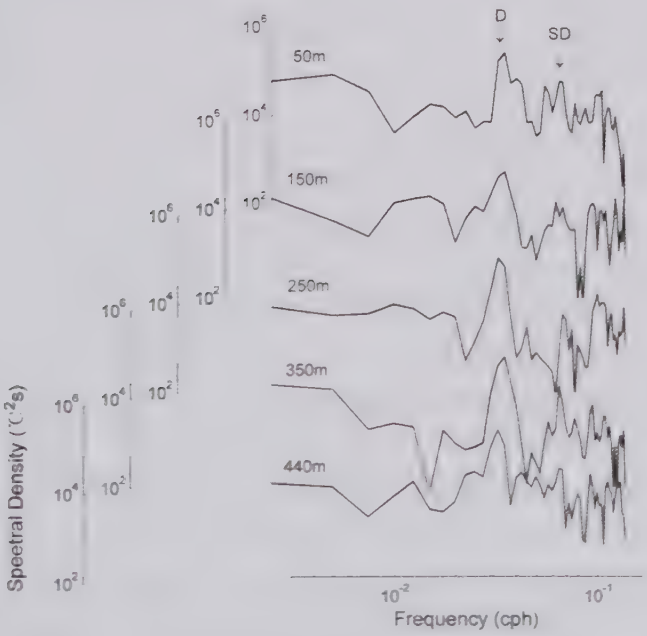

Fig. 5 The power spectra density of temperature at 50 m, 150 m, 250 m, 350 m, 440 m depths. Signs D and SD denote the diurnal and semidiurnal frequency, respectively.

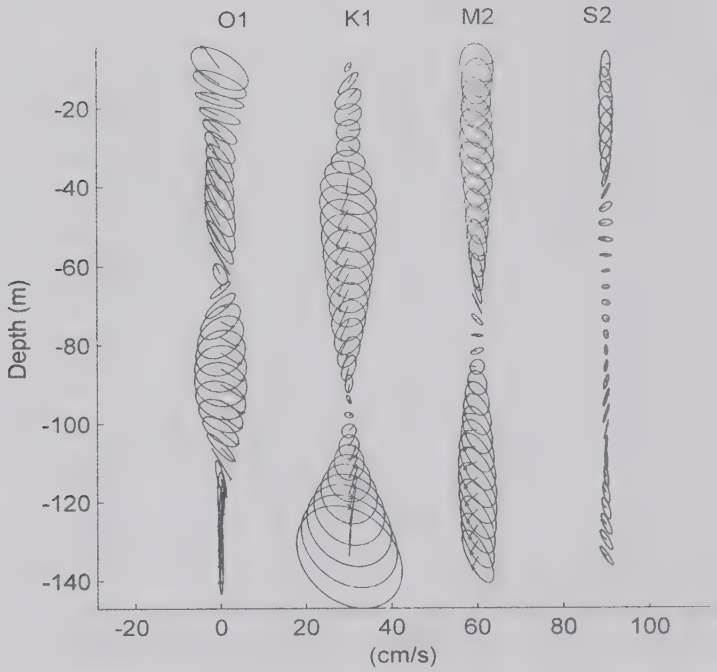

Fig. 6 Vertical structure of the baroclinic tidal ellipses of for primary constitutes (O_1, K_1, M_2 and S_2). The lines from ellipses' centers show the phases and the arrows show the rotating directions of currents vectors.

3.3 Internal tidal energy

Fig. 5 shows that the diurnal and semidiurnal internal tides are more energetic than components at other frequency bands. So the internal tidal energy affecting the ocean environment mainly concentrates in the diurnal and semidiurnal band. To estimate the energy in the two bands, we isolate the diurnal and semidiurnal internal tidal currents by performing the fourth-order Butterworth filter on the baroclinic current. Cutoff frequencies of the filter are set as 0.8 and 1.2 cpd to include diurnal (O_1 and K_1) components and 1.6 and 2.4 cpd to include semidiurnal components, respectively. Fig. 7 show the band-passed baroclinic diurnal and semidiurnal currents. The diurnal and semidiurnal internal tides seem to be stronger near 21 June. The vertical shear layers of current are clear in Fig. 7 and it can be seen that the depth of shear layer changes with time.

Given the band-passed currents, KE above 134 m depth and PE for the whole water column of diurnal (semidiurnal) are calculated using formula (1) and (2), respectively. The results are shown in Fig. 8. It can be seen that the diurnal internal tides, in general, are more energetic than semidiurnal internal tides. The KE of diurnal (semidiurnal) internal

tides reaches the maximum value -2 kJ/m^2 (-1 kJ/m2) in on 21 June. The temporal distributions of diurnal and semidiurnal KE are similar, with two distinct extreme values on 6 June and 21 June. But the temporal distributions of diurnal and semidiurnal PE are different. The maximum PE values of diurnal and semidiurnal are -3.5 and -1.5 kJ/m^2 during the observational period, respectively.

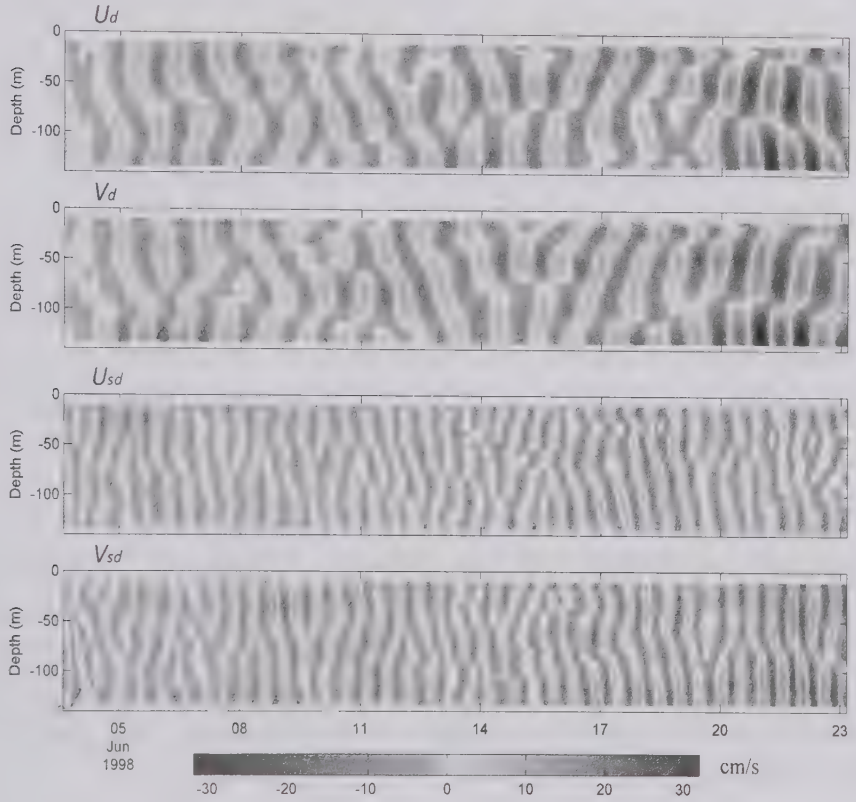

Fig. 7 Band-passed baroclinic diurnal current and semidiurnal current. ud (usd) and vd (vsd) are the along-shelf and cross-shelf components of diurnal (semidiurnal) currents, respectively.

4 Discussion and summary

We analyzed the internal tides in the southern area off Dongsha Island using in-situ ocean current data and CTD data. These results can be compared with the observation at the same site get by SCSMEX in May [15]. Based on the in-situ data in June, Baroclinic current ellipses were calculated to study the characteristics of primary constituents of internal tides which are the same with that in May, i.e., the diurnal constituents (O_1 and K_1) and semidiurnal constituents (M_2 and S_2). The internal tidal currents in the study area are dominated by diurnals in May and June, but the maximum semi-major axe in June (K_1, more than 14 cm/s) is greater than that in May (K_1, less than 11 cm/s).

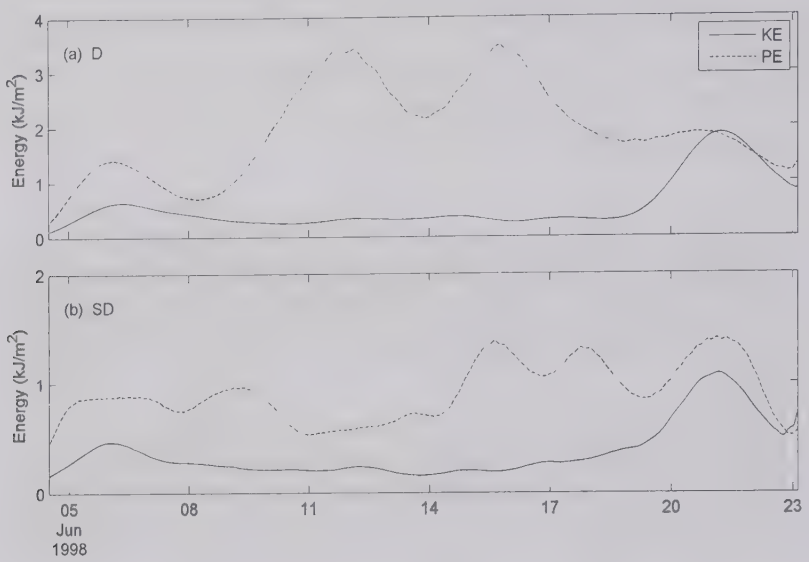

Fig. 8 KE and PE of (a) diurnal internal tides and (b) semidiurnal internal tides during the observational period.

The variation of ocean temperature field with time is much visualized phenomena indicating the existence of internal tides. Virtually, it is the potential energy of internal tides that impacts the ocean temperature field greatly. So power spectra of variation of ocean temperature were calculated to show the potential energy distribution with frequency. Consistently with the result of harmonic analysis, spectra plot shows the highest potential energy in the diurnal band, which is like the conditions in May.

Finally, the kinetic energy density above the depth of 134 m was calculated using the band-passed currents and the potential energy density for the whole water column was calculated using the vertical displacement of internal tides, respectively. The maximum values of KE (PE) are up to 2 (3.5) kJ/m^2 for diurnal internal tides, and up to 1 (1.5) kJ/m^2 for semidiurnal internal tides. Just like in May, variation of energy with time shows that the internal tides appear to be intermittent, suggesting the complicacy of the generation or the propagation of internal tides in the NSCS.

Acknowledgement

The authors thank the scientists and crew aboard R/V Shiyan No.3 for SCSMEX cruises. This work is supported by the National Natural Science Foundation of China (No. 41176025, 40876008) and the SCSMEX project.

References

[1] Holloway P E, Chatwin, Craig P. Internal tide observations from the Australian North West Shelf in summer 1995 [J]. Phys. Oceanogr., 2001, 31(5): 1 182 - 1 199.

[2] Lerczak J A, Winant C D, Hendershott M C. Observations of the semidiurnal internal tide on the southern California slope and shelf [J]. Geophys. Res., 2003, 108(C3): 3 068 - 3 068, doi: 10.1029/2001JC001128.

[3] Nash J D, Alford M H, Kunze E. Estimating internal wave energy fluxes in the ocean [J]. Atmos. Oceanic Technol., 2005, 22: 1 551 - 1 570.

[4] Nash J D, Kunze E, Lee C M, et al. Structure of the baroclinic tide generated at Kaena Ridge, Hawaii [J]. Phys. Oceanogr., 2006, 36: 1 123 - 1 135.

[5] Alford M H, Zhan Z. Global patterns of low-mode internal wave propagation. Part I: Energy and energy flux [J]. Phys. Oceanogr., 2007, 37, 1 829 - 1 848, doi: 10.1175/JPO3085.1.

[6] Wunsch C. Internal tides in the ocean [J]. Rev. Geophys. Space Phys., 1975, 13(1): 167 - 182.

[7] St. Laurent L, Garrett C. The role of internal tides in mixing the deep ocean [J]. J. Phys. Oceanogr., 2002, 32(10): 2 882 - 2 899.

[8] Jan S, Chen C A. Potential biogeochemical effects from vigorous internal tides generated in Luzon Strait: A case study at the southernmost coast of Taiwan [J]. J. Geophys. Res., 2009, 114: C04021, doi: 10.1029/2008JC004887.

[9] Liu A K, Chang Y S, Hsu M K, et al. Evolution of nonlinear internal waves in the East and South China Seas [J]. J. Geophys. Res., 1998, 103: 7 995 - 8 008.

[10] Hsu M K, Liu A K. Nonlinear internal waves in the South China Sea [J]. Can. J. Remote Sens., 2000, 26: 72 - 81.

[11] Zhao Z, Klemas V, Zheng Q, et al. Remote sensing evidence for baroclinic tide origin of internal solitary waves in the northeastern South China Sea [J]. Geophys. Res. Lett., 2004, 31: L06302, doi: 10.1029/2003GL019077.

[12] Duda T F, Lynch J F, Irish J D, et al. Internal tide and nonlinear internal wave behavior at the continental slope in the northern South China Sea, IEEE J. Oceanic Eng., 2004, 29: 1 105 - 1 130.

[13] Fang, W. D., P. Shi, X. M. Long, and Q. W. Mao (2005), Internal solitons in the northern South China Sea from insitu observations, Chinese Science Bulletin, 50: 1 627 - 1 631.

[14] Liang X F, Zhang X Q, Tian J W. Observation of internal tides and near-inertial motions in the upper 450 m layer of the northern South China Sea [J]. Chinese Science Bulletin, 2005, 50: 2 890 - 2 895.

[15] Guo P, Fang W D, Gan Z J, et al. Internal tide characteristics over northern South China Sea continental slope [J]. Chinese Science Bulletin, 2006, 51(S3): 15 - 22.

[16] Jan S, Chern C S, Wang J, et al. Generation of diurnal K1 internal tide in the Luzon Strait and its influence on surface tide in the South China Sea [J]. J. Geophys. Res., 2007, 112: C06019, doi:

10.1029/2006JC004003.

[17] Jan S, Lien R C, and Ting C H. Numerical Study of Baroclinic Tides in Luzon Strait [J]. J. Oceanogr., 2008, 64(5): 789 - 802.

[18] Shaw P T, Ko D S, Chao S Y. Internal solitary waves induced by flow over a ridge: With applications to the northern South China Sea [J]. J. Geophys. Res., 2009, 114: C02019, doi: 10.1029/2008JC005007.

[19] Duda T F, Rainville L. Diurnal and semidiurnal internal tide energy flux at a continental slope in the South China Sea [J]. J. Geophys. Res.,2008, 113: C03025, doi: 10.1029/2007JC004418.

[20] Guo P, Fang W, Liu C, et al. Seasonal characteristics of internal tides on the continental shelf in the northern South China Sea [J]. J. Geophys. Res., 2012, 117: C04023, doi:10.1029/2011JC007215.

[21] Zhao Z, Alford M H. Source and propagation of internal solitary waves in the northeastern South China Sea [J]. J. Geophys. Res., 2006, 111:C11012, doi: 10.1029/2006JC003644.

[22] Helfrich K R, Grimshaw R H J. Nonlinear disintegration of the internal tide [J]. J. Phys. Oceanogr., 2008, 38: 686-701, doi: 10.1175/2007JPO3826.1.

[23] Alford M H, Lien R C, Simmons H, et al. Speed and evolution of nonlinear internal waves transiting the South China Sea [J]. J. Phys. Oceanogr., 2010, 40:1 338 - 1 355, doi: 10.1175/2010JPO4388.1.

[24] Emery W J, Thomson R E. Data Analysis Methods in Physical Oceanography [M] (second and revised edition). Amsterdam: Elsevier, 2001.

[25] Pawlowicz R, Beardsley R, Lentz S. Classical tidal harmonic analysis including error estimates in MATLAB using T_TIDE [J]. Computers Geosci, 2002, 28: 929 - 937.

[26] Fang W D, Shi P, Mao Q W, et al. Variation of upper ocean in the northern South China Sea from mooring station observations [J]. Acta Oceanol. Sin., 2000, 22(5): 23 - 30.

[27] Du Y, Wang D X, Shi P, et al. Seasonal variation of the barrier layer in the South China Sea and its relationship to the sea surface flux [J]. Chinese J. Atmos. Sci., 2004, 28(1): 101 - 111.

[28] Pan A J, Wang X F, Xu J D, et al. Barrier layer in the northeastern South China Sea and its formation mechanism [J]. Chinese Sci. Bull., 2006, 51(4): , 472 - 479.

1998 年南海北部 20 天定点连续观测的内潮分析

蔡 扬[1]，郭 朴[2]，方文东[2]

（1. 国家海洋局 南海预报中心，广州 510300；

2. 中国科学院南海海洋研究所 热带海洋环境国家重点实验室，广州 510301）

摘 要：对1998年6月南海北部20天的海流和温度定点连续观测资料进行分析，得到该海域内潮的特征及其能量分布。分析结果显示内潮的主要成分为O_1，K_1，M_2与S_2分量，其中全日内潮（O_1与K_1）的能量占主要部分。在观测期间，此四个分量的海流失量均为顺时针旋转，其潮流椭圆半长轴的最大值超过14 cm/s。海水温度的变化显示出内潮存在准日周期振动，平均垂向振幅达到50 m。观测到的内潮携带高能量且其活动存在不连续性，在观测范围内，全日内潮的动能及势能密度的最大值分别达到2 kJ/m^{2}及3.5 kJ/m^2，半日内潮的动能及势能密度的最大值分别达到1 kJ/m^{2}及1.5 kJ/m^2。

关键词：内潮；定点观测；南海北部；能量

Comparison of spectral partitioning techniques for wind wave and swell

LI Shui-qing, ZHAO Dong-liang

Physical Oceanography Laboratory, Ocean University of China, Qingdao 266100, *Shandong province, China*

Abstract: The ocean waves are generally mixed with wind wave and swell. In order to separate these two kinds of ocean waves, many wave spectral partitioning techniques have been proposed. In this study, a two-dimensional(2D) and three one-dimensional (1D) wave spectral partitioning techniques (denoted as PM, WH, and JP) are examined based on the model simulations and in-situ observations. It is shown that the 2D technique could provide the most reliable results as a whole. Compared with 2D technique, PM and JP techniques obviously overestimate the wind-wave components, and the same situation happens for WH technique at low wind speed. With the adjustment of the partitioning frequency ratio, the 1D PM technique is modified, in which the result agree well with that of the 2D scheme.

Keywords: wind wave; swell; partition; wave spectrum

1 Introduction

It is well known that the waves in the ocean are commonly mixed with swell and wind wave. The former refers to waves that are generated elsewhere and propagating over long distances, or the local winds slow down or change direction, while the latter is defined as waves in equilibrium with local wind. Because of the different dynamics involved and quite distinct feathers between them, it is necessary to separate them in the real application. Accurate separation of wind wave and swell is central to a variety of activities, such as air-sea interaction, ocean wave modeling, and coastal engineering.

Many efforts have been devoted to distinguishing between wind wave and swell. Wang(1990)[1] discussed the criterion for swell, and Guo et al. (1997)[2] proposed the mixed wave energy composition factor to separate swell from wind wave. These studies mainly focus on determining what kind of ocean waves by using of a criterion, and they did not provide the concrete procedure for the separation of wind wave and swell from the highly mixed sea.

Received on July 10, 2012

Corresponding author: lshq160@gmail.com

The wave spectrum reflects the inner structure of ocean wave in frequency domain, and spectral partition is suggested to be the best way to isolate wind wave and swell [3,4]. These methods can be typically categorized into 1D and 2D techniques, which are based on one and two dimensional wave spectrum, respectively. The 2D technique was first proposed by Gerling (1992)[5]. According to the properties of wind input into ocean waves, the information of wind vector and wave directional spectrum is used to separate wind wave and swell. It is regarded that 2D technique gives more reliable results than that of 1D technique [6, 7]. However, the 2D technique is very limited in practical application due to the lack of coincident measurement of wind vector and wave directional spectrum. Compared with 2D technique, 1D technique is more convenient to separate wind wave and swell. The basic idea of 1D technique is to set a partition frequency for the wave spectrum, in which the lower frequency and higher frequency part correspond to the swell and wind wave, respectively. Many methods of this kind have been proposed, which is based on the wave frequency spectrum only, or wind speed at the same time. Their reliability can be evaluated by the comparison with 2D technique in the case of natural sea state.

Earle [8] proposed an 1D technique that simultaneously depends on wave frequency spectrum and wind speed, in which the partition frequency is a function of wind speed (hereinafter referred as PM technique). Some of the 1D techniques separate wind wave and swell based on wave frequency spectrum only. For example, Wang and Hwang(2001)[9] suggested that the difference of the wave steepness could be used to distinguish wind wave and swell (hereinafter referred as WH technique). According to the overshot characteristics of wind wave, Portilla et al.[7] also gave a scheme based on the wave frequency spectrum (hereafter referred as JP technique).

In this study, the 2D technique and three 1D techniques mentioned above were tested through model simulations and in-situ observational data. With the adjustment of ratio coefficient of partition frequency, the PM technique is modified that is more consistent with the results of the 2D technique.

2 Brief description of the partition techniques

2.1 2D partition technique

The 2D partition technique is based on not only the wave directional spectrum, which fully represented the inner structure of ocean wave in frequency and direction domain, but also the wind vector. According to Komen et al. (1984)[10], the wave component is regarded as pure wind wave when the following relationship is satisfied:

$$\eta \frac{U_{10}}{c} \cos(\theta - \psi) > 1 \qquad |\theta - \psi| < \frac{\pi}{2} \tag{1}$$

where U_{10} is the wind speed at 10 m height above the sea surface, c the phase speed, θ the corresponding wave direction, ψ the wind direction, and η is a constant, which is usually chosen as 1.3 [11,12].

2.2 1D partition technique

2.2.1 PM partition technique

Based on the idea that the wind wave and swell correspond to higher frequency and lower frequency part of the wave frequency spectrum, Earle (1984)[8] suggested that it could be divided by the partition frequency f_s as follows

$$f_s = 0.8 f_{PM} \tag{2}$$

where f_{PM} is the peak frequency of PM wind wave spectrum that corresponds to the fully developed wind wave[13]. It is only related to wind speed, and can be written as $f_{PM} = 0.13g / U_{10}$, where g = 9.8 m/s^2 is the gravitational acceleration.

2.2.2 WH partition technique

Based on the wave frequency spectrum observed by buoy, Wang and Hwang (2001)[9] defined a function of mean wave steepness that can be written as

$$A(f_*) = \frac{8\pi \left[\int_{f_*}^{f_d} f^2 S(f) df \right]}{g \left[\int_{f_*}^{f_d} S(f) df \right]^{1/2}} \tag{3}$$

where $S(f)$ is the wave frequency spectrum, f_d is the upper limit of frequency measured by buoys. They further derived an empirical relationship between f_s and the peak frequency f_m of wave steepness function based on the PM wind wave spectra[13], which can be expressed as:

$$f_s = A(f_m)^B \tag{4}$$

where A = 4.112, B = 1.746. Therefore, the WH technique only depends on wave frequency spectrum to calculate the wave steepness function, and the partition frequency can be determined by Eq. (4).

2.2.3 JP partition technique

In the mixed ocean waves, the wave frequency spectrum usually has multi-peaks. The various spectral peaks represent different wave systems. The trough between the two adjacent peaks is regarded as the borderline of wave systems. In this way, the wind wave and swell can be separated from the ocean waves. Portilla et al. [7] defined a coefficient as the ratio λ of measured wave spectrum $S(f_p)$ and PM wave spectrum $S_{PM}(f_p)$ at the spectral peak. It can be written as:

$$\lambda = \frac{S(f_P)}{S_{PM}(f_p)} \tag{5}$$

The wind wave spectrum will exceed the corresponding PM spectrum before it reaches to the fully developed state. This is the so called overshot phenomenon. The JP partition technique suggested that the wave system was wind wave when $\lambda > 1.0$, otherwise, the wave system was swell. As the WH technique, the JP technique is only related to the wave frequency spectrum, and independent of wind speed.

3 Results and discussion

3.1 Model simulation

One way to test the ability of partition technique is to detect the wind wave and swell from the constructed mixed ocean waves with the specified wave spectra. A Gaussian type swell spectral model [14] and the JONSWAP wind wave spectral model [15] are used to construct the wave spectrum in this study. The JONSWAP frequency spectrum is

$$S_w(f) = \alpha \frac{g^2}{(2\pi)^{-4}} f^{-5} \exp\left\{-1.25\left(\frac{f_0}{f}\right)^4\right\} \gamma^{\exp\left\{\frac{(f-f_0)}{2\sigma^2 f_0^2}\right\}} \tag{6}$$

where σ is given as:

$$\sigma = \begin{cases} 0.07 & f \le f_0 \\ 0.09 & f > f_0 \end{cases} \tag{7}$$

and α, f_0, γ are related to wave age β [16,17].

$$\alpha = 0.0817(7\pi\beta)^{-6/7}$$
$$f_0 = 1.31g/(\pi^2\beta U_{10}) \quad (8)$$
$$\gamma = 7.0(7\pi\beta)^{-3/7}$$

The 2D wind wave directional spectrum is obtained as the product of wave frequency spectrum and directional spreading function. The directional spreading function G (θ) is taken as $G(\theta)=16/5\pi\cos\theta$. The 2D swell spectrum is given as:

$$S_{sw}(f,\theta)=\frac{\langle h^2\rangle}{2\pi\sigma_f\sigma_\theta}\exp\left\{-0.5\left[\left(\frac{f-f_p}{\sigma_f}\right)^2+\left(\frac{\theta-\theta_p}{\sigma_\theta}\right)^2\right]\right\} \quad (9)$$

Where $\langle h^2\rangle$ is the variance of the heights, σ_f and σ_θ are the standard deviations of frequency and wave angle, respectively, f_p is the peak frequency and θ_p is the wave direction corresponding to the spectral peak.

Tab. 1 Relative errors of the spectral technique based on model simulations

Wave state	Parameter	2D	PM	WH	JP
Swell (H_s, T_P, σ_f)	(1m,8s,0.005)	0	0	-1	0
	(1m,8s,0.03)	0	0	-0.83	0
	(4m,12s,0.005)	0	0	-1	0
	(4m,12s,0.03)	0	0	-0.72	0
Wind wave (U_{10}, β)	(5m/s,0.5)	0	0	-1	0
	(5m/s,0.9)	-0.06	0	-0.42	0
	(10m/s,0.5)	0	0	-0.34	0
	(10m/s,0.9)	-0.05	0	-0.18	0
	(15m/s,0.5)	0	0	-0.11	0
	(15m/s,0.9)	-0.05	0	-0.36	0
Mixed sea (U_{10}, θ, β) ($H_s, T_P, \theta_m, \sigma_f, \sigma_\theta$)	Figure 1a (10,0,0.5) (2.5,14,45,0.005,5)	0	0	-0.34	0
	Fig. 1b (10,0,0.9) (2.5,14,45,0.005,5)	-0.05	0	-0.18	0
	Figure 2a (6,0,0.9) (1.2,9,0,0.008,5)	-0.06	0	-0.35	0
	Figure 2b (9,90,0.8) (0.85,7, 0,0.008,5)	-0.03	0.20	-0.19	0.20

In this study, three wave systems, pure wind wave, swell, and mixed wind wave and

swell, are deployed in the numerical simulation. The key parameters and simulation results are listed in Tab. 1. The ability of detecting wave system for the spectral partition techniques is evaluated in terms of the relative error.

The relative errors at various cases for each spectral technique are shown in Tab. 1. In the case of swell, all partition techniques except for WH can detect the swell. The reason for the invalidation of WH technique is the assumption that the wind waves contribute mostly to the total wave steepness. It is obviously not applied in the case of swell. For pure wind wave, both PM and JP techniques perform well, and the 2D technique also detects the wind waves. However, the WH technique can not well distinguish the wind wave when it approaches to the fully developed state ($\beta = 0.9$).

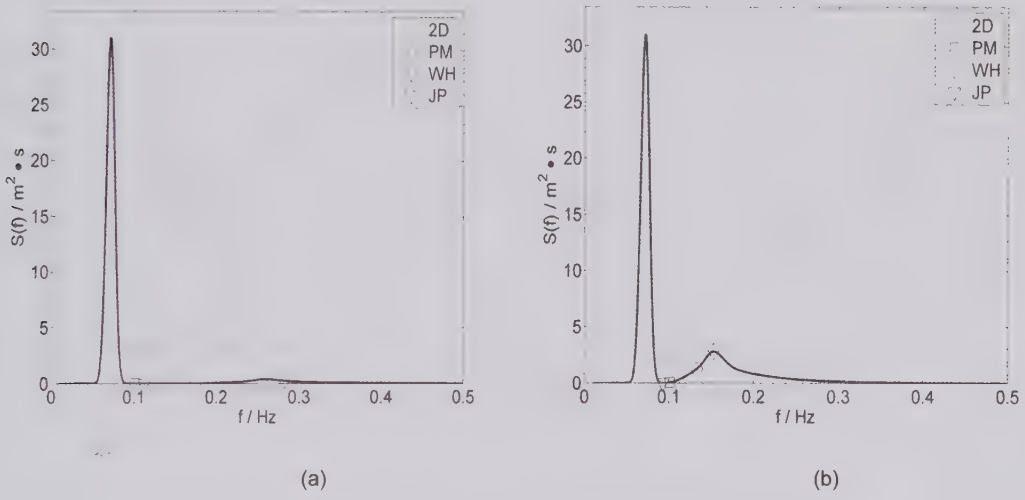

Fig. 1 Coexistence of wind wave and swell radiated from distant storm (a) $\beta = 0.5$ **(b)** $\beta = 0.9$

In the case of mixed sea, two kind of swell are considered. The first is that the swell propagates from distant storms, in which the corresponding frequency band is narrow. As shown in Fig. 1, all the partition techniques can separate the wind wave and swell, except for the underestimation of wind waves by WH. The second is that the swell is transformed from the wind wave due to the decrease of wind speed or changing of wind direction. Fig. 2a and 2b show the cases of wind speed decreased from 10 m/s to 6 m/s and wind direction changed from 0° to 90°, respectively. It can be seen that the 2D partition technique can well separate the wind wave and swell in each case, while the WH partition technique has great relative errors. Both PM and JP techniques perform quite well in the former case, and relatively greater errors occur in the latter case. The failure of PM can be ascribed to the neglect of wind direction. The overlap of wind wave and swell can enhance the swell spectrum that leads to the fake overshot, which will be wrongly detected by the JP

partition technique.

From the above analysis, the 2D partition technique can perform well in each case, and the relative errors are less than 10% in all cases. Compared to the WH partition technique, the PM and JP partition techniques generally give more reliable results. Therefore, the 2D method will be used to validate the three 1D partition techniques with the observational data from buoys.

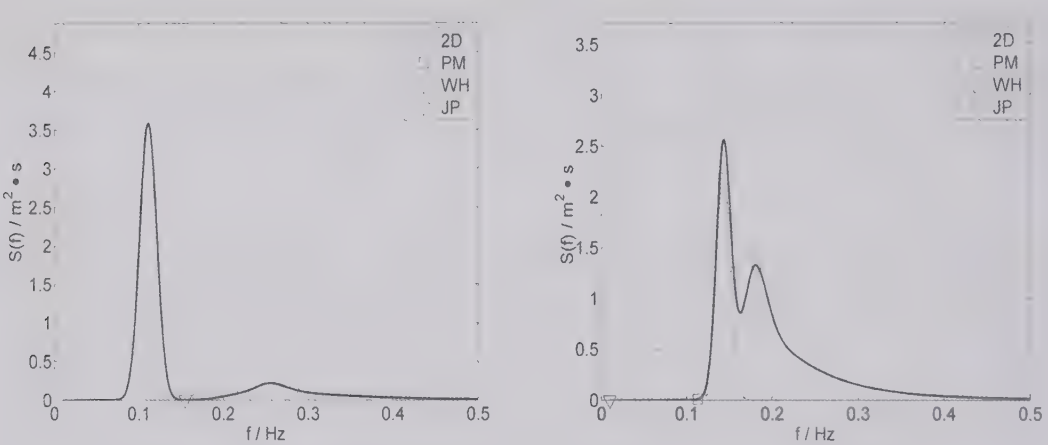

Fig. 2 Coexistence of wind wave and swell generated from wind variation
(a) wind speed decreasing; (b) wind directionchanging

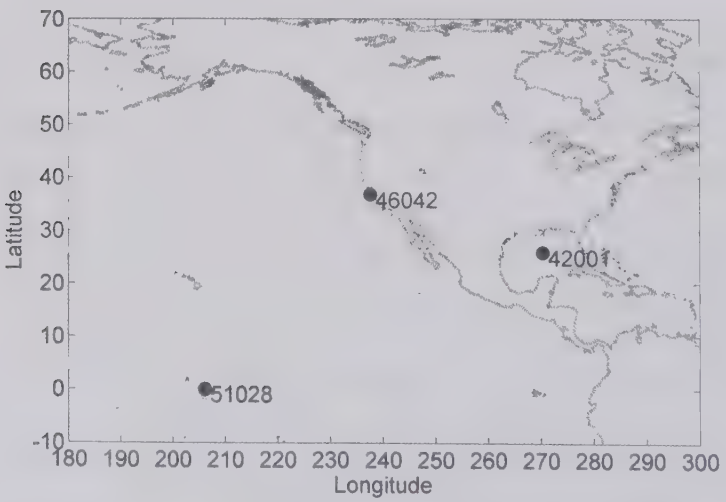

Fig. 3 Locations of NDBC buoys

3.2 Validation with buoy data

The dataset consists of measurements from three buoys operated by the National Data Buoy Center (NDBC) as shown in Fig. 3. One of the buoys 42001 is located in the gulf of Mexico, where Hwang et al. (1998)[18] suggested that wave energy of swell rarely exceeded 15% of the total spectral energy. The buoy 51028 is in the site of "swell pool" suggested by Chen et al. (2002)[19], which is dominated by the swell. The observational data from buoy 46042 represent the mixed sea in the natural condition. The observational data measured by the three buoys in the period of 2005 are applied in the following discussion.

Fig. 4 shows the variations of bin-averaged significant wave height (SWH) of wind wave with wind speed with various partition techniques. The fully developed relationship between SWH and wind speed [20] is also plotted for reference in Fig. 4. It can be seen that PM technique systematically overestimates the SWH compared with the fully developed relationship in the wind speed range of 5 m/s - 10 m/s. The results of WH technique also significantly overestimate the SWH when the wind speed is less than 6m/s, and are consistent with those of the 2D technique at higher wind speed. The results of JP technique are generally consistent with those of the 2D technique, although they slightly exceed the fully developed relationship at the low wind speeds.

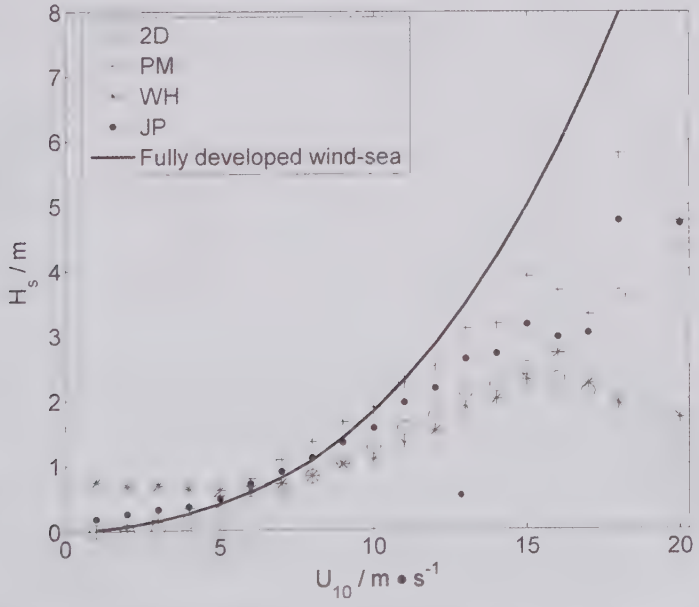

Fig. 4 Variations of the SWH of wind wave derived from different spectral techniques with wind speed

Direct comparison between the 1D techniques and 2D technique is shown in Fig. 5. The systematic overestimation of PM technique is quite obvious as shown in Fig. 5a, which has been previously suggested by Portilla et al.(2009)[7]. WH technique significantly overestimates the wind wave at the wind speed of 0 m/s - 6 m/s (Fig. 5b), this is because the sea is frequently dominated by swell at low wind speeds [19]. Gilhousen and Hervey(2001)[21] also pointed out the same problem, and they suggested that additional wind information should be used to improve the performance. The results given by WH technique at higher wind speeds are generally consistent with those of 2D technique (Fig. 5c), although the large scatter is observed. In general, the results of JP technique are greater than those of 2D technique, especially at high wind speeds. Quantitative comparisons of 1D techniques with 2D technique are given in Tab. 2 in terms of bias and root mean square error (RMSE). It can be seen that WH technique has the lowest bias, while its RMSE is the largest. On the contrary, the PM technique has the largest bias, and its RMSE is the lowest.

Tab. 2 Errors of each 1D spectral technique from field tests

	42001		46042		51028		Total	
	Bias	RMSE	Bias	RMSE	Bias	RMSE	Bias	RMSE
PM	0.35	0.53	0.35	0.46	0.37	0.41	0.37	0.50
WH	0.29	0.61	0.23	0.68	0.07	0.49	0.22	0.60
JP	0.31	0.59	0.28	0.54	0.16	0.30	0.28	0.52
Improved PM	0.05	0.22	-0.01	0.11	-0.03	0.06	0.05	0.18

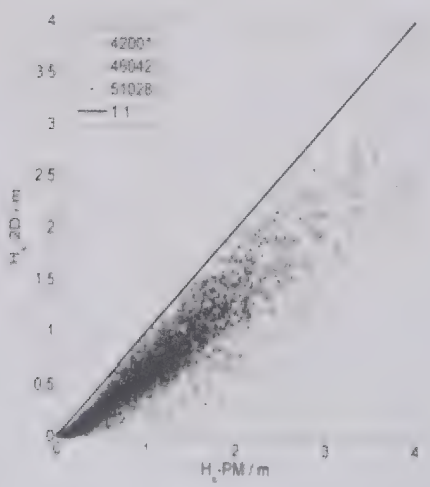

(a)

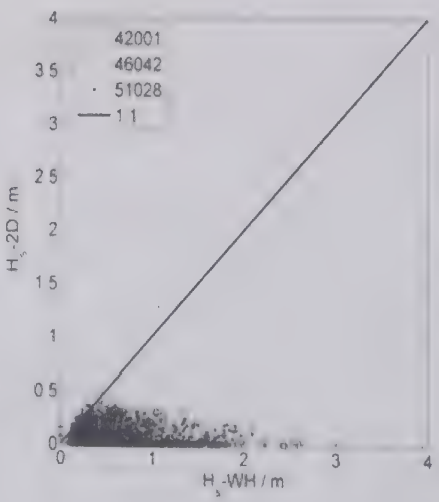

(b)

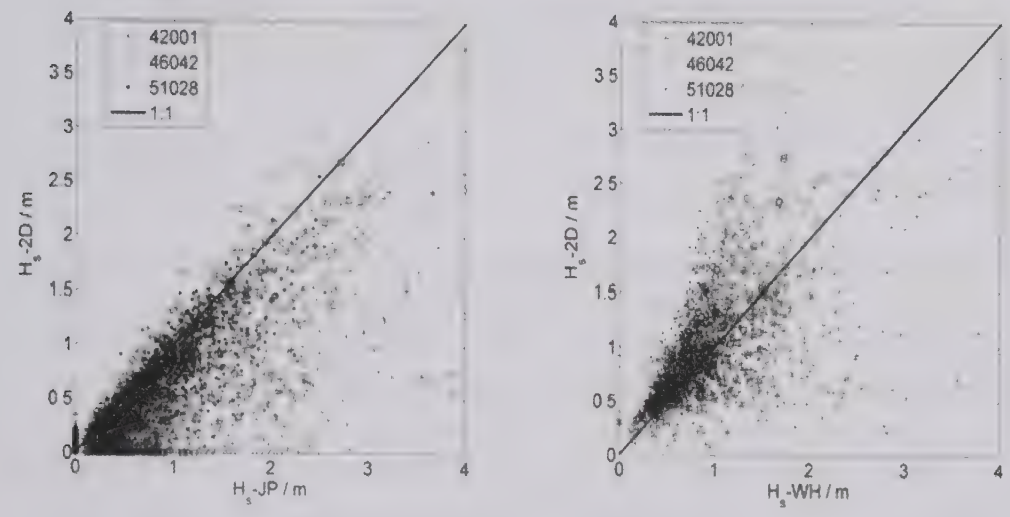

Fig. 5 Comparison of the SWH of wind wave from 2D technique with that given by (a) PM, (b) WH at wind speed up to 6 m/s, (c) WH at wind speed higher than 6 m/s, (d) JP

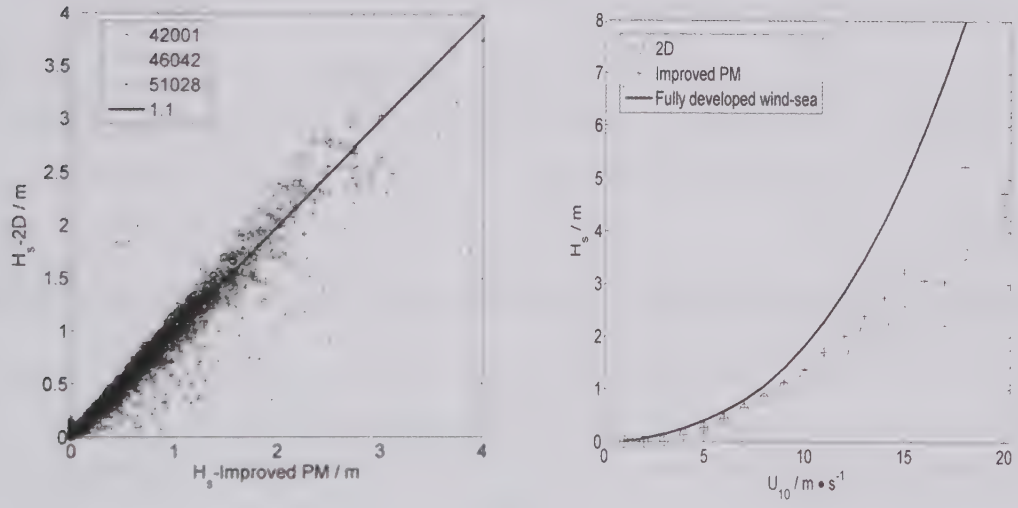

Fig. 6 Comparison of the 2D technique with the improved PM technique in terms of the SWH of wind wave (a) 1:1 comparison (b) in terms of variation with wind speed

The overestimation of wind wave by PM technique can be easily improved by the adjustment of the partition frequency f_s. It is found that the PM technique gives the best agreements with 2D technique when $f_s = 1.2 f_{PM}$ replaces the Eq. (2) (Figure 6 and Table 2). On the other hand, almost the same relationship ($f_s = 1.22 f_{PM}$) can be derived by assuming that the corresponding phase velocity of f_s equals U_{10}, i.e. $g / 2\pi f_s = U_{10}$). In

addition, it is shown by the numerical model that waves for $f > 1.25 f_{PM}$ decay quickly[22], which indicates that it is physically reasonable by using $f_s = 1.2 f_{PM}$ to separate the wind wave and swell.

4 Summary

In this study, the performance of the 2D wave spectral partitioning technique and three 1D wave spectral partitioning techniques are examined through the model simulations and the in-situ observations. In general, the 2D technique can provide the most reliable results, and it is used as a reference to examine the 1D techniques. It is found that PM technique obviously overestimates the wind wave components, and the same situation happens to WH technique at lower wind speeds, while it is consistent with 2D technique at higher wind speed. The results of JP technique are generally greater than those of 2D technique. With the adjustment of partition frequency, the PM technique is improved, in which, it performs best in terms of bias and RMSE.

Acknowledgements

This study is supported by the National Natural Science Foundation of China (No. 41076007) and the National Basic Research Program of China (No. 2009CB421200).

Reference

[1] Wang B Y. Criteria of differentiating swell from wind waves [J]. J. Oceanogr. Huanghai & Bohai Sea, 1990, 8(1): 16 - 24.

[2] Guo P F, Shi P, Wang H, et al. A new criterion between wind wave and swell wave [J]. Journal of Ocean University of Qingdao, 1997, 27(2): 131 - 136.

[3] Semedo A. A Global View on the Wind Sea and Swell Climate and Variability from ERA-40 [J]. Journal of Climate, 2010, 24(5): 1 461 - 1 479.

[4] Hanson J L, Phillips O M. Automated Analysis of Ocean Surface Directional Wave Spectra [J]. J. Atmos. Oceanic. Technol., 2001, 18(2): 277 - 293.

[5] Gerling T W. Partitioning Sequences and Arrays of Directional Ocean Wave Spectra into Component Wave Systems [J]. J. Atmos. Oceanic Technol., 1992, 9(4): 444 - 458.

[6] Drennan W M, Graber H C, Hauser D, et al. On the wave age dependence of wind stress over pure wind seas [J]. J. Geophys. Res., 2003, 108(C3), 8062, doi:10.1029/2000JC000715.

[7] Portilla J, Ocampo-Torres F J, Monbaliu J. Spectral Partitioning and Identification of Wind Sea and Swell [J]. J. Atmos. Oceanic Technol., 2009, 26(1): 107 - 122.

[8] Earle M D. Development of algorithms for separation of sea and swell [R]. National Data Buoy Center Tech. Rep. MEC-87-1, NDBC. 1984, 53pp.

[9] Wang D W, Hwang P A. An Operational Method for Separating Wind Sea and Swell from Ocean Wave Spectra [J]. J. Atmos. Oceanic Technol., 2001, 18(12): 2 052 - 2 062.

[10] Komen G J, Hasselmann S, Hasselmann K. On the Existence of a Fully Developed Wind-sea Spectrum [J]. J. Phys. Oceanogr., 1984, 14(8): 1 271 - 1 285.

[11] Hasselmann S, Brüning C, Hasselmann K, et al. An improved algorithm for the retrieval of ocean wave spectra from synthetic aperture radar image spectra [J]. J. Geophys. Res., 1996, 101(C7): 16 615 - 16 629.

[12] Voorrips A C, Makin V K, Hasselmann S. Assimilation of wave spectra from pitch-and-roll buoys in a North Sea wave model [J]. J. Geophys. Res., 1997, 102(C3): 5 829 - 5 849.

[13] Pierson W J, Moskowitz L. A Proposed Spectral Form for Fully Developed Wind Seas Based on The Similarity Theory of S. A. Kitaigorodskii [J]. J. Geophys. Res., 1964, 69(24): 5 181 - 5 190.

[14] Durden S, Vesecky J. A physical radar cross-section model for a wind-driven sea with swell [J]. IEEE Journal of Oceanic Engineering. 1985, 10(4):445 - 451.

[15] Hasselmann K, Olbers D. Measurements of wind-wave growth and swell decay during the Joint North Sea Wave Project (JONSWAP), Ergänzung zur Deut. Hydrogr. Z., Reihe A, 1973, 12(8): 1 - 95.

[16] Mitsuyasu H, Tasai F, Suhara T, et al. Observations of the power spectrum of ocean waves using a cloverleaf buoy [J]. J. Phys. Oceanogr., 1980, 10: 286 - 296.

[17] Hasselmann K, Sell W, Ross D B, et al. A Parametric Wave Prediction Model [J]. J. Phys. Oceanogr., 1976, 6(2): 200 - 288.

[18] Hwang P A, Teague W J, Jacobs G A, et al. A statistical comparison of wind speed, wave height, and wave period derived from satellite altimeters and ocean buoys in the Gulf of Mexico region [J]. J. Geophys. Res., 1998, 103(C5), 10 451 - 10 468, doi:10.1029/98JC00197.

[19] Chen G, Bertrand C, Robert E, et al. A Global View of Swell and Wind Sea Climate in the Ocean by Satellite Altimeter and Scatterometer [J]. J. Atmos. Oceanic Technol., 2002, 19, 1 849 - 1 859.

[20] The WAMDI Group. The WAM Model—A Third Generation Ocean Wave Prediction Model [J]. J. Phys. Oceanogr., 1988, 18(12): 1 775 - 1 810.

[21] Gilhousen D B, Hervey R. Improved Estimates of Swell from Moored Buoys [J]. Proc. Fourth Int. Symp. WAVES 200, Alexandria, VA, ASCE, 2001, 387 - 393.

[22] Young I R. Wind Generated Ocean Waves [M], Elsevier Science Ltd,1999.

风浪和涌浪分离方法的比较

李水清，赵栋梁

（中国海洋大学 物理海洋研究所 山东 青岛 266100）

摘 要：海浪通常以风浪和涌浪混合的形式存在，如何进行分离风浪和涌浪一直是海浪理论研究和海洋工程应用中的重要问题。本文利用模型试验和实测资料，对目前提出的一种二维谱风涌浪分离方法（2D法）和三种一维谱风涌浪分离方法（PM法、WH法、JP法）进行了检验，分析发现：2D法给出的结果整体而言最为可靠，与2D法相比，PM法明显高估了风浪成分，WH法低风速时高估了风浪，高风速时跟2D法比较接近，而JP法在整体上高估了风浪成分。通过调整分割频率的比例系数，改进了PM法，改进后的PM法给出的分离结果与2D法最为一致。

关键词：风浪；涌浪；分离；海浪频谱

Analysis of tidal and residual currents across semi-enclosed bay mouth based on shipboard ADCP measurements

LI Xi-bin[1, 2], SUN Xiao-yan[3], YAO Zhi-gang[4, 5]

1. *Tianjin Marine Environmental Monitoring Central Station, State Oceanic Association (SOA), Tianjin* 300451, *China;*

2. *Tianjin Marine Environmental Monitoring and Forecasting Center, Tianjin* 300451, *China;*

3. *National Marine Data and Information Service, Tianjin* 300171, *China;*

4. *College of Physical and Environmental Oceanography, Ocean University of China, Qingdao* 266100, *Shandong province, China;*

5. *Physical Oceanography Laboratory, Ocean University of China, Qingdao* 266100, *Shandong province, China;*

Abstract: Based on 25 hours shipboard ADCP measurements across semi-enclosed bay mouth(Kemen Channel), time series of tidal currents over 12 sites, which distribute evenly along the transect, were constructed to improve our understanding of tidal characteristics and residuals in this region. The tidal currents in Kemen Channel were identified as the regular semidiurnal and reversing tidal flows, with its behaviour more like standing waves. Moreover, the flood currents in the lower layers were found to be ahead of that in the upper layers and vice versa for ebb tides. The major of tidal ellipse for M_2 constituent was found to be larger close to the southern side of the channel, with its incline also increasing toward the south. The signs of M_4 constituent were also found mainly nearby the end points of this transect, indicating the importance of nonlinearity in tidal dynamics due to the shallower topography. A two-layer structure was found for the residual currents in Kemen Channel, flowing northeastwardly out of the Bay in upper 20 m and southwestwardly into the bay in the lowers. Besides approximate 4.81×10^8 m^3 water exchanges were determined between the Luoyuan Bay and outer seas by the calculation of tidal flux through Kemen Channel.

Keyword: shipboard ADCP; tidal currents; residuals; tidal transport

Luoyuan Bay (26°19' to 26°31' N, 119°34' to 119°50' E) is located in the northeast of Fujian province, whose Geographic characteristics distribution were shown in Fig. 1. Luoyuan Bay is surrounded by mountains, only through the northeastern part of Kemen

Received on Sept. 3, 2012

Corresponding author: luckysunxy@126.com

channels connecting to the East China Sea. As the only connection of Luoyuan Bay and open sea, Kemen channels show northeast-southwest direction substantially, with terrain undulating, and the depth range is approximately 20 m to 80 m; Along the southwest into the bay, Luoyuan Bay is overall widened and folded along the northwest-southeast direction, it is a typical semi-enclosed bay type with big mouth and small belly [1,2]. As the only connection of the inside and outside of bay water, the Kemen channels plays a key role in the process of water and material exchange. Structure and property studies of transect tides and residual currents will help better understanding of the entire long-term hydrodynamic environmental and material transport processes in Luoyuan bay.

ADCP(coustic Doppler Current Profile) calculates velocity and direction of water flow by observing the movement of scatterers suspended in seawater, whose accuracy is much higher than the traditional way. In addition, the ADCP observations also give finer vertical distribution of water currents, which can constitute a space-time continuous sequence of sea currents observation [3,4]. This allows us to have a more completed and detailed understanding of flow structure in Kemen channels. Therefore, the main objective of this article is to separate the tidal and residual signals and analyze the structures and properties of tidal and residual currents based on shipboard ADCP observation data of Kemen channels transect, in order to improve our understanding hydrodynamics of Luoyuan Bay estuary.

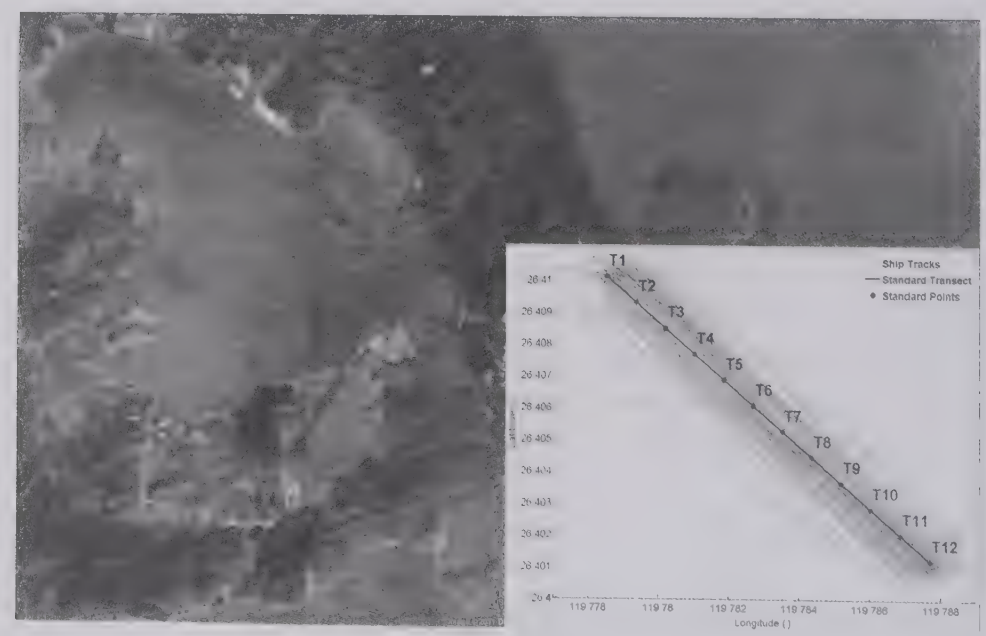

Fig. 1 Geographical features of Luoyan Bay and shipboard ADCP track

1 Data and processing

Data analyzed in this paper is from 25 hours, continuous shipboard ADCP observation of Kemen channels transect by Ocean University of China during the time period of 13:28 on Sept. 28, 2005 to 15:13 on Sept. 29, the location of the transect is as shown in Fig. 1. The direction of the transect is basically perpendicular to the water spindle direction. The observation instrument is the 307.2 kHz WorkHorse series ADCP from the US. RDI Company. Vertical direction includes a total of 30 measured layers with thickness of 2 m, and 1 minute short-term average data is selected for analysis. Observation section width of Luoyuan Bay mouth is about 1.5 km, and sailing speed underway is approximately 2 to 2.5 m/s. The single trip require about 10 mins. Data quality control includes sailing speed calculation by combining bottom tracking and DGPS, excluding the abnormal values and data Percent Good less than 80%, and all missing data were interpolated. Through quality control, standard section is divided into 11 parts and 12 standard points (T1 to T12 see Fig. 1). In this paper, the follow-up analysis is based on equal interval sea current observations with time series in 12 standard points.

2 Time series

Tidal current with time series from 12stations (T1 to T12) showed similar space distribution characteristics. T5 station with the deepest water depth was done time series analysis, and results are shown below(see Fig. 2). In 22 hours from 17:00 on Sept. 28, 2005 to 15:00 the next day, tidal level with time series of T5 station showed two high levels(20:00 on Sept. 28 and 8:00 the next day) and two low levels (2:00 on Sept. 28 and 14:00 the next day), and time interval of the two adjacent wave crests was about 12.5 hours, which displayed regular semidiurnal tidal characteristics.

During high tide(14:00 to 20:00 on Sept. 28th and 2:00 to 8:00 the next day), tidal current flowed southwestward and entered the bay, average high tidal flow direction is about 210°. During low tide(20:00 on Sept. 28 to 2:00 the next day and 8:00 to 14:00 the next day), tidal current flowed northeastward away from the bay, and average low tidal flow direction was about 30°. The high and low tidal directions were basically along the axial direction of the Kemen channel, and tidal current at the bay mouth was mainly the transmeridional U component with maximum value about 0.4 m/s, and the north-south V component was relatively weak with value only about 0.2 m/s. In additon, tidal currents displayed two high tides and two low tides within 25 hours, it is regular semidiurnal tide. The maximum velocity of high tidal flow was about 0.5 m/s, three hours before the

climax(17:00 on Sept. 28 and 5:00 the next day); The maximum velocity of low tidal flow was about 0.4 m/s, three hours after the climax(23:00 on Sept. 28 and 11:00 the next day), so the maximum flow velocity appeared at half-tide level moments and minimum flow velocity appeared at the high and low tide time. Standing wave characteristics were obvious, above all, they were consistent with the semi-enclosed bay tidal wave characteristics.

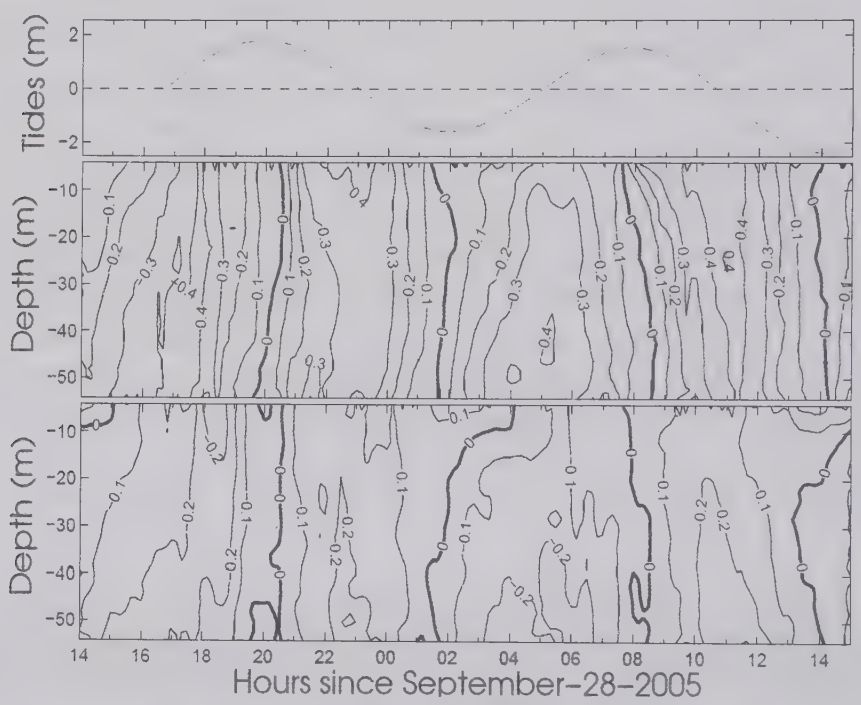

Fig. 2 Tidal level(up), transmeridional U component (middle) and north-south V component(low) distribution with time series

From the vertical direction, the spacial distribution of flow velocity is not even. Generally, the high value of high tidal current appeared in the middle and low area, high tidal current velocity was weaker near the surface. For ebb current, ebb current velocity was higher in the middle and up area, especially near the surface area, and ebb current velocity was weaker in the low area. As a whole, high tidal current velocity was slightly higher than the ebb current velocity. Along the vertical direction the occurrence of high tide and low tide also displayed inconsistent, which can be seen from the triangular structure of the velocity isopleth map. During flood tide, water in the low area of Kemen channel first began to flow, after about 0.5 to 1 hours water in the surface area began to flow. As a whole, the ebb tide time was longger than the high tidal current in the surface area, and the bottom area is the opposite.

3 Residule current

The previous analysis has shown that the tidal current in the area of Kemen channel was M2 tidal component with 12.42 hours cycle, and other tidal component proporation was smaller. Thereby, by averaging 25 hours current with time series, after eliminating and suppressing most of the tidal signals in the observational data, the spatial distribution of the residual current of the Kemen channel cross sections was obtained. The result is as shown in Fig. 3.

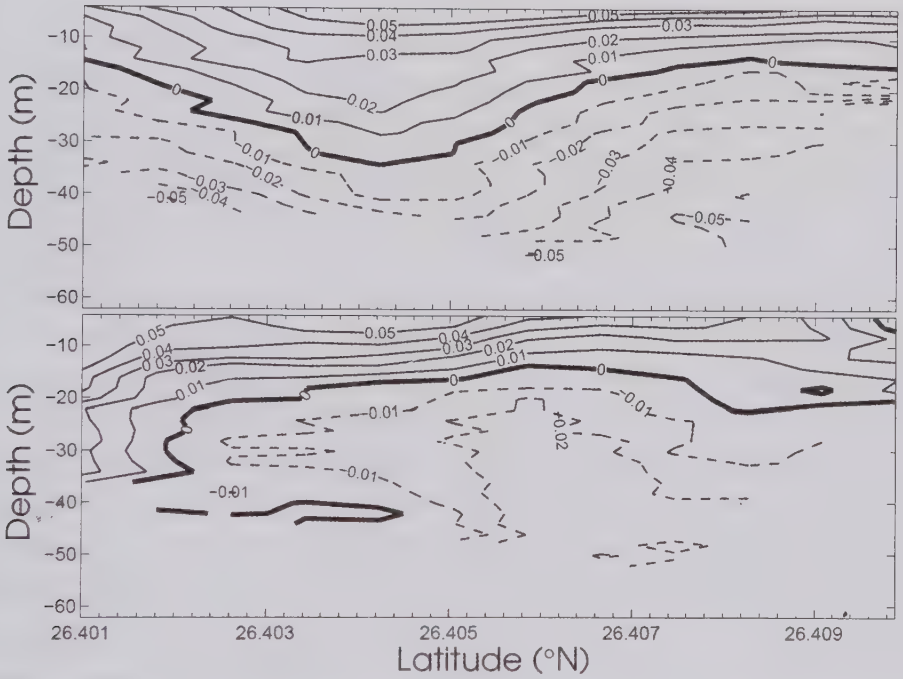

Fig. 3 Transmeridional U component(up) and north-south V component(low) of residual current structure of Kemen channel cross section

(Wherein, the solid line represents the velocity component is positive(U eastward, V northward), and the dotted line represents the velocity component is negative(U westward, V southward), and the black thick line represents zero velocity.)

The transmeridional U component of residual current distribution displayed basically two-layer structure on the vertical direction. In the upper layer, water flowed eastward, towards outside the bay, and the core outflow area was located the surface area near 26.404°N, where near the south tip of the channel. And to the north of the core outflow area, eastward outflow distribution in the horizontal direction is relatively uniform and isopleth is

rather straight. In the middle and lower layers of channel water flowed uniformly westward, that flowed into the bay. And there were two core areas that water flow westward, which located at 26.402°N and 26.408°N, respectively near the bottom area, in which, flow in the north core area of 26.408° was stronger than the south one, especially area of the flowing. This indicates that the west inflow of Kemen channel flowed into the Luoyuan bay mainly through the middle and lower regions of the north side of the channel. Possible reason of this phenomenon is due to the role of the coriolis force in the northern hemisphere, which made the flood tide into the bay converging at the northwest side of the channel and the ebb tide out of the bay converging at the southeast side of the channel. Therefore, the upper outflow district position was southward.

Two-layer structure on the vertical direction of the north-south V component of residual current was sill visible basically, especially obvious at the north side area of the channel. However, some area of southernmost to 26.402°N displayed northward outflow at all the depths, and amplitude of the northward outflow weakened with water depth increasing. In the area near the surface, intensity of northward outflow was about 0.05 m/s, and near the bottom area, its intensity decreased approximately 0 m/s. Area from 26.402°N to the north of the northernmost, the depths that northward outflow could reach were basically consistent. It was about 20 m, and horizontal distribution of northward outflow was relatively uniform, and only that in the northernmost area of the channel showed a certain horizontal change. The core inflow area of north-south V component mainly appeared in the region where depths were deeper than 20 m from north of 26.402°N to the northernmost, and the core position of inflow area was near the 26.408°N bottom area, which was basically consistent with transmeridional inflow. The north-south outflow intensity of Kemen channel was close to the transmeridional component, and maximum value was about 0.05 m/s. While the inflow was somewhat different, and maximum inflow intensity was about -0.03 m/s along the north-south direction of the Kemen channel, and obviously it was weaker than transmeridional inflow intensity -0.05 m/s. Furthermore, there was only one inflow core area of north-south component along the cross section direction, which was also different from transmeridional component.

Overall, along the transect, northeast outflow was mainly concentrated in the upper layer and shallower area whose depth less than 20 m, and the outflow core position was to the south of the channel, and intensity of northeast outflow was a bit stronger but inflow area was relatively small; However, southwest inflow mainly located in the middle and lower layers, and the core inflow position located near the bottom of the northern channel, and the intensity of southwest inflow was relatively weak but the inflow area is relatively larger.

For further revealing distribution characteristics of residual field, vertical distribution of residual vector along cross section was given, and results were as shows in Fig. 4. We can see that basically the middle and upper layers were northeast outflow, and outflow direction was about 40° - 80° basically along the channel axis direction in most area except T1 and T2 stations. However, inflow southwest with direction about 190° - 230° was mainly located in the middle and lower layers at the north side of the channel, basically opposite to the major inflow direction. For the vertical distribution of residual vector, residual vector inside Kemen channel basically displayed Clockwise rotation with depths except some rare stations of both ends, which was related to the effect of Coriolis force in the northern hemisphere.

4 Tidal flux

During the observation, tidal flux through the entire transect was calculated based on the 25 hours, tidal currents with time series, and was compared with previous results. By tidal flux observation the following formula was used to calculate:

$$T = \int_{t=t_{Start}}^{t=t_{End}} \int_{z=Z_{Bot}}^{z=0} \int_{x=0}^{x=x_{Total}} \int_{y=0}^{y=y_{Total}} (u \cdot dx + v \cdot dy) \cdot dz \cdot dt$$

In the formula, t_{Start} and t_{End} stand for the starting and ending time of the observation; dt is observation time interval, defined as 10 mins; Z_{Bot} stands for depths of observation section, dz is thickness of vertical unit, defined as 2 m; x_{Total} and y_{Total} are the east-west and north-south lengths of the observation transect. By calculation, we got tidal flux sequence along the time integral cross the channel section. Results are as shown in Fig. 5.

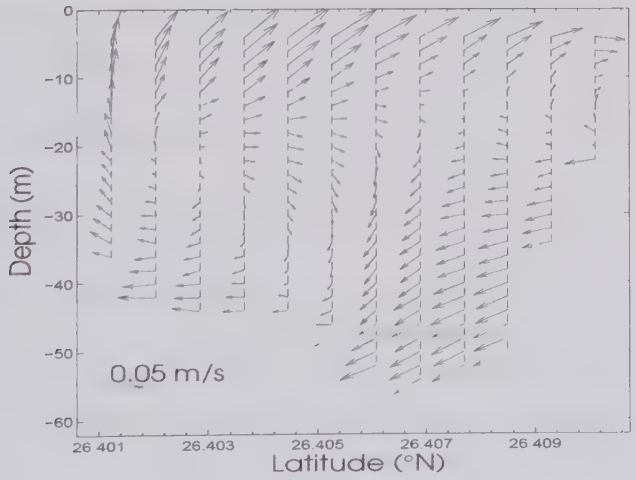

Fig. 4 Residual vertical vector of Kemen channel cross the section

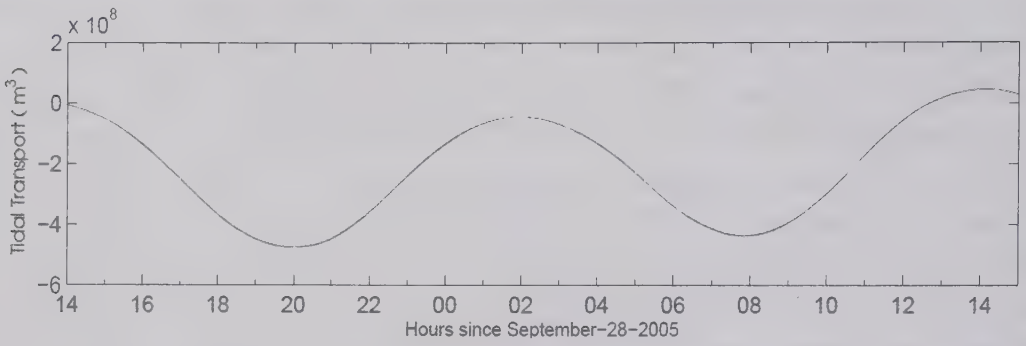

Fig. 5 Cumulative tidal flux along the cross-section integral, and that flowing into the bay is positive

From 20:00 on Sept. 28, 2005 to 02:00 next day, tidal flux into the bay was about 4.32×10^8 m^3. From 2:00 to 8:00 on Sep. 29, 2005, tidal flux out of the bay was 3.92×10^8 m^3. From 8:00 to 14:00 of the same day, tidal flux into Luoyuan bay reached the observation maximum value, approximately 4.81×10^8 m^3.

5 Conclusion

Based on 25 hours, shipboard ADCP measurements across Kemen channel, time series of tidal currents over 12 sites(T1 to T12) were constructed. Tidal current, risidual current and tidal flux of Luoyuan channel section were analyzed based on tidal current with time series from 12 stations(T1 to T12), and results are as follows:

(1) Water current of Kemen channel cross section was dominated by tidal currents, which displayed two complete high and ebb tides with 25 hours, and it had obvious regular semidiurnal tidal characteristics. Tidal velocity was minimum during high and ebb tide moments, which showed obvious standing wave feature. High tides first displayed near the middle and low layer of the channel, but ebb tides occurred in the near surface area, and time of ebb tidal currents was longer in the surface and the lower area is opposite.

(2) Residual currents of Kemen channel displayed two-layer structure on the vertical direction, which flowed northeastward out of the bay in the upper layer with water depth shallower than 20 m, and the position of core outflow area was slightly to the south; Residual currents displayed southwestward flowing into the bay in the middle and lower layer of the channel, and the position of inflow core area was comparatively to the north side of the channel. Spatial distribution of the inflow and outflow core position should be related to the influence of the Coriolis force.

(3) Estimation of tidal flux indicates that tidal flux in the Luoyuan bay through the observation transect was about 4.81×10^8 m^3

References

[1] Bay records editorial committee of China, Bay records of China: The seventh Fascicule [M]. Beijing: Ocean Press, 1994: 49 - 92.

[2] Wang A J, Ye X, Chen J. Effects of typhoon on sedimentary processes of embayment tidal flatA case study from the"Fenghuang" typhoon in 2008 [J]. Acta Oceanologica Sinica, 2009(6): 77 - 86.

[3] Instruments R D. ADCP coordinate transformation: Formulas and calculations [J]. RDI Manual; 1998.

[4] Gordon R L. Instruments R D. Principles of Operation a Practical Primer [J]. RD Instruments, San Diego, 1996.

基于船载 ADCP 观测对半封闭海湾湾口断面潮流及余流的分析

李希彬[1,2]，孙晓燕[3]，姚志刚[4,5]

（1. 国家海洋局天津海洋环境监测中心站，天津 300451；2. 天津市海洋环境监测预报中心，天津 300451；
3. 国家海洋信息中心，天津 300171；4. 中国海洋大学 海洋环境学院，山东 青岛 266100；
5. 中国海洋大学 物理海洋教育部重点实验室，山东 青岛 266100）

摘 要：基于对罗源湾可门水道的25小时连续走航ADCP观测，本文成功构建了沿走航断面共12个站位的连续海流时间序列，并对这些站位的潮流、余流以及潮通量等进行了分析。结果表明可门水道内的潮流为正规半日潮流，驻波性质明显，涨潮首先出现在水道中下层而退潮则首先发生在水道上层。水道内潮流为往复流，水道南部M_2分潮流流速较大，并且其倾角自北向南逐渐增加。此外，水道两端的浅水区域内浅水分潮M_4振幅较显著。可门水道内余流呈现出两层结构，20 m以浅余流沿东北向流出海湾，并且出流的核心位置偏南，而20 m以深的余流沿西南向流入湾内，入流的流核位于偏北的近底层区域。对潮通量的积分计算表明通过可门水道进入罗源湾的潮通量约为4.81×10^8 m^3。

关键词：走航ADCP；潮流；余流；潮通量

An approach to estimate tidal dissipation with single-point high-frequency ground wave radar data

MAO Hua-bin, CHEN Ju, QIU Chun-hua, LIAN Shu-min

State Key Laboratory of Tropical Oceanography, South China Sea institute of Oceanology, CAS, Guangzhou 510301, Guangdong province, China

Abstract: Using the single-point ground wave (GW) radar data at Shensi Station and the water level data at three stations (Shengsi, Luchaogang and Daishan), the authors obtained the flow vectors from the radial velocity of GW radar observation, and calculate four sub-tidal harmonic constants (O_1, K_1, M_2 and S_2). The tidal characteristics derived from the GW radar dataset agreed well with those from the tidal gauge data. The authors also analyzed the tidal energy flux and tidal energy dissipation rate. There was a good relationship between the tidal energy dissipation rate and topography. The study showed a good way to calculate tidal energy dissipation rate using GW radar data.

Keywords: ground wave radar; characteristic value; tide type; tidal energy flux; tidal energy dissipation

Introduction

Ground wave (GW) radar with high-frequency radar wave is one of the marine environment remote sensing techniques. Since GW radar has relative high frequency electromagnetic waves and sea water conducts electric very well, the diffraction from GW radar achieves to the sea surface much farther than stadia, in a way of vertical polarization. High-frequency GW (HFGW) radar can measure the near-surface current, wind and wave.

Compared with the traditional equipments, this approach covers longer and wider range, observing more parameters and working under all-weather condition; compared with ocean satellite, it has lower expense, higher accuracy and higher spatial/temporal resolution. Therefore, GW radar deserves our attentions. Previous studies on the GW radar lead development of the GW radar ocean remote sensing [1,2]. In 1990s, GW radar reaches a relative high level in terms of techniques and capabilities with the improvement of electric, signal procession and computer. Nowadays, there are tens of GW radars along the coastal area. The flow data retrieved from GW radar will be used widely in the near

Received on May 16, 2012

Corresponding author: maohuabin@scsio.ac.cn

future.

Zhou and Yang[3] retrieved the ocean surface velocity vectors by using two radial velocity maps measured by both radars. They interpolated the radial velocities into the common grids in the polar coordinates and their results were consistent with altimetry results. Zhu et al.[4] calculated the radial velocity using OSMAR GW radar, finding that the spatial distributions of M_2 sub-tidal amplitude and phase were similar with those from former studies.

Internal wave generated from continental shelf not only plays a very important role in the energy balance of global ocean but also provides energy to the local oceanic mixing [5]. Nash et al.[6] observed the internal tidal propagation, reflection and internal wave mixing off Virginia during May and June 1998. They found that at semidiurnal frequency, a divergence of high-wavenumber offshore energy flux almost balanced onshore energy flux.

Zhang et al.[7] calculated the M_2 sub-tidal energy flux in the complicated topography area of Pacific, using 10-year altimetry data, Levitus data and dynamic model data. Li et al.[8] investigated the tidal energy flux and tidal energy dissipation in Bohai Sea, Yellow sea and East China Sea, by assimilating altimetry and tidal gauge data.

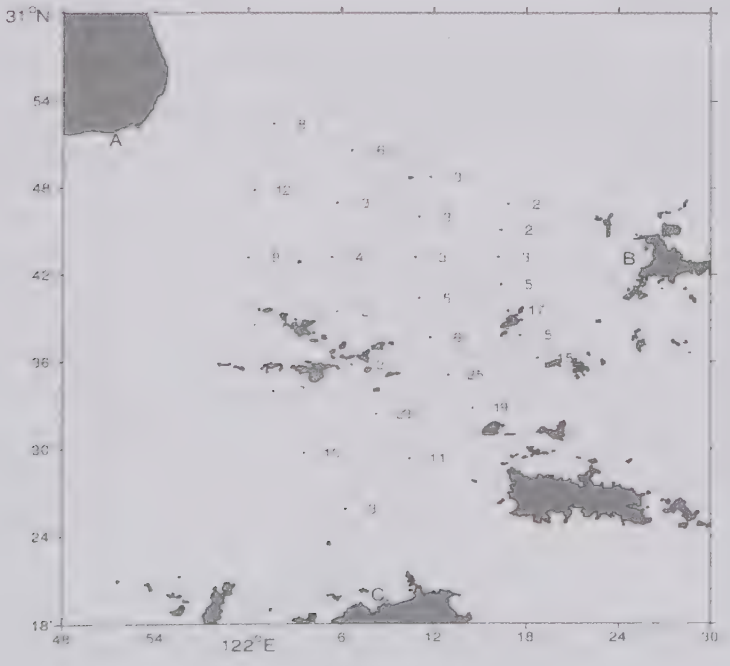

Fig. 1 Observation stations

(The number denotes the water depths, and A, B and C denote the Luchaogang , Shengsi , and Daishan stations, respectively).

In this study, we made a try to derive tidal energy flux and tidal energy dissipation from GW radar data. Firstly, we retrieved the velocity vectors based on the GW radar data in Shengsi Island, Hangzhou Bay. Secondly, we approached the velocity and the delay angle of M_2 sub-tide and S_2 sub-tide, and finally we got the tidal energy flux and tidal energy dissipation. Data and methods are discussed below; section 2 explains the results and section shows is the discussion and conclusions.

2 Data and methods

2.1 Data

Radial velocities were derived from HFGW radar measurements at Shengsi Island (Fig. 1). It covered 120°-120°30′E, 30°24′-30°54′N from Aug. 23 to Sep. 26, 2007. The temporal was 389s, the radial was 10 km, and the angle resolution was 10°, respectively. We also compare the tide gauge data with 1h resolution at Luchao, Shengsi and Daishan stations. The topography data from chart are interpolated.

2.2 Methods

2.2.1 Current vectors

The GW radar only measures the radial velocity. The real tidal velocity vector includes not only the radial velocity but also the tangential velocity. It is inaccurate to get the tidal energy balance only using radial velocity. Therefore, we need to retrieve the velocity vectors.

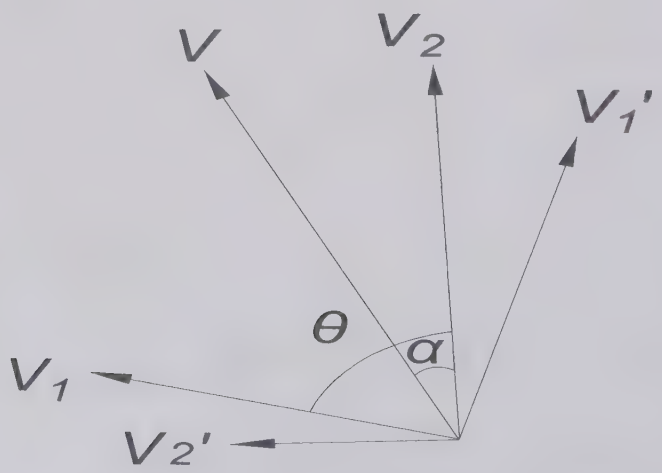

Fig. 2 Decomposition of velocity vector diagram

Considering the facts that the two adjacent stations are close; time interval of GW are very short and the radial velocity are estimated using the total echoes in each pixel, we assume the radial velocities at two adjacent stations are the two components of one vector(Fig. 2). This method has once been applied to retrieve the geostrophic velocity by altimetry data in the cross region:

$$V_1 = V \cdot \cos(\theta - \alpha) \ , \tag{1}$$

$$V_2 = V \cdot \cos(\alpha) \, , \tag{2}$$

where V_1 and V_2 are the radial velocity at two adjacent stations; V_1' and V_2' are the tangential velocity; V is the vector velocity, θ is the angle between two point, α is the angle between V and V_2.

From Eqs. (1) and (2), the real velocity is

$$V = \frac{V_2}{\cos\left\{ arctg\left(\frac{V_1 - V_2 \cdot \cos\theta}{V_2 \cdot \sin\theta}\right)\right\}} \tag{3}$$

$$\alpha = arctg\left(\frac{V_1 - V_2 \cdot \cos\theta}{V_2 \cdot \sin\theta}\right) \tag{4}$$

2.2.2 Harmonic constants and tidal characteristics

We used the 'T_tide' toolbox to get the amplitude and phase of sub-tidal components(O_1, K_1, M_2 and S_2) at Luchao, Shengsi and Daishan tidal gauges. We derive the harmonic constants through analyzing the tidal velocity vectors. Following Chinese 'Code of Hydrology for sea harbor'[9], tidal characteristics are determined by $\lambda = (H_{O_1} + H_{K_1}) / H_{M_2}$, where H_{O1}, H_{K1}, H_{M2} are the major axis of elliptical tide for O_1, K_1, M_2. There are four types of tides on the basis of tidal characteristics: 1) $\lambda \le 0.5$, regular semidiurnal tide; 2) $0.5 < \lambda \le 2.0$, irregular semidiurnal tide; 3) $2.0 < \lambda \le 4.0$, irregular diurnal tide; 4) $4.0 < \lambda$, regular diurnal tide.

2.2.3 Tidal energy flux and tidal energy dissipation

Although GW radar measures sea surface velocity without the vertical structure of velocity, the study area is very shallow. We assume that the shallow ocean is one box, which means the velocity is uniform in each layer.

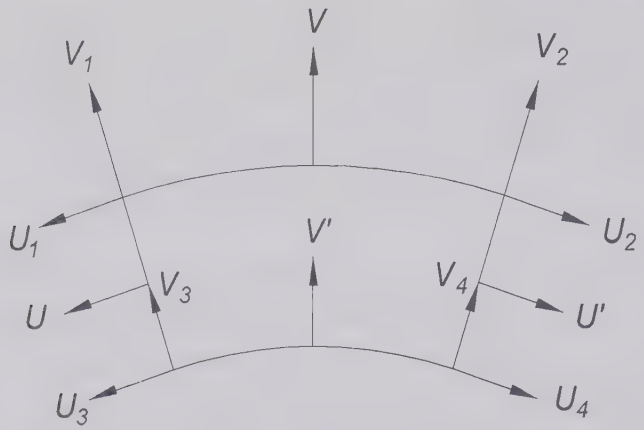

Fig. 3 Schematic of tidal energy flux algorithm

Fig. 3 shows the schematic of tidal energy flux algorithm. We use four stations to calculate the tidal energy flux. The radial velocity is $V=(V_1+V_2)/2$ and $V'=(V_3+V_4)/2$, and the tangential velocity is given by $U=(U_1+U_3)/2$ and $U'=(U_2+U_4)/2$. The lateral area is $S_{12}=(h_1+h_2)*\overline{12}/2$, where h_1 and h_2 is the water depth at station 1 and station 2, and $\overline{12}$ means the arc length between station 1 and station 2. The tidal energy is $E=0.5*V^2$, and then the tidal energy flux in each side is $\phi_e=V*S*E$. ϕ_e is positive(negative) when the water flow into(out of) the study area. The tidal energy dissipation is given by $\phi=\langle\phi_1+\phi_2+\phi_3+\phi_4\rangle$, where $\langle\ \rangle$ means time average.

Tab.1 Harmonic constants of three tidal stations

station	O_1		K_1		M_2		S_2		Characteristic value
	Amplitude / cm	Phase / °	Amplitude / cm	Phase / °	Amplitude / cm	Phase / °	Amplitude / cm	Phase / °	
Luchao	20.72	172	33.77	223	151.73	329	54.28	39	0.36
Shengsi	18.52	159	30.50	207	114.48	277	49.98	340	0.43
Daishan	20.51	171	31.90	222	104.87	296	41.06	358	0.49

3 Results

3.1 Velocity vectors

Fig. 4a shows the original radial velocity from GW radar. The westward velocity around 30°42′N (-1.6 m/s) is a little larger than the surrounding velocities. Fig. 4b shows the retrieved velocity vectors. The water flows westward and converges into the bay. The velocity vectors are consistent with that under high tide condition in Hangzhou bay [10].

3.2 Harmonic analysis results

Four sub-tidal harmonic constants at each station are listed in Tab. 1. All of the tidal characteristics are between 0.28 - 0.47, which indicates that all over the stations are affected by the regular semidiurnal tides. The maximum major axis of ellipses is 1.28 cm (at station 11). The harmonic constants from tidal gauges also show that regular semidiurnal tides domain Luchao, Shengsi and Daishan stations (Tab. 2). Their tidal type is consistent with that from tidal gauge datasets [11].

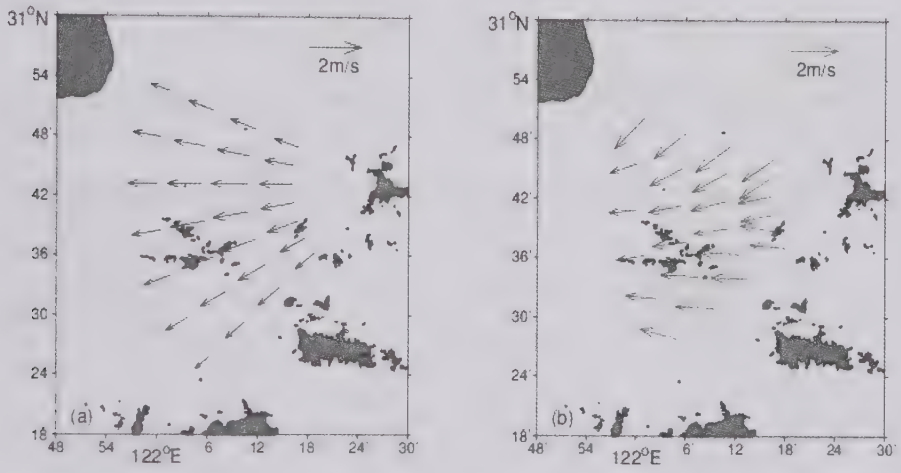

Fig. 4 Monthly averaged map of (a) the original radial velocity and (b)the retrieved flow vectors

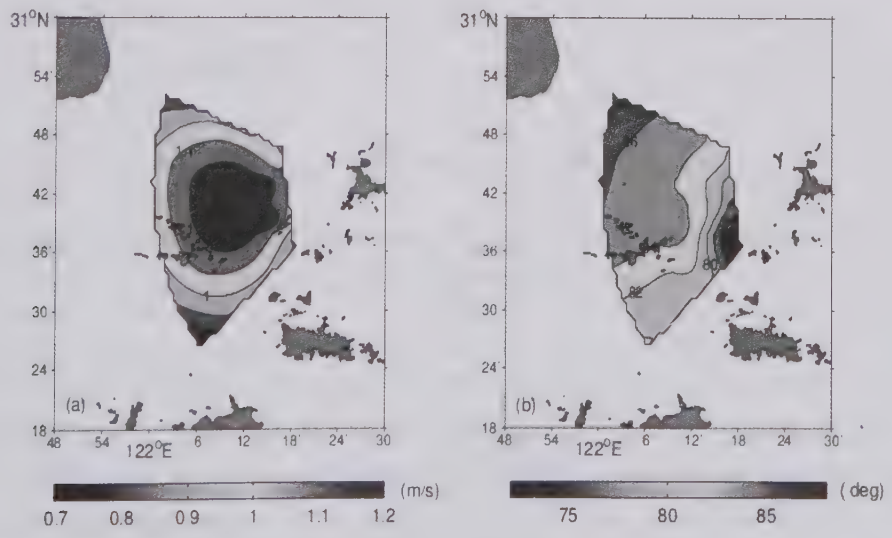

Fig. 5 Distributions of M_2 sub-tidal (a) velocity magnitude and (b) phase-field

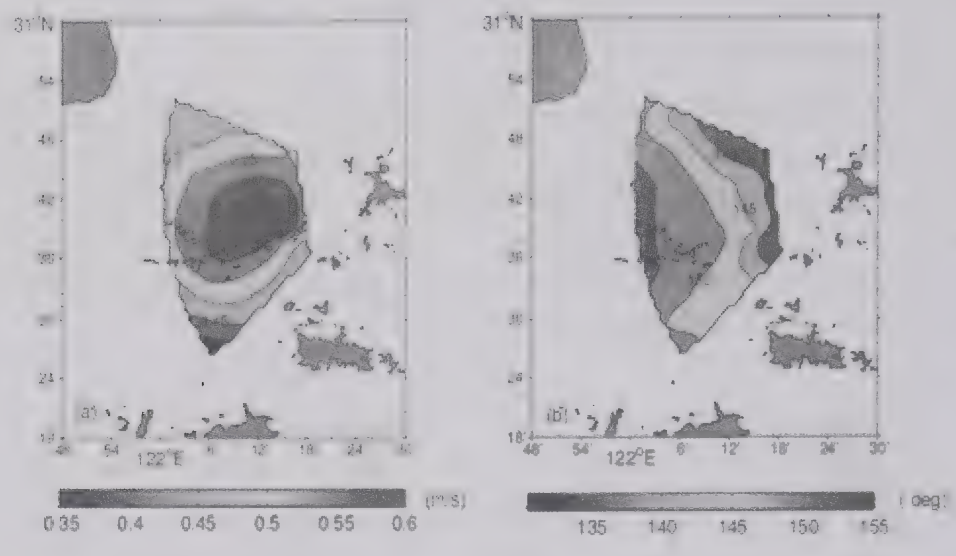

Fig. 6 Distributions of S2 sub-tidal (a) velocity magnitude and (b) phase-field

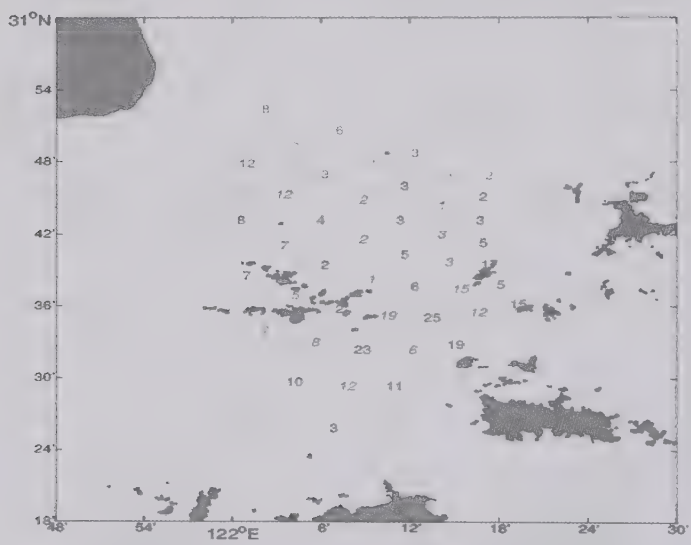

Fig. 7 Distributions of tidal energy dissipation rate(unit:104 m^3/s) (red number), and the water depth (blue number)

Since the semidiurnal tide domains the study area, we pay attention to the M_2 and S_2 sub-tidal components. Fig. 5a shows the sub-tidal velocity magnitude has a 'Sandwich' structure, which has maximum magnitude in the middle and minimum magnitude at the edge of the study area. It may result from the topography. When closer to the islands, the water depth becomes shallower and the velocity becomes smaller. The maximum velocity is 1.28cm/s. Fig.5b shows the M2 sub-tidal phase distributions. The higher phase in

northwest and lower phase in southeast indicate that the M_2 sub-tidal component flows into Hangzhou bay from southeast to northwest. Fig. 6a shows the S_2 sub-tidal velocity magnitude, which has the same pattern with M_2 sub-tidal component. The maximum velocity of S_2 is 0.63 cm/s. Fig. 6b is the S_2 sub-tidal phase distribution. The S_2 sub-tidal propagates westward from northeast.

Tab. 2 Harmonic constants of observation stations

station	O_1		K_1		M_2		S_2		Characteristic value
	Major axis/m	phase-lag/°	Major axis/m	phase-lag/°	Major axis/m	phase-lag/°	Major axis/m	phase-lag/°	
1	0.154 7	237	0.142 7	289	0.835 3	72	0.432 0	134	0.36
2	0.157 6	247	0.171 1	287	0.994 2	72	0.495 5	135	0.33
3	0.146 2	236	0.212 3	293	1.146 3	76	0.597 5	141	0.31
4	0.150 7	236	0.218 1	297	1.178 6	79	0.617 0	141	0.31
5	0.159 8	241	0.204 1	301	1.173 5	80	0.592 0	140	0.31
6	0.132 1	242	0.207 7	299	1.050 8	82	0.567 4	138	0.32
7	0.166 3	260	0.196 1	298	0.890 4	82	0.503 4	133	0.41
8	0.138 8	237	0.169 8	295	0.949 3	80	0.468 4	146	0.33
9	0.133 6	233	0.188 0	292	1.104 9	82	0.535 6	146	0.29
10	0.146 9	234	0.199 8	296	1.238 6	84	0.619 3	150	0.28
11	0.156 1	242	0.199 1	298	1.283 6	84	0.639 1	149	0.28
12	0.151 5	245	0.193 0	302	1.264 9	84	0.618 0	147	0.27
13	0.144 2	249	0.227 1	307	1.150 3	84	0.556 3	141	0.32
14	0.163 5	252	0.196 8	301	0.959 2	85	0.498 0	135	0.38
15	0.097 9	234	0.167 9	302	0.884 9	81	0.442 7	148	0.30
16	0.119 3	222	0.208 2	298	1.043 0	81	0.517 9	149	0.31
17	0.121 7	229	0.222 2	295	1.166 7	84	0.597 0	153	0.29
18	0.135 6	246	0.197 8	292	1.211 7	85	0.600 1	153	0.28
19	0.130 4	250	0.191 2	296	1.206 3	85	0.580 6	152	0.27
20	0.119 2	240	0.2054	307	1.102 7	85	0.510 9	149	0.29
21	0.108 5	242	0.207 4	294	0.911 8	87	0.467 1	142	0.35
22	0.156 9	217	0.071 9	291	0.669 5	83	0.334 6	152	0.34
23	0.152 4	233	0.100 3	282	0.858 9	81	0.428 7	150	0.29
24	0.165 4	238	0.143 4	277	0.972 8	84	0.495 3	156	0.32
25	0.171 5	231	0.147 8	288	1.004 5	86	0.528 4	157	0.32
26	0.152 4	239	0.162 8	284	1.016 5	87	0.493 6	159	0.31
27	0.101 9	248	0.224 1	305	0.959 2	87	0.476 6	153	0.34
28	0.147 6	210	0.203 7	299	0.746 7	90	0.451 6	156	0.47

3.3 Tidal energy dissipation

Fig. 7 shows the distribution of water depth and the tidal energy dissipation. The blue

numbers are the water depths and the red one are the tidal energy dissipation rates, with unit 104 m^3/s. We found the maximum tidal energy dissipation rate is 19×104 m^3/s. The smaller gradient of water depth corresponds to the smaller tidal energy dissipation rate. It indicates that the tidal energy dissipation is related to the topography.

4 Discussion and conclusions

1) We retrieve the velocity vector based on single-point GW radar radial velocity. We also compare the four sub-tidal components(O_1,K_1,S_2,M_2) from the velocity vectors with that from the tidal gauge datasets using harmonic analysis. The two datasets show the same tidal characteristics and tidal types in our study area. It indicates that the retrieved velocity vector from single-point GW radar is convincible and feasible to investigate the tidal information.

2) We assume the velocity in each layer is the same with the surface velocity. It ignores the velocity shear, but it could reflect the tidal characteristics in small scale. To get much higher accuracy, vertical structure of velocity is needed.

3) The tidal energy dissipation rate from GW radar agrees well with the gradient of water depth. In the steep continental shelf, the tidal energy dissipation rates are large; while in smooth region, the tidal energy rates are small.

Acknowledgments

This work was supported by projects (No. 40976012 and No. 40906030). We thank Professor WEN Bi-yang from WuHan University for providing the ground radar observation data.

References

[1] Ke Heng-yu, Wu Shi-cai, Yang Zi-jie, et al. Application of HF Ground Wave Radar to EEZ [J]. Journal of University of Wuhan Iron and Steel Corporation, 1999, 11(2): 23 - 30.

[2] Zhou Zhi-xin, Liu Yong-tan. Computational Method for the Extraction of Suface-Current by HF Ground-Wave-Radar [J]. Marine Science Bulletin, 1997, 16(5): 79 - 84.

[3] ZHOU Hao, WEN Bi-yang, LIU Hai-wen. Ocean Surface Vector Current Synthesization of HF Ground Wave Radar [J]. Wuhan University Journal(Natural Science Edition), 2001, 47(5): 642 - 644.

[4] ZHU Da-yong, SHAO Hao, LI Yan, et al. Quality analyses of radial currents measured by a

demonstration system of OSMAR HF radar in Fujian Province [J]. Journal of Oceanography in Taiwan Strait, 2007, 26(1): 8 - 16.

[5] Mackinnnon J A, Gregg M C. Shear and baroclinic energy flux on the summer New England shelf [J]. J. Phys. Oceanogr., 2003, 33: 1 462 - 1 475.

[6] Nash J D, Kunze E, Toole J M, et al. Internal tide reflection and turbulent mixing on the continental slope [J]. J. Phys. Oceanogr., 2004, 34:1 117 -1 134.

[7] ZHANG Xiao-qian, LIANG Xin-feng, ZHOU Lei. Estimates of M2 internal tide energy fluxes in the Pacific Ocean using TOPEX/Poseidon altimeter data [J]. Acta Oceanologica Sinica, 2005, 27(5): 9 - 14.

[8] LI Pei-Liang, LI Lei, ZUO Jun-Cheng, et al. Tidal Energy Fluxes and Dissipation in the Bohai Sea, the Yellow Sea and the East China Sea [J]. Journal of Ocean University of Qingdao, 2005, 35(5): 713 - 718.

[9] The ministry of communications of the People's Republic of China. JTJ213-98, Code for sea port hydrology. Beijing: people's traffic press, 1998.

[10] Li Shenduo, Hu Hui. A study on the current fieled of the HangZhou bay [J]. Oceanologia Et Limnologia Sinica. 1987, 18(1): 28 - 37.

[11] Chen Qian, Huang Da-ji, Zhang Ben-zhao, et al. Characteristics of the tidal current and residual current in the seas adjacent to Zhejiang [J]. Donghai Marine Science, 2003, 21(4): 1 - 14.

单点高频地波雷达资料估算潮能耗散的方法

毛华斌，陈 举，邱春华，练树民

（中国科学院南海海洋研究所 热带海洋环境国家重点实验室，广东 广州 510301）

摘 要：使用嵊泗站所布设的地波雷达观测获取的径向流数据，以及嵊泗、芦潮港、岱山3个潮汐观测站水位资料，采用两点近似投影方法反演流场全矢量流速，并用T_tide程序计算调和常数，分别计算O_1、K_1、M_2、S_2各分潮流速场及迟角场，并计算各点上的潮能通量及潮能耗散，得到嵊泗岛以西杭州湾口区域潮能耗散同地形存在良好对应关系，充分证明了采用地波雷达观测数据进行潮能耗散计算这一方法的可行性，供相关工作者作进一步研究和讨论。

关键词：地波雷达；特征值；潮汐类型；潮能通量；潮能耗散

Distribution of clay minerals in surface sediments off Yangtze River estuary

LAN Xian-hong[1,2], ZHANG Zhi-xun[1,2], LI Ri-hui[1,2], WANG Zhong-bo[1,2], CHEN Xiao-hui[1,2], TIAN Zhen-xing[1,2]

1. *The key Laboratory of Marine Hydrocarbon Resource and Geology, Qingdao* 266071, *Shandong province, China;*

2. *Qingdao Institute of Marine Geology, Qingdao 266071, Shandong province, China*

Abstract: Based on the clay minerals, content analysis from 187 stations in the surface sediments, this paper dealt with the assemblages and the distributions of clay minerals in the surface sediments off the Yangtze River estuary. The research results showed that the illite dominates the surface sediments off the Yangtze River estuary with the smectite or kaolinite the second rank and chlorite the third rank; the illite-smectite-kaolinite- chlorite-assemblage is the main type of the clay minerals assemblage in the area, with the illite-kaolinite-chlorite-smectite -type as the second rank; the source of clay mineral is mainly from the Yellow River and the Yangtze River. The Q-type cluster analysis show that sediments from both recent and ancient Yellow River were deposited mainly in the northeast part of the study area to the north of 29°30′. Substance from the Yangtze River was deposited mainly in the western and middle parts off the Yangtze River estuary.

Keywords: clay mineral; distribution characteristic; off Yangtze River estuary

The clay minerals, with fine particle structure and varied composition, are the most widely distributed minerals in the marine environment. Because clay minerals are sensitive to the changes of geological process or sedimentary environment, the source and transport paths of substances in sediments can be effectively identified by the analysis of compositions and combinations of clay minerals in the marine environment. The analysis can also reflect rock and climate characteristics in the source area [1-6].

The muddy sediments are extensively developed in the East China Sea. The clay minerals, which are diverse, widely distributed, constitute an important part of the sediments in the region that is the main carrier of information ofthe various geological processes. The study on the type, combinations and distribution characteristics of the clay minerals can provide the provenance, formation environment and other important

Received on July 10, 2012

Corresponding author: lanxh@qingdaonews.com

information. Prior to this, many researchers study the clay minerals of the East China Sea that has accumulated a wealth of information and achieves many important results [7-13]. Zhu et al.'s study [9] showed that the distribution characteristics of the clay mineral in sediments of the East China Sea are mainly dominated by provenance into the sea and hydrodynamic role of sea area. The sediments from the continental shelf of the East China Sea are formed by the huge amount sands that are brought by the Yellow River, Huaihe River, Yangtze River and other rivers in the continent of China. Sediments are diffusion and deposition to the outer continental shelf constantly because of the entrancing of currents. The north of the study area is mainly affected by the Yellow River, the abandoned Yellow River and the Huaihe River, and the south of the study area is mainly affected by both recent and ancient Yangtze River, and clay minerals of the Trough area are partially from volcanic eruption. The fine-grained materials of the Yangtze River estuary into the sea are migration and diffusion to the East and southwest of the study area as well as the fine-grained materials of the Yellow River eastward into the northern Yellow Sea, by entering the western South Yellow Sea into the East China Sea [10].

The results of previous studies established the overall understanding of the clay minerals in the sediments of the Yangtze River estuary and adjacent areas, and also provided more optional research methods to present researchers. The National Land Resources and Geological Survey comprehensively analyzed and studied on the clay mineral distribution in surface sediments off Yangtze River estuary, then it obtained large amounts of data that explored the source of sediments in the study area.

1 Sample collection and analysis methods

1.1 Sampling and processing

From August to September 2006, the sediments off Yangtze River estuary are sampled and collected by box-type sampler. The content analysis of the clay minerals from 187 stations in the surface sediments was analyzed in the laboratory (Fig.1).

The extraction method of the clay minerals was determined based on muddy components of the surface sediment samples. About 40 g - 70g samples were placed into a 2 000 mL beaker with distilled water. After washing and stirring, the samples with distillation water became a suspension. For the samples containing more organic matter. amount of hydrogen peroxide should be used to remove organic matter first. At last, clay component of <2 μm was extracted according to Stokes' Sedimentation Theory.

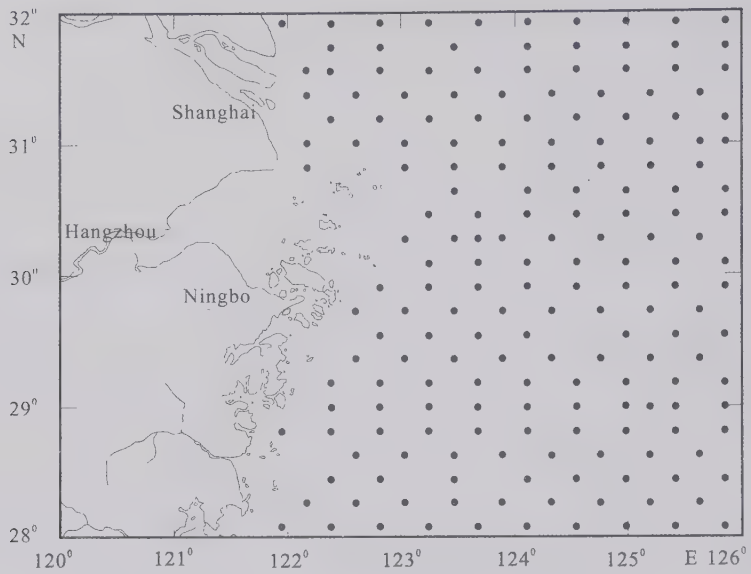

Fig. 1 Location of the sampling stations of clay minerals

The extracted clay component was made of glycerol saturated directional pieces and natural directional pieces. The remaining of the clay component was retained to prepare for other tests and verification purposes. The contents of iron and calcium of samples were not high, and the samples treated by hydrogen peroxide could be fully dispersed as far as possible to maintain the original characteristics of clay minerals, so the removal of iron and calcium handling was ignored.

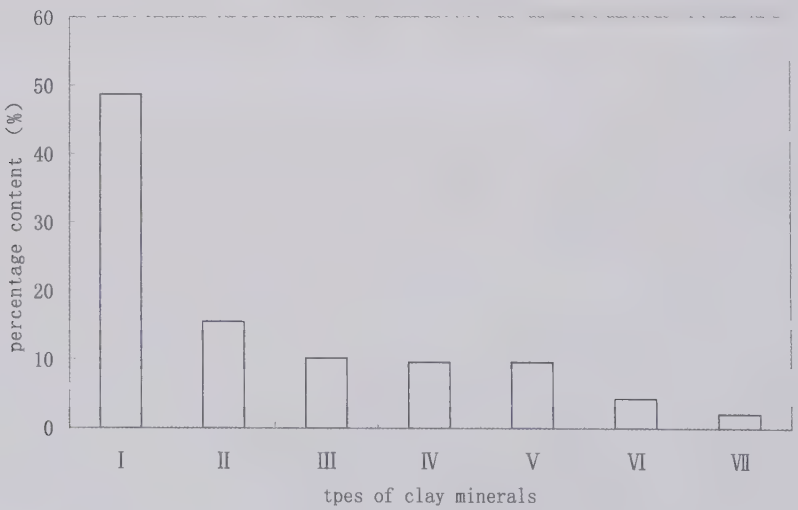

Fig. 2 Assemblages of clay minerals in the surface sediments

1.2 The analytic identification in the X-ray diffraction of clay minerals

The analytic identification in the X-ray diffraction of clay minerals using high-power Japan Rigaku D / Max-RA rotating anode X-ray diffraction was completed by the Testing Center of Qingdao Institute of Marine Geology. Qualitative identification of the clay minerals is carried out according to the orientation X-ray diffraction patterns after glycerin saturated.

The content of the semi-quantitative analysis of the clay minerals was carried out according to the diffraction patterns after glycerin saturated. The measured items included the clay mineral integral strength (distance of peak to the background line), percentage of the inverse of the weight factor multiplied by the peak high strength value to the weighted peak high strength value, corresponding to the percentage content of the minerals [14]. The percentage contents in the chlorite and kaolinite were calculated respectively, after the plus of the peak height values of chlorite (d_{004}), kaolinite (d_{002}) divided respectively by 1 and 1.75 and the respective percent contents of clay mineral were obtained [14].

2 Results and discussion

2.1 Types of clay minerals assemblage in surface sediments

The main types of clay minerals are illite, smectite, kaolinite and chlorite in the surface sediments off Yangtze River estuary. The types of clay mineral assemblage are divided into seven kinds according to the relative content of clay minerals, especially smectite. (1) the illite - smectite - kaolinite - chlorite-type (Type I); (2) the illite - kaolinite - chlorite - smectite-type (Type II) (3) the illite - chlorite - kaolinite -smectite- type (Type III); (4) the illite - kaolinite - smectite - chlorite-type (Type IV); (5) the illite - smectite - chlorite - kaolinite -type (Type V); (6) the illite - kaolinite - chlorite-type (Type VI); (7) the illite - chlorite - kaolinite-type (Type VII). The type I is the main type of clay mineral assemblage in surface sediments, and the following is type II, then type III, type IV and type V. Little proportions of type VI and type VII are in the surface sediments in the study area (Fig. 2).

2.2 The distribution of clay minerals

2.2.1 Illite

The illite has the highest concentrations of clay minerals in the sediment in this study area (content ranging from 47.0% to 76.7%, average of 60.3%).The illite content of the study area is from 55% to 65%, so illite content is divided into the low content region (<56%)

and high content region (>64%).

The high value distribution of the illite has two regions in the study area, namely in the south and southeast as well as in a small area outside of the Yangtze River estuary, and central south part has high value area of existence of the small piece of the illite. The low content region is mainly located in the northeast and north of the study area. Distribution of the illite content in the south and southeast of the study area decreased gradually to the north and northeast (Fig. 3), and the illite had the highest content in the southeast near the continental slope.

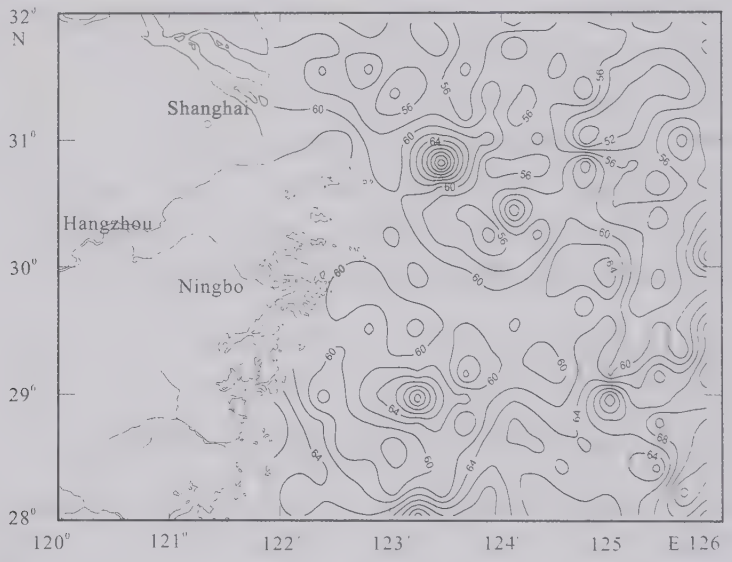

Fig. 3 Distribution of illite content in the surface sediments

2.2.2 Smectite

The smectite content in the sediments of the study area ranged from 0 to 34.8%, with an average of 14.9% and main distribution from 10% to 20%. The smectite content was divided into the low content region (<10%) and high content region (>16%). The high content region was mainly located in the north and northeast, and the low content region of the smectite is mainly in the south, southwest and southeast. Distribution of the smectite high content in the north and northeast regions was decreasing gradually to the south and southeast that was opposite to the illite (Fig. 4).

2.2.3 Kaolinite

The kaolinite content in the sediments of the study area ranged from 9.6% to 20.7%, with an average of 13.5% and main distribution from 10% to 16%. The kaolinite content

was divided into the low content region (<12%) and high content region (>16%) (Fig. 5). The high content region was mainly located in the northwest and west of the study area. And the low content region was mainly in the east, southwest and middle parts. Distribution of the kaolinite had higher content in the western offshore region, especially highest content in the estuary of Yangtze River and coastal area of the Zhejiang, decreasing gradually to the middle and eastern parts in the sea area.

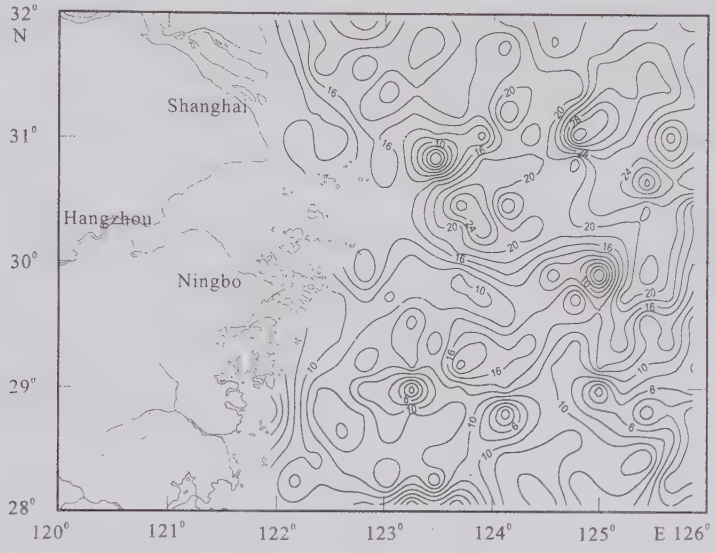

Fig. 4 Distribution of smectite content in the surface sediments

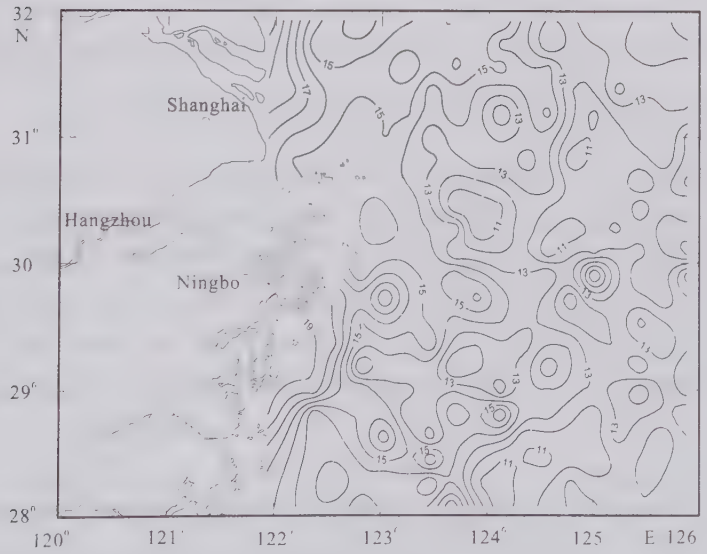

Fig. 5 Distribution of kaolinite content in the surface sediments

2.2.4 Chlorite

The chlorite content in the sediments of the study area ranged from 6.6% to 17.2%, with an average of 11.3% and mainly between 8% to 14%. The chlorite had the lowest content of the clay minerals in this study. The chlorite content is divided into the low content region (<10%) and high content region (>12%) (Fig. 6).The high content region is mainly located in the southeast and south of the study area, and the low content region is mainly located in the northeast and middle parts of the study area.

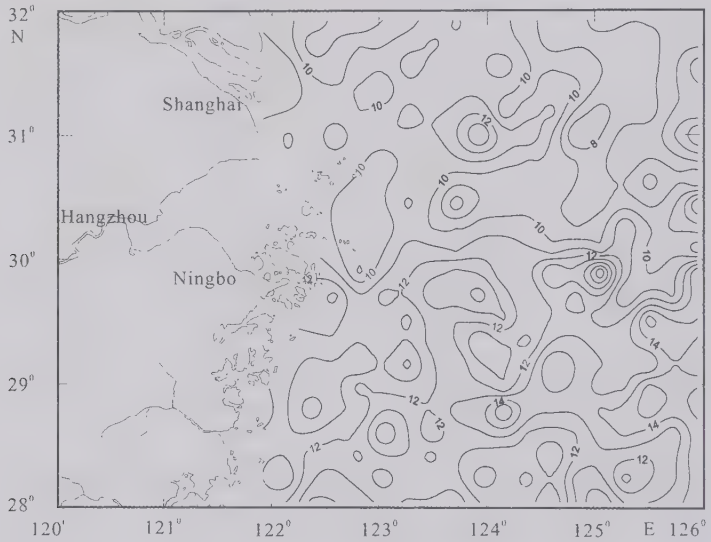

Fig. 6 Distribution of chlorite content in the surface sediments

2.3 Characteristics of the distribution areas for clay minerals

In order to research the distribution areas of the clay mineral assemblage in the study area, the Q-cluster analysis of the clay mineral samples was done by SPSS software. The number of the analysis samples was 187, and used clustering method was the Ward's method and used distance calculation method was the Square Eulidean distance method. The district off the Yangtze River estuary was divided into three mineral assemblage regions (Fig. 7) based on the Q-type analysis of the clay mineral samples in the study area.

2.3.1 Region A

The regional range of region A extends from the South Yellow Sea to the southeast that reaches nearly 29°30′, which located in the north and northeast parts of the study area. The characters of clay mineral assemblage are high smectite values, low illite and chlorite values. The clay mineral of specific feature has generally higher content of smectite,

between 19% - 23%, with the maximum value of 31% - 34% and an average of 21.6% (Tab. 1); the illite content is low, except for data limited stations more than 60%, and that between 50% - 60% with an average of 55.6%; the chlorite content is low too with the minimum value of 7.3%, the maximum value is 11.7% with an average of 9.8%; the kaolinite content is 13% in average.

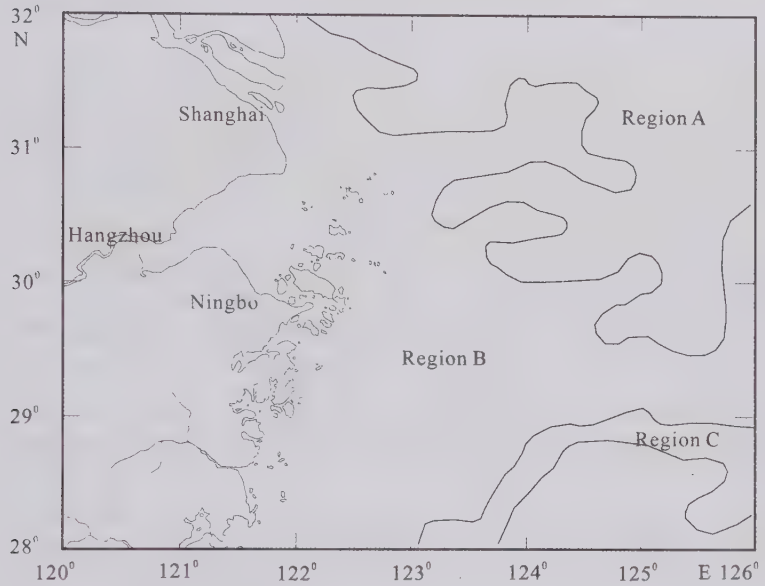

Fig. 7 Distribution areas of clay minerals

The clay mineral assemblage in average in region A is similar to that in Yellow River where the smectite, illite, chlorite and kaolinite contents in average are 23%, 59%, 9% and 8% [9]. It's closed to the results from ZHOU Xiao-jing, et al.,[13] who did cluster analysis in sample conducted in the Yangtze River estuary and the continental shelf of the East China Sea and attributed to the distribution areas of the Yellow River-like clay in the northeast and east parts.

2.3.2 Region B

The regional range of the region B includes southeast off the Yangtze River estuary and Zhejiang offshore sea, located in the west, middle and southeast parts of the study area. The characters of clay mineral assemblage are low smectite values, middle illite and chlorite values. The clay mineral of specific feature has generally higher content of illite that between 60% - 65% with an average of 62.5%; the smectite content is between 8% - 15% with an average of 11.6%(Tab. 1); the chlorite content is higher too, whose the average value is 12.1%; the kaolinite content is 13.8% in average.

The clay mineral assemblage of the region B in average is similar to that in the Yangtze River where the illite, smectite, chlorite and kaolinite content in average are 68%, 6%, 11% and 14% [9]. It's closed to the results from ZHOU Xiao-jing, et al.,[13] who did cluster analysis in sample conducted in the Yangtze River estuary and the continental shelf of the East China Sea and attributed to the distribution areas of the Yangtze River-like clay in the central west region of the continental shelf of the East China Sea.

2.3.3 Region C

The region C is only located in the southeast part of the study area. The characteristics of the clay mineral assemblage is that the smectite is not contained, and the illite and chlorite are highly contained. The illite content is ranging from 66% to 75%, and the chlorite content is ranging from 13% to 16%, the kaolinite content from 12% to 17%. And the average contents of them are 71.5%, 14.2% and 14.3% (Tab.1).

Tab. 1 Distribution areas of clay mineral assemblage from the Q-type cluster analysis

Distribution areas of mineral assemblage	sample number /individual	smectite / %	illite / %	kaolinite / %	chlorite / %
Region A	69	21.6	55.6	13.0	9.8
Region B	110	11.6	62.5	13.8	12.1
Region C	8	0	71.5	14.2	14.3

2.4 Provenance study of clay minerals

It's shown from many studies that clay minerals in the East China Sea are from the land source [7,8]. The characteristics of the clay minerals of sediments in the East China Sea are mainly dominated by the provenance into the sea and hydrodynamic role of sea area. The continental shelf sediments in the East China Sea are from the mainland of China, such as the Yellow River and Yangtze River carrying huge amount of sediments into the sea, which has diffusion and deposition by the currents carrying constantly to the outer shelf. The northern sediment of the East China Sea shelf are mainly affected by substances of the Yellow River and abandoned Yellow River and the southern sediments of the East China Sea shelf are mainly affected by substances of the present and ancient Yangtze River [9]. Some fine material into the sea by the Yangtze River moved to the east that entered into the Sea of Japan and the Pacific Ocean, some moved to the southwest that entered into the Taiwan Strait. And some fine material into the sea by the Yellow River moved to the east that entered into North Yellow Sea, with diffusion into East China Sea finally through South Yellow Sea [10]. The East China Sea shelf sediment can be divided into two types that is, "Yangtze River-like" and "Yellow River-like" sediments. The Yangtze

River-like sediments are mainly distributed in the central west region of the East China Sea and the Yellow River-like sediments are manly distributed in northeast, east parts and some region distributions in south of the study area. The Yellow River-like sediments in northeast part of study area may come from the fine particulate in the Yellow River and abandoned Yellow River, but the fine sediments in south and east parts may be the relict sediments formed in dry and cold climates such as Pleistocene Ice Age and then mixed with fine particulate of sediments in the modern river into the sea [13].

The clay minerals are generally formed by the weathering and its type depends on the parent rock types and climatic conditions. The illite is mainly produced by feldspar weathering. The feldspar are both important rock-forming minerals and common rock minerals, so it's not surprised that illite, as a terrigenous matter, dominated in the sediments of the study area. The kaolinite and chlorite are also the main mineral compositions of terrigenous fine particulate into the sea. Generally speaking, the main parent rock of the chlorite is metamorphic rock and chlorite is formed mainly in the high latitudes of the main physical weathering. The kaolinite is formed in the warm, humid environment of the lower latitudes. It's conductive to the formation and preservation of the smectite in the depositional environment of alkaline medium conditions [1].

The East China Sea is the marginal sea whose characteristics and distributions of clay minerals are impacted by the parent rock type and climatic environment of the land-source area, but also is controlled by the transport processing and the sedimentary hydrodynamic conditions in the depositional areas. Because the fine (<2 μm) clay mineral particles are very sensitive to hydrodynamic process, it's undoubtedly that the hydrodynamic role of the depositional region is the most important factor to influence the distribution of clay minerals. The precipitation of clay minerals mainly depends on the flocculation, so the crystal habit of the clay minerals and geochemical environment of the depositional region are also important factors affecting the distribution of clay minerals [15]. Considering the geographical location and current distribution of the East China Sea, The reasons cause the increase or decrease of smectite content possiblely should be: (1) the increase of the fine particulate in the Yellow River; (2) the four main clay mineral in the terrigenous sediments differed in the long-range transport processing because of process of the circulation system in the East China Sea; (3) the clay minerals are transformed into each other. Due to the influence of circulation distribution, the seawards substances of the Yellow River control on clay particle sediment of the continental shelf of the East China Sea, the sediments of in the Yellow River source might have a greater effect in the northern East China Sea, but more to south its influence weaker [13].

It's well known that terrestrial runoff carries sediment load to the river mouth area,

because the stream gradient decreases, changing water environment in river mouth area, the vast majority of sediments have flocculent subsidence in the estuarine delta. A small amount of unsettled sediments continues to the distant spread by the role of ocean currents. In addition，deposited sediments, which is under the powerful role of the wave and tide, causing the bottom sediment to tilting, suspension, and then be carried to the distant spread by the sea current and the bottom flow. Bingxian Guan did a detailed study on the scope of the role and the changes of winter/ summer in the East China Sea currents. Compared with the boundary of the clay mineral and the activity scope of the sea current in the East China Sea, the clay boundary has a good agreement with the activity scope of the northern Jiangsu coastal current, current circulation in the Yellow Sea, Zhejiang coastal current and Kuroshio. Therefore the sea current is considered to control the spreading range of the clay matter [9].

The study area is located in the west of East China Sea. The ^{14}C dating of the surface sediments showed that the depositional age was between 2 000 - 3 000 years and same era deposited basically. According to the types and association characteristics of clay minerals, the sediments in the study area were mainly from the Yangtze River, Qiantang River, Yellow River and offshore river systems, which provided a large number of terrigenous materials, and the re-role of sediments of the adjacent areas. There are many studies on the composition of clay minerals that was from the surrounding land into the sea, the clay minerals of Zhejiang coastal zone and clay minerals of offshore harbor in the study area [9,15,16]. The results showed that type of the clay mineral assemblages from the Yellow River could be divided into two types: illite-smectite-kaolinite-chlorite (Type I) [9] and illite -smectite-chlorite-kaolinite (Type V) [16]; the type clay mineral assemblages from Yangtze River could be divided into two types too: illite-kaolinite-chlorite-smectite (Type II) [9] and illite-chlorite-kaolinite-smectite (Type III) [16]; the types of clay mineral assemblages from Zhejiang coastal zone and offshore harbor were illite-chlorite-kaolinite-smectite (Type III). It's obviously that clay mineral assemblages of the Type I and Type V are the Yellow River source, and the clay mineral assemblages of Type II and Type III are the Yangtze River and offshore harbor sources. Comprehensive analysis showed that region A was the Yellow River source, mainly from Yellow River and region B was the Yangtze River source, mainly from Yangtze River.

In general, the hydrodynamic role of the offshore area is strong, and salinity is low and flocculation is weak, so it's much easier for the granular or thick plate kaolinite minerals to settle down and to form the high value area of kaolinite distribution (Fig. 5). Relatively speaking, the hydrodynamic role of farther offshore area is weaker, and salinity is higher and flocculation is stronger, so it's gradually for the fragmented or scaly illite and

smectite to settle down and to form the high value area of them (Fig. 3 and Fig. 4) [17, 18]. After terrigenous sediments into the sea, they are going to be transported for a long-distance, mixed and transformed after deposition. Therefore, the clay mineral assemblages in the sediments of region C in the study area should be produced by several factors.

3 Conclusions

a) The widespread clay minerals in the surface sediments off Yangtze River estuary are illite, kaolinite, chlorite and smectite. The illite, as the dominant minerals, has the average content of 60.3%; followed by smectite whose average content is 14.9%; the average content of kaolinite is 13.5% and chlorite's is 12.3%.

b) The dominant assemblage type of clay minerals is illite-smectite-kaolinite-chlorite, followed by type of illite-kaolinite-chlorite-smectite. The clay mineral source of surface sediments off Yangtze River estuary is the terrigenous origin that is supplied by the Yellow River and Yangtze River.

c) The Q-type cluster analysis showed that sediments from both recent and ancient Yellow River were deposited mainly in the northeast part of the study area to the north of 29°30′. The substance from the Yangtze River was deposited mainly in the western and middle parts off the Yangtze River estuary.

Reference

[1] LAN Xian-hong. Clay minerals as an index of paleoclimate [J]. Geological Science and Technology Information, 1990, 9(4): 31 - 35.

[2] Park Y A, Khim B K. Clay minerals of the recent fine grained sediments on the Korean continental shelves [J]. Continental Shelf Research, 1990, 10: 1 179 - 1 191.

[3] LAN Xian-hong. The palaeoenvironmental significance of the clay minerals assemblage in marine sediments [J]. Marine Geology Letters, 2001, 17(1): 5 - 10.

[4] Xu K H, Milliman J D, Li A C, et al. Yangtze-and Taiwan-derived sediments on the inner shelf of East China Sea [J]. Continental Shelf Research, 2009, 29: 2 240 - 2 256.

[5] FANG Xi-sheng, SHI Xue-fa, WANG Guo-qing. Distributions of clay minerals in surface sediments from the Changjiang River subaqueous Delta and their affecting factors [J]. Advances in Marine Science, 2007, 25(4): 419 - 427.

[6] LAN Xian-hong, ZHANG Xian-jun, LIU Xin-bo, et al. Distribution pattern of clay minerals in surface sediments of South Yellow Sea and their provenance [J]. Mar. Geol. & Quat. Geol., 2011, 31(3): 11 - 16.

[7] QIN Yun-shan, ZHAO Yi-yang, CHEN Li-rong, et al. Geology in the East China Sea [M]. Beijing: Science Press, 1987,1 - 550.

[8] JIN Xiang-long. Marine Geology in the East China Sea [M]. Beijing: China Ocean Press, 1992, 1 - 524.

[9] ZHU Feng-guan, LI Xiu-zhu, GAO Shui-tu. Study of clay minerals in surface sediments of the East China Sea Shelf area [J]. Donghai Marine Science, 1988, 6(1): 40 - 51.

[10] HE Liang-biao. Clay Minerals in China Sea and adjacent sea area [J]. Science in China (Series B), 1989, 1: 75 - 83.

[11] LI Guo-gang. Composition and distribution of clay minerals in surface sediments off China Sea and its geological significance [J]. Oceanologia Sinica, 1990, 12(4): 470 - 479.

[12] ZHU Feng-guan. Clay minerals of the East China Sea Shelf area in the recent Epoch stratum [J]. Donghai marine Science, 1985, 3(4): 32 - 43.

[13] ZHOU Xiao-Jing, LI An-Chun, WAN Shi-Ming, et al. Clay minerals in surficial sediments of the East China Sea Shelf: Distribution and provenance [J]. Oceanologia et Limnologia Sinica, 2010, 41(5): 667 - 675.

[14] GB/T 12763-2007. Specifications for oceanographic survey-Part 8: Marine geology and geophysics survey [S]. Beijing: China Standard Press, 2007, 10 - 12.

[15] YANG Zuo-sheng. Mineralogical assemblages and chemical characteristic of clay from sediments of the Yellow, Yangtze and Pearl Rivers and their relationship to the climate environment in their sediment source areas [J]. Oceanologia et Limnologia Sinica, 1988, 19(4): 336 - 346.

[16] FAN De-jiang, YANG Zuo-sheng, MAO Deng, et al. Clay minerals and geochemistry of the sediments from the Yangtze and Yellow Rivers [J]. Mar. Geol. & Quat. Geol., 2001, 21(4): 7 - 12.

[17] LAN Xian-hong, MA Dao-xiu, XU Ming-guang, et al. Clay minerals in the Late Quaternary of the sediments of the Zhujiang Estuary and their facies significance [J]. Journal of Oceanography in Taiwan Strait, 1988, 7(2): 127 - 134.

[18] Xin Chun-ying, He Liang-biao, Wang Hui-yan. Clay minerals in the surficial sediments from the Yellow River Estuary and Its offshore areas [J]. Journal of Oceanography of Huanghai & Bohai Seas, 1998, 16(4): 23 - 27.

长江口外表层沉积物黏土矿物分布特征

蓝先洪[1,2]，张志珣[1,2]，李日辉[1,2]，王中波[1,2]，陈晓辉[1,2]，田振兴[1,2]

（1. 国土资源部海洋油气资源与环境地质重点实验室，青岛 266071；2. 青岛海洋地质研究所，青岛 266071）

摘 要：依据对长江口外表层沉积物187个站位沉积物样品的黏土矿物含量分析，研究了长江口外表层沉积物黏土矿物的组合特征和分布规律。长江口外表层沉积物伊利石为优势矿物，平均含量为60.3%；次之为蒙脱石，平均为14.9%；高龄石平均含量13.5%，绿泥石平均含量为12.3%。黏土矿物的组合类型以伊利石-蒙脱石-高岭石-绿泥石型为主，伊利石 高岭石-绿泥石-蒙脱石型次之；长江口外表层沉积物黏土矿物主要为陆源成因，物质主要来源于黄河和长江的供给。Q型聚类分析显示，现代黄河物质及老黄河物质主要沉积于研究区东北部北纬29°30′以北地区，长江物质主要在研究区西部及中部区域沉积。

关键词：黏土矿物；分布特征；长江口外

Changes in magnetic susceptibility and grain size of Holocene sediments of the Pearl River estuary and climate changes reflected by them

CAO Ling-long[1, 2], WANG Ping[1*], WANG Jian-hua[2], WANG Xiao-jing[3], YANG Jie[4]

1. *South China Sea Marine Engineering and Environment Institute, SOA, Guangzhou* 510300, *Guangdong province, China;*

2. *Department of Earth Sciences, Sun Yat—sen University, Guangzhou* 510275, *Guangdong province, China;*

3. *XI'AN University of Science and Technology, Xi'an* 710056, *Shanxi province, China;*

4. *South China Sea Environment Monitoring Center, SOA, Guangzhou* 510300, *Guangdong province, China*

Abstract: Through the Pearl River Estuary Wan Qing-sha W2 core AMS ^{14}C dating of sediments, combining with paleomagnetic test, pollen analysis, and comprehensive comparison with other relevant records, the regional framework of Holocene age was established. Using the combined feature grain size and magnetic susceptibility proxies for the environment, climate change information in the area since about 6 000 cal yr BP was obtained. The result showed the area since the middle Holocene had experienced three stages climate changes of warm and dry - cool and wet temperature and humidity. South area of China in the late Holocene climate (especially rainfall) had important changes, corresponding to the Northern Hemisphere solar radiation reducing, air temperature decreasing, Asian monsoon weakening, and it had close ties with activities to strengthen El Nino - Southern Oscillation events.

Keywords: grain size; magnetic susceptibility; holocene; paleoclimate; Pearl River estuary

The granularity of the sediment is an important physical indicator of sediment environment. As shown in the research of the loess formed by the accretion of wind and dust, the grain size of the loess is a good indicator of the changes of the East Asian monsoon, and it can be correlated to the curve of the deep-sea oxygen isotope($\delta^{18}O$).Meanwhile, magnetic susceptibility is one of the indices which show the magnetic features of the sediments. The information of the environment changes can be

Received on May 16, 2012

*Corresponding author: 1903125@qq.com

displayed through analyzing the curve of the magnetic susceptibility. The researches of the deep-sea sediment show that the magnetic susceptibility and the granularity of the sediments can be used to measure the speed and the transporting capacity of the ocean current. Also, the researches of the sedimentology show the magnetic susceptibility and the granularity of the sediments indicate the climate changes of drying and wetting. In 1980s, Huang Zhen-guo et al. studied on the formation and evolution of the Pearl River estuary, followed by Lan Xian-hong, Zhang Weiqiang, Zheng Zhuo, Liu Chun-lian, who have further researched on the climate changes of the Pearl River estuary. However, few people have focused on the climate change there after Holocene and less researches were on the magnetic susceptibility and the granularity of the sediments and its relations with the climate changes, since most of their researches are on the spore and pollen, clay mineral and foraminifer. This thesis focuses on the evolution of the climate environment of the Pearl River estuary after Holocene through analyzing the magnetic susceptibility, the granularity of the sediments and other substitute indices such as the spore pollen.

1 The natural environment of the Pearl River estuary

The Pearl River estuary lies in the south of China with the surface area of 10 000 km^2. It is a plain area, where the Pearl River water system joins the South China Sea. Since later Pleistocene epoch, it had sediments composed of clay, clay with aleuvitic texture, aleuvite. The thickness of the sediments ranges from several meters to scores of meters because of the changes of basement topography and the rate of deposition is from 50 cm to 250 cm every millennium. The drill core W2 under study is located in a town, named Wan Qing-sha Town, which lies in the south of Guang Zhou city surrounded by sea at the three sides (Fig. 1) .

2 The collection of the samples and the research methodology

The number of the samples under research was 141. They were collected with the inter-space of 10 cm. The instrument to analyze the grain size was Automatic Laser Granularity Analyzer Mastersize 2000 produced by the British company, Malvern, whose measurement range of the grain size was from 0.02 to 2 000 μm, and the instrumental error of the repeated measurement was less than 2%.

Steps were as follows:

a) Add distilled water and 10% hydrogen peroxide to get rid of the organic fertilizer.

b) Add 10% hydrochloric acid to get rid of inorganic carbon.

c) Add distilled water, without moving the sample for 24 hours.

d) Add the dispersant, at the same time, use the ultrasonic wave to oscillate the sample for 15 min .

e) Highly dispersed particle suspension was formed.

Criterion was the Yudo-Wash side-grading criterion.

Index:

The indices of the grain size acquired through the graphical method by Folk and Ward, included mean diameter, sorting coefficient, skewness, kurtosis, mode, et al. Mean diameter showed the central tendency of the grain size distribution of the sediments, reflecting the mean power capacity of the transporting and sediment medium; Sorting coefficient was marked by the standard deviation, reflecting the uniformity of the sediment particle and the higher the index, the worse the separation; Skewness and kurtosis reflected the grain size proportion, the concentration degree of the diameter distribution, and the power of the sediment; Mode showed the content figure of the grain which is highly distributed, and reflected the separation of the sediment, and the changes of skewness and the kurtosis.

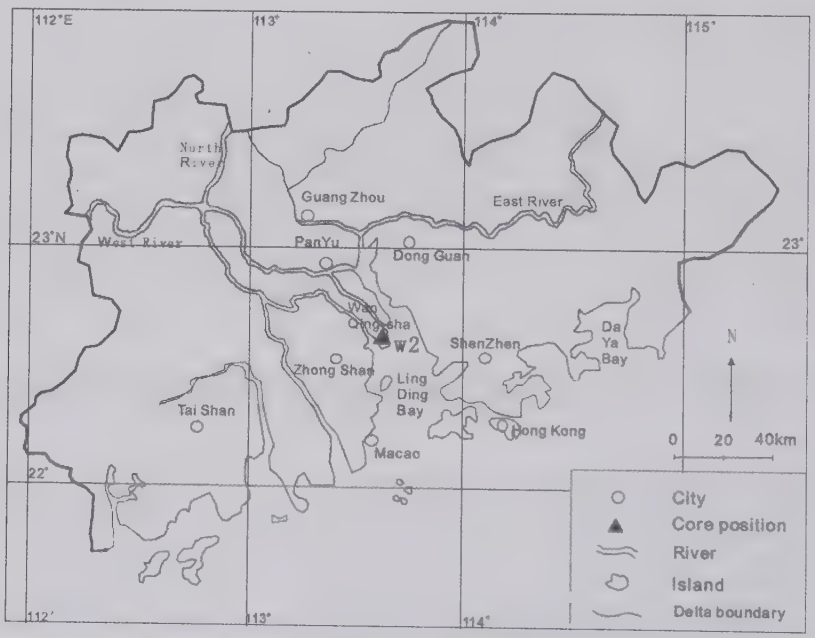

Fig. 1 General situation of Wan Qing-sha and position of core W2

The instrument to analyze the magnetic susceptibility was the high-low frequency susceptibility admeasuring apparatus MS2 produced by the British company Bartington. 836 samples were tested by repeated measurements on the freshly-cut profile with the

inter-space of 2 cm. In order to make sure the accuracy of the result, the mean value was acquired by five times' measurement.

The samples of four seashells and carbon flakes were collected in the section of the sediment with significant changes of characters and appearances to identify the age through AMS ^{14}C. The pre-treatment of the samples had been carried on in Guangzhou Institute of Geochemistry, Chinese Academy of Science, and the measurement in the heavy ion physical lab of Peking University with AMS. The indices related to the age of the samples were revised by the software Calib5.0 (Tab. 1).

The measurement of the paleomagnetism was carried on with Superconducting Rock Magnetometer in the Institute of Geology and Geophysics of Chinese Academy of Sciences. The samples were collected by drilling (0 m to 15.37 m) with U-shape groove, the inter-space being 2 cm, an alternative current demagnetizer with several graces. The magnetic remanence was acquired through principle components analysis and the magnetic dip through Fisher's statistical method. The figure was reliable because the value of MAD was between 0 and 3 with little error.

3 Result and discussion

3.1 Identification sediment age

The lithological characters show that there is an obvious change in 15.37 m. The indices of the spore pollen indicate that the number of *gramineae* and *pteridophytes* increases dramatically from 15.37 m, and *Sonneratia* mangrove disappears, and *Dacrydium pierrei* deceases sharply. Those are consistent with the description of the researches of Sun Shao-xian, Li Ping-ri and Zheng Zhuo. The analysis of paleomagnetism shows that most of the samples have the forward magnetic dip showing they are all Brunhes normal polarity period of depositions. At the same time, the magnetic dip has repeatedly negative value from 16.65 to 15.60 m. Compared with Standard geomagnetic polarity time scale and ^{14}C dating result, we confer that it is consistent with the Gothenburg polarity drift between 11 000 and 12 000 yrs BP. Other researchers have also found the record of this event in the lacustrine strata and loess of eastern coastal area in China. With all the founding above, the place 15.37 m is the dividing line between Holocene and Pleistocene.

The data of age is reliable with the analysis of all the results. According to the interpolation and extrapolation, the data we have acquired form the frame of this research. Suppose the rate of sedimentation between the adjacent control points is mean, and the

age of the bottom section be 6010 cal yr BP, and the mean rate of sedimentation be 246 cm/kyr. At the beginning of the Holocene, there is a deletion of deposition. With the character of the sediment, the age of the deletion is about 10 to 6 kyr BP.

3.2 Variations of sediment granularity composition and magnetic susceptibility

As shown from the research on the sediment granularity, the scope of the grain size is between 0 and 1 800 um. The size of the sand (>63 um) mainly is between 440 and 660 cm, and the scope of which is relatively large from 3.85% to 88.32%, average 24.55%; that of the silt(4 - 63 um), accounts for 5.15% to 58.82%, with average of 36.77%; that of the clay, accounts for 5.95% to 66.74%, with depth between 1 050 m and 1 537 cm. The sorting coefficient ranges from 0.38 to 3.21, and the mean value 1.87. The samples which have lower value have absolute advantage. The skewness value ranges from -0.33 to 0.64 with the large scope of 5 kurtosis grades from negative skewness to positive skewness. Most of the samples get close to symmetrical and positive skewness, and the mean value is 0.22. The kurtosis value is 0.81 to 2.55 with four grades, and most of which are medium sharpness and sharpness, and the mean value is 1.16. The result of the particle size analysis is shown in Fig. 2.

Tab. 1 Age data of core W2 in Wan Qingsha, Pearl River Delta

Samper numbe	Depth/ cm	*Properties	Test age / yr BP	adjusted age / yr BP
W2-C1	240	shell	1175 ± 33	1110 ± 60
W2-C2	670 - 690	shell	1817 ± 29	1770 ± 40
W2-C3	1 053	shell	2452 ± 40	2540 ± 120
W2-C4	1 280	charcoal	3698 ± 28	4040 ± 100

The frequency distribution curve shows not only the grain size, but also the content of the size fraction component, and other indices of the samples. So it is often used to display the particle distribution. The frequency changes are correlated with the properties of rock and the sedimentary surroundings with regular patterns. The samples of depth from 1 357 to 1 050 cm have main singlet, and mode change less from 10 um to 14 um. As we can see, the figures of a few samples show there is a small secondary crest of sand-sized particle on the main crest of the silt-sized particle, and the bottom between two main crests is not clear. The samples of depths from 1 050 to 670 cm, with double peaks, clear secondary peak, and mode 9 um to 97 um, mainly 9 um to 13 um, have a tendency of moving to the coarse grain. The samples depth from 670 to 440 cm, with singlet and less double peaks,

have not so clear secondary peak, mode 121 to 201 um. The samples depth from 440 to 107 cm, with mainly bimodal pattern, clear secondary crest, many multimodal patterns, few singlet, and mode 7 to 110 um, have largest change scope (Fig. 2) .

The magnetic susceptibility mainly reflects the concentration rate of the magnetic mineral and the behavior character, and an indicator of the degree of the magnetization and variation of the sedimental surroundings through displaying the component changes. It has been widely used in the researches of the quaternary period environmental changes, since the changes of content are related to the source, environment, climate change and the power at that period. According to the test result of Holocene magnetic susceptibility in W2 core, the value fluctuates clearly between 11.0 - 52.9×$10^{-8}$$m^3$/kg, and the mean value is 19.7×$10^{-8}$$m^3$/kg. The scope of fluctuation is relatively large from 120 to 210 cm at the top (Fig. 2). According to the magnetic susceptibility curve, there are a few fluctuations between 1 537 and 1 050 cm, the mean value of which is 16×$10^{-8}$$m^3$/kg. At the point of 943 cm, there is a peak. The mean value between 1 050 and 440 cm is 24×$10^{-8}$$m^3$/kg. The value begins to increase from 440 cm, and sharply increase at the point of 210 cm.

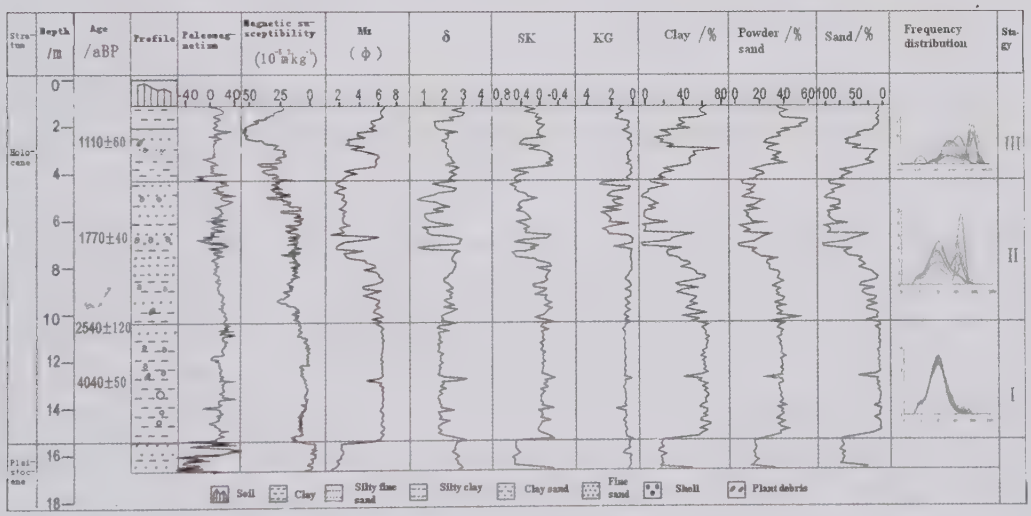

Fig. 2 Composite diagram of granularity, magnetic susceptibility for the Core W2

3.3 Particle size, magnetic susceptibility and environment changes

The figures of the sediment granularity have shown specific characters with the effects of the various elements in estuarial area. Since Holocene, the sources of the sediments in the Pearl River area have not chang much, the main of which being terrigenous clastic rocks. The grain size is mainly affected by the surroundings. Firstly, the changes of the particle diameter distribution are related to the distance to the estuary and the sea level with the effect of the running water. When the sea level lows, the estuary is

closer to the core, and the coarse particle fragments are easily to be moved here. Also, the grain size is closely related to the change of climate. When the rainfall increases, the hydrodynamic power increases, and the more particles have been moved in the river. According to the sea level change curve of Pearl River Estuary since 8000yr BP finished by Fang Guo-xiang, the change frequency and scope are relatively small (±5 m). Therefore, climate change, especially the rainfall, is the main element affecting the change of the grain size other than the change of sea level since 6 000 yr BP.

The magnetic susceptibility depends on the abundance of the magnetic mineral particle which is related closely to the climate. Within the estuary area, the environment for the sources is relatively stable. When the rainfall increases, the erosion and weathering increases, and more fragments moved in, moreover the concentrate of the minerals increases, and the value of the magnetic susceptibility increases too. When it is dry, the hydrodynamic power decreases, and less fragments form outside are brought in, moreover the concentration decreases and the value decreases too. With the characters shown by the granularity composition and spore pollen, the research indicates that the high magnetic susceptibility represents the high hydrodynamic power in Holocene, and the climate wet then; the low of which means dry climate.

We have divided the Holocene sediment in Wan Qing-sha W2 core into 3 sections according to magnetic susceptibility, combination of fineness, spore pollen and lithological characters.

Section I (1 537 cm to 1 050 cm, about cal 6 000 to 2 500yr BP): The particles are composed mainly by dark grey or pure clay, with thin fine and silty sand at the top. The mean diameter is 6.7Φ, much larger than that of cutting section. It is the finest section. The scope of the skewness is from -0.25 to 0.14, mainly concentrate between -0.1 to 0.08, and it belongs to approach symmetric form. The value of the kurtosis is between 0.9 and 1.6, mainly concentrate between 1.2 and 1.3. The curves are mainly singlet with little change in mode. Little change is in sorting coefficient. The character of the transporting power is few and sedimental power is stable. Meanwhile the magnetic susceptibility is lower than the mean value and stable, which shows the rather dry weather then. Also according to the figures of the spore pollen, during that period, woody plant is flourish, especially subtropical evergreen forest. There are mangroves such as Bamboo trees, sedges and grasses in Cyrtandroideae. However, the content decreases from the bottom to the top, which shows that the climate has changed from warm to cool and wet during Holocene.

Section II (1 050 to 440 cm, about cal 2 500 to 1 400yr BP): The bottom of this section is composed mainly by dark grey medium and fine sand with thin clay, partly by silty

fine sand. The top of this section is mainly composed by loose fine sand and thin silt. The changes of particles indices are dramatic. The composition of the coarse particle increases to the biggest number, and the sorting coefficient and skewness value fluctuate sharply. There are mostly bimodal state with clear secondary peak. From bottom to top, the mode and the main peak of the curve have a tendency of moving to the end of the coarse particle. The speed of deposition increases, which shows that the hydrodynamic power is increasing and the character of external agent which carries the mineral to new places changes largely with unstable deposition power. All shows that the sediment during this period is formed by different deposition with changeable environment, closely related to climate. We can see that the magnetic susceptibility reaches its peak at the point of 8.9m with an increase tendency. It shows that the climate is rather wet. Also, the figures of the spore pollen indicate that it is cool then with low content of trilete spore of *Cyperaceae*, *Artemisia* and *Myriophyllum* aquatic fern which usually grow in warm environment.

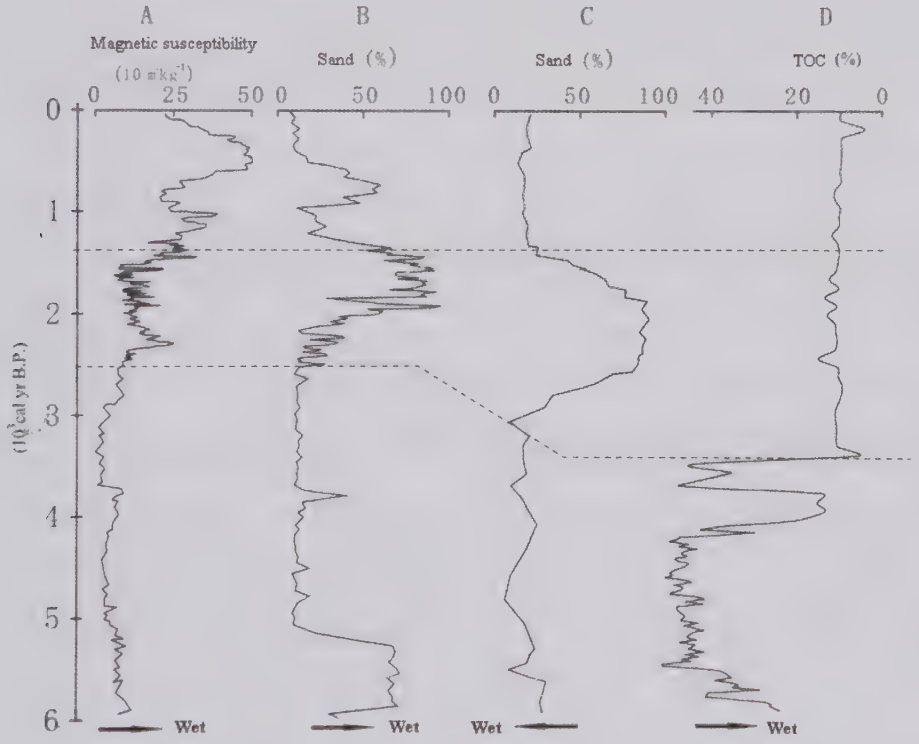

Fig.3 Comparison of W2 hole size, magnetic susceptibility index at Pearl River estuary since contrast with the other records

A. W2 magnetic susceptibility; B. W2 Sediment sand percentage; C. Shaanxi Jingbian loess deposits of sand percentage; D. Total organic carbon (TOC) content percent at Great Lakes

Section III (from 440 cm to 120 cm, about 1 400 cal yr BP to today): The sediment is

mainly composed of the taupe silty clay with muddy fine sand in the middle. There is a stratification which is formed in the movement of tide. The granularity decreases at the point of 440 cm, then increases rapidly and decreases again, which shows that the climate changes from warm to cool and warm again. The frequency curve of this section displays there are most bimodal patterns with clear secondary peak, some multimodal patterns and few singlet. The mode is 7 um to 110 um with largest change scope. The speeding rate of deposition is the largest one, which shows that the sedimental surroundings are complex and the external force leading to carrying is relatively strong. This may be related to the increasing pushing-forward speed of the Pearl River Estuary. The magnetic susceptibility increases with large fluctuation. The figures of the spore pollen show that the herbs, such as *Cyperaceae*, *Cyrtandroideae*, *Chenopodium*, *Artemisia aquatic Myriophyllum*, and the ferns, such as three joints fern spores, *Cyathea*, *Mount Kei* have increased, compared with section II, showing the warm and humid environment. At the point of 2 m, the number of the magnetic susceptibility reaches its peak, and *gramineae* increases sharply. All those are related to the human activities. At the end of this period, the magnetic susceptibility and the mean diameter decrease obviously, indicating the relative dry climate at that time.

3.4 Discussion

So far, the early and the middle period of the Holocene have been regarded as the most comfortable one with warm and humid climate. However, the figures of the granularity composition, the magnetic susceptibility, spore pollen and AMS^{14}C date identification of the W2 core show that in the Pearl River Estuary, during the Holocene, the climate was warm generally, but relatively dry. That is different from the humid environment record of stalagmite in Dong Ge in Gui Zhou and stalagmite $\delta^{18}O$ in Shen Long-jia in HuBei; while it is consistent with the record of the tropical and sub-tropical area in Africa and Asia, which shows that the climate was becoming wet in mid-Holocene. Meanwhile, the record of the organic carbon of the mire in the lake of Nan Lin nearby shows that the climate turned to be cool and humid in 3 800 cal yr BP (Fig. 3). Though there is some difference in the year identification, it is certain that in the south of China, the climate is warm and dry in the mid-Holocene, and it turned to be cool and humid in the late Holocene. It has been shown that since the late-Holocene, the radiation of the sun reduces, the temperature down, and the Asian monsoon reduce, causing the rainfall in the south increases and reaching its peak since Holocene in the south of China. Besides, a lot of researches show, during the late-Holocene, the power and the frequency of the El Nino phenomenon increased. The record of Maer Lake and Hu Guang Maar Lake in HaiNan shows that the climate pattern in 2 700 cal yr BP was related to ENSO, which means that the climate change in the southeast is closely related to the El Nino and ENSO since Holocene.

4 Conclusions

The conclusions is followed:

(1) As the substitute indicators, the granularity composition and the magnetic susceptibility are correlated. The magnetic susceptibility is positively related to the sand component percentage, and negatively related to the clay percentage. Besides, according to the spore pollen and the former researches, the relatively high magnetic susceptibility and sand represent the higher hydrodynamic force and more humid environment.

(2) The climate changes in the Pearl River Estuary since the Holocene are divided into 3 period, whose process is warmth and dryness-coolness and humidity-warmth and humidity.

(3) The change of the volume of the rainfall in the south of China is not consistent with the change of the Asian monsoon. When the Asian monsoon is strong in the mid-Holocene, the climate of the area is relatively dry; while, when the sun radiation reduces, the temperature decreases and the monsoon weakens, and the rainfall increases and the climate turn humid. Those are consistent with the finding of An Zhi-sheng, and the weakening of the Asian monsoon is consistent with the moving of the rainfall area to the south. Also, it is closely connected with the El Nino phenomenon since the late-Holocene.

References

[1] Sun Y C, Li H S. Sedimentary facies and environment of clastic rocks [M]. Beijing: Geologic Press, 1986, 65-81.

[2] Xiao J L, Nakamura T, Lu H Y, et al. Holocene climate changes over the desert/loess transition of north-central China [J]. Earth and Planet Sci. Lett., 2002, 197: 11 - 18.

[3] Yang W G, Zheng H B, Wang K, et al. Sedimentary characteristic of terrigenous clast of site MD05-2905 in the northeastern part of south china sea after 36ka and evolution of east asian monsoon [J]. Advance in earth science, 2007, 10(22):1 012 - 1 018.

[4] Verosub K L, Roberts A P. Environmental magnetism: past, present, and future [J]. J. Geophys. Res., 1995, 100: 2 175 - 2 192.

[5] Liu Q S, Deng C L, Torrent J, et al. Reviews on resent developments of mineral magnetism of the Chinese loess [J]. Quat. Sci. Rev., 2007, 26: 368 - 385.

[6] Giancarlo G B, Nicholas M I. Holocene periodicity in North Atlantic climate and deep-ocean flow south of Iceland [J]. Nature, 1999, 397:515 - 517.

[7] Campbell C. Late Holocene lake sedimentology and climate change in southern Alberta, Canada

[J]. J. Quat. Res.,1998, 49: 96 - 101.

[8] Wang X Y, WU L, Zhang G S, et al. Characteristics and Environmental Significance of Magnetic Susceptibility and Grain Size of Lake Sediments since Holocene in Chaohu Lake, Anhui Province [J]. Scientia Geographica Sinica, 2008, 28(4): 548 - 552.

[9] Huang Z G, Li P R, Zhang Z Y, et al. Pearl River delta formation development and evolution [M]. GuangZhou: Popular Science Press, Guangzhou branch, 1982.

[10] Lan X H. Sedimentary characteristics and strata division of core 22 of the Ppearl River delta [J]. Oceanologia Et Limnologia Sinica, 1991, 22(2): 148 - 164.

[11] Zheng Z, Wang J H. Paleoenviromental significance of late Quaternary pollen flora in northern Zhuijiang River delta [J]. Tropic Oceanology, 1998, 17(3): 1 - 9.

[12] Zhang W Q, Huang Z G. A new approach to the climatic fluctuation during late Quaternary in the Pearl River delta [J]. Tropical Geography, 2005, 25(4): 298 - 301.

[13] Liu C L, Franz T F, Dong Y X. High resolution ostracod records of borehole PRD05 and the Late Quaternary palaeoenvironment in Pearl River Delta [J]. Journal of Palaeogeography, 2008, 10 (3): 313 - 322.

[14] Yang X Q, Rodney G, Zhou H Y. Sediment rock magnetic properties and its environmental significance in Pearl River Delta [J]. Science in China (Series D), 2007, 37(11): 1 493 - 1 503.

[15] Long Y Z, Huo C L. The sedimentation characteristics of Zhujiang river delta in late quaternary [J]. Marine Sciences, 1990, 4: 7 - 14.

[16] Chengdu Institute of geology. Sedimentary rock grain size analysis and its application [M]. Beijing: Geological Publishing Press, 1978: 31 - 143.

[17] Xie Y Y, Li C A, Wang Q L. Grain-size Characteristics and Their Environmental Significance of Jiangling Lake Sediments in Jianghan Plain [J]. Journal of Jilin University (Earth Science Edition), 2007, 37(3): 570 - 577.

[18] Sun S X. Distribution of sonneratia pollen in the late quaternary strata of the south china sea and its significance [J]. Journal of Tropical Oceanography, 1991, 10(1): 21 - 25.

[19] Li P R, Fang G X, Huang G Q. Holocene environmental changes in Zhujiang delta [J]. Quaternary Sciences, 1991, (2): 130 - 138.

[20] Zheng Z. Distribution of dacrydium in south china during the late quaternary [J]. 1991, 33(2): 130 - 139.

[21] Harland W B. A geologic time scale [M]. In: Cambridge Earth Science Series. Cambridge: Cambridge University Press, 1982, 28 - 35.

[22] Zhu R X, Zhao X T, Wei X F. the earth's magnetic field polarity shift a evidence in 12 000 years ago [J]. Chinese Science Bulletin, 1992, (17): 1 596 - 1 598.

[23] Moner N A. Geomagnetic excursion during last 140 000 yrs [J]. Quaternary Research, 1981, (11): 48 - 51.

[24] Shu W J, Wang W M, Chen Y, et al. Sedimentary characteristics of the palaeochannel and

environment evolution during the Holocene in the Taihu [J]. Journal of Stratigraphy, 2008, 32(2): 146 - 151.

[25 Wang J Y, Wang J, Liu J L, et al. Evolution of sedimentary environment of a Holocene river channel in east Taihu lake [J]. Acta Pala -eontologica Sinica, 1996, 35(2): 224 - 231.

[26] Fang G X, Li P R, Huang G Q. Sea level changes in Pearl river delta during the past 8 000 years [J]. Geographical Research, 1991, 10(4): 1 - 11.

[27] Dykoski C A, Edwards R L, Cheng H, et al. A high-resolution, absolute-dated Holocene and deglacial Asian monsoon record from Dongge Cave [J]. Earth Planet Sci. Lett., 2005, 233(1-2): 71 - 86.

[28] Shao X H, Wang Y J, Cheng H. Holocene monsoon climate evolution and drought events in Hubei recorded in a stalagmite from Shen nong-jia [J]. Cinese Science Bulletin, 2006, 51 (1): 80 - 86.

[29] Guo Z T, Petit-Maire N, Kropelin S. Holocene non-orbital climatic events in present-day arid areas of northern Africa and China [J]. Globplanet Change, 2000, 26: 97 - 103.

[30] Gasse F, Van Campo E. A brupt post-glacial climate events in West Asia and North Africa monsoon domains [J]. Earth Planet Sci. Lett., 1994, 126: 435 - 456.

[31] Zhou W J, Yu X F, Jull A J T, et al. High-resolution evidence from southern China of an early Holocene optimum and a mid-Holocene dry event during the past 18 000 years [J]. Quat. Res., 2004, 62 (1): 39 - 48.

[32] YAO T D, Thompson L G. Dhond ice core records from past 5ka temperature change [J]. Science in China(Series B), 1992, 10: 1 089 - 1 093.

[33] Xiao J L, Nakamura T, Lu H Y, et al. Holocene climate changes over the desert/loess transition of north-central China [J]. Earth Planet Sci. Lett., 2002, 197: 11 - 18.

[34] An Z S, Stephen C, Porter, et al. Asynchronous Holocene optimum of the East Asian monsoon [J]. Quaternary Science Reviews, 2000, 19: 743 - 762.

[35] Moy C M, Seltzer G O, Rodbell D T, et al. Variability of ElNiño/Southern Oscillation activity at millennial timescales during the Holocene epoch [J]. Nature, 2002, 420: 162 - 165.

[36] Zhen Z, Wang J H, Wang B, et al. Maer Lake Holocene environmental record in Hainan Island [J]. Chinese Science Bulletin, 2003, 48(3): 282 - 286.

[37] Wang S Y, Lv H Y, Liu J Q. High resolution sporopollen records revealing the early Holocene Optimum environmental characteristics in Maar lake [J]. Chinese Science Bulletin, 2007, 52(11): 1 285 - 1 291。

珠江口全新世沉积物粒度与磁化率的变化特征及其所反映的气候环境变化

曹玲珑[1,2]，王 平[1*]，王建华[2]，王晓静[3]，阳 杰[4]

（1. 国家海洋局 南海海洋工程勘察与环境研究院，广东 广州 510300；2. 中山大学地球科学系，广东 广州 510275；3. 西安科技大学地环学院，陕西 西安 710056；4. 国家海洋局 南海环境监测中心，广东 广州 510300）

摘 要：通过对来自珠江口万顷沙W2孔的沉积物进行AMS ^{14}C测年，结合古地磁测试以及孢粉分析结果，并与其他相关记录综合对比，建立了该地区全新世以来的年代框架。使用粒度组合特征以及磁化率为环境代用指标，获取了该地区约6 000 cal yr BP以来的气候环境变化信息。经过分析与对比，认为该区自中全新世以来，经历了暖干-凉湿-温湿三个气候环境变化阶段。在晚全新世中国南方地区气候（尤其是降雨量）发生了重要的变化，这与北半球太阳辐射减弱，气温降低，亚洲季风减弱，降雨带南移有着一致的对应关系，同时还很可能与这一时期厄尔尼诺—南方涛动活动加强有着紧密的联系。

关键词：粒度；磁化率；全新世；古气候；珠江三角洲

Correction of seabed layer thickness in processing subbottom profile data

WANG Fang-qi, QI Fa-qing, HU Guang-hai, DONG Li-feng, TAO Chang-fei

The First Institute of Oceanography, SOA, Qingdao 266061, *Shandong province, China*

Abstract: The subbottom profiling is an important means of marine engineering survey, hazardous geology study and continental shelf scientific research. The accuracy of subbottom profile data interpretation has a direct impact on the research and investigation results. Because some of profilers' transducer and hydrophone are separately installed, when the survey area is very shallow, distortion of shallow layers will be caused if it is seen as a self-excited and self-collected single-channel seismic system. According to the principle of subbottom profiler, the distortion correction formula is deduced and analyzed, providing actual value to using C-View software to interpret such subbottom profile data more accurately. In addition, the seabed sediments sound velocity is one of the key parameters when acquiring and processing the subbottom profile data. On the basis of comparing some sound velocity forecasting empirical equations, the LU Bo's equation was considered the most appropriate to predict the seabed sediments, sound velocity at near-shore of China. In a survey of an artificial island site, the LU Bo's equation and the porosity data obtained from geological drilling were utilized to predict the sediments sound velocity, and the sound velocity structure profile was plotted, which was applied in processing the subbottom profile data of the artificial island investigation. The method of using porosity data to predict sediments sound velocity in processing subbottom profile data can improve the interpretation accuracy and it's of practical significance.

Keywords: subbottom profile; layer thickness correction; sound velocity forecasting equation; porosity

1 Introduction

The subbottom profiling is an important geophysical method based on water-acoustics and geo-acoustics, which can efficiently detect the structure and construction of submarine sediments without stopping the ship. With advances of marine scientific research, large-scale development of marine oil and gas resources, construction

Received on October 25, 2011

Corresponding author: sdhdwfq0317@163.com

of more and more marine engineering projects and geologic hazards research, the subbottom profiling has been more and more widely used because of not only its high sensitivity and resolution but its continuity and the ability of quickly finding out the underwater geologic formation characteristics and distribution.

The subbottom profiler can be divided into two types according to the combination of transducers and hydrophones: integration type and separation type. The former's transducer and receiver are combined into one (self-excited and self-receiving), which are contained in a common box and approximately in the same location, such as SES-2000, ChirpIII, et al. The latter's transducer and receiver is usually separately installed by 4 - 10 m in horizontal to avoid the wake and mechanical noises, such as AAE CSP2000, C-Boom, et al. To the subbottom profiler of separation type, because the acoustic signal are not a vertical path to go, but an oblique path, and the incidence angle and reflection angle is not zero, and it can only be treated as a system of self-excited and self-receiving in very deep water; When in shallow water, the incidence angle and reflection angle are very large and the profiler cannot be treated as a system of self- excited and self-receiving any more. In this case, the travel time interpreted from the profile is much larger than the case of vertical launch and vertical receive so that the distortion of shallow layer will be caused. Therefore, we must find an efficient method to correct the layer thickness [1, 2].

When acquiring and processing the subbottom profile data, to determine the sound velocity of seabed sediments is a key problem. What we want to obtain is the arrival time of the reflected sound signal from the acoustical interface, and if the velocity of sediments layers can't be approximately determined, we can't acquire their real thicknesses. Usually a constant sound velocity value will be used according to experience data, for example, generally 1 600 m/s in the Bohai Sea. However, due to the complexity of actual structure of seabed sediments, the velocity is not a constant at all and there will be an error added up to the layer thickness in interpreting the profile data. Therefore, we must find out the real distribution of sediments sound velocity to correct the layer thickness.

Based on the principle of subbottom profiler, the factors leading to the distortion of seabed sediments for the above points were analyzed and the corresponding correction methods were proposed, which were successfully applied to solve practical projects and were proved to be right and efficient.

2 Distortion and correction of shallow stratigraphic thickness

2.1 Distortion of shallow layers thickness

When the distance (d) between the profiler's transducer and hydrophone is very large and the sea water is very shallow, the incidence angle (i) will be very large and the real path ($|AK_1|+|K_1S|$) of sound waves will be very different from the vertical path ($|PK_1|$). There will be a large deviation between the obtained layer thickness and the real case, and then the distortion will occur.

Assuming that the real path of sound wave is s_t, the vertical two-way path is s_v, and the distortion of propagation medium is defined as: $\Delta s = s_t - s_v$, and the distortion rate is as follows:

$$D = \frac{\Delta s}{s_v} = \frac{s_s - s_v}{s_v} \tag{1}$$

From the formula (1) it can be seen that the larger D value indicates the larger deviation between the real path and vertical two-way path of sound wave, and the larger deviation from the real seabed layers thickness.

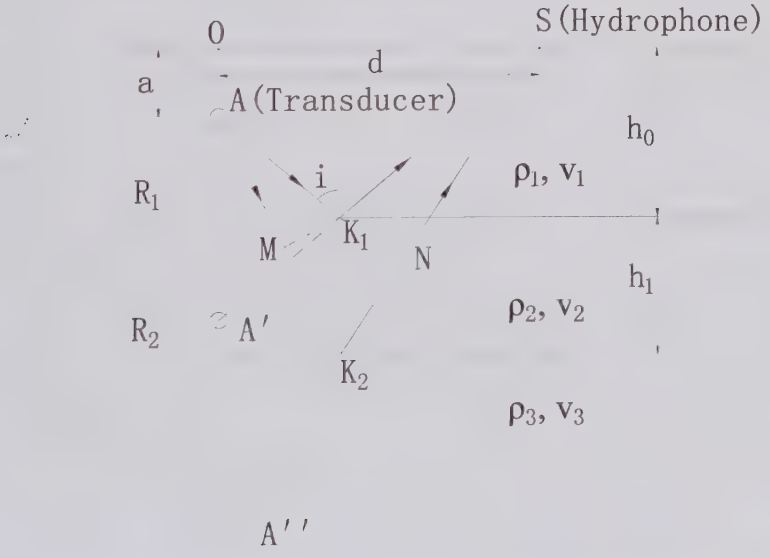

Fig. 1 Sound waves propagation path of subbottom profiler

2.2 The correction method of distortion

The C-View software is developed by C-Products Company of Hong Kong. It has

been widely used in acquiring and processing the subbottom profile data. When the C-View software is used to interpret the subbottom profile data, usually the seafloor boundary is tracked firstly, then the stratigraphic interface boundaries are depicted, as a result that the profile data obtained are calculated based on the seafloor depth. From the profile, the seafloor depth (H_0) can be obtained directly, and then the underlying seabed layers, boundaries are depicted and the layer depth values are calculated: $H_{0(1)}$, $H_{0(2)}$, $H_{0(3)}$, ..., $H_{0(n)}$.

In Fig. 1, $|AM|=|AK_1|$, $|SN|=|SK_1|$, and the first layer depth is h_1, then, $h_1=|K_1K_2|$, $H_0=\frac{|AK_1|+|K_1S|}{2}$,

$$H_{0(1)}=\frac{|AK_2|+|K_2S|}{2}-H_0=\frac{|AK_2|+|K_2S|}{2}-\frac{|AK_1|+|K_1S|}{2}=\frac{|MK_2|+|NK_2|}{2}<|K_1K_2|=h_1,$$

also that is, $H_{0(1)}<h_1$.

It can be seen that the directly calculated depth from the profile is smaller than the real layer depth, because while the software is calculating, the uncorrected seafloor depth is subtracted, which is larger than the real seafloor depth. That is caused by the C-View software data processing principle. The seafloor depth distortion is transmitted to all the underlying layers, depths while calculating (the layer depth distortion caused by this is called genetic distortion). Because of the genetic distortion, the directly calculated depth from the profile is smaller than the real layer depth. Actually the directly interpreted depth from the profile is a result of the double impacts of layer distortion and seafloor depth genetic distortion.

In the first reflection interface, the real travel time is: $|AK_1|+|K_1S|=|A'S|=2H_0$,

In the right-angled triangle $OA'S$, $2h_0-a=\sqrt{4H_0^2-d^2}$, then:

$$h_0=0.5a+0.5\sqrt{4H_0^2-d^2} \quad (2)$$

The formula (2) is the seafloor depth correction formula. It can also be said that appropriate seafloor depth can be obtained from the subbottom profile if accurate instrument placement parameters are input.

In the second reflection interface, the real travel time is: $|AK_2|+|K_2S|=|A'S|=2H_{0(1)}+2H_0$,

In the right-angled triangle $OA''S$, $2(h_0+h_1)-a=\sqrt{4(H_{0(1)}+H_0)^2-d^2}$, then:

$$h_1 = 0.5a + \sqrt{4(H_{0(1)} + H_0)^2 - d^2} - h_0$$

Similarly, all the underlying layer depth values are available:

$$h_i = 0.5a + \sqrt{4(H_{0(i)} + H_0)^2 - d^2} - h_0, \text{ where } i = 1, 2, \cdots\cdots, n \quad (3)$$

The formula (3) is the formula for sediments, layer thickness correction. The layer depth values calculated are based on the seafloor depth.

2.3 Application example

The First Institute of Oceanography of SOA had conducted an oilfield investigation using a subbottom profiler (C-Boom), and meanwhile a borehole (30 m) in the center of the oilfield was drilled. During the subbottom profile investigation, the research ship had passed the center well twice: the first was from west to east and the second was from south to north. The real-time seafloor depth was 1.4 m - 3.5 m. The horizontal distance between the transducer and hydrophone was about 4.8 m. Because the seafloor depth was too small, the distortion of shallow seabed layer thickness was very obvious.

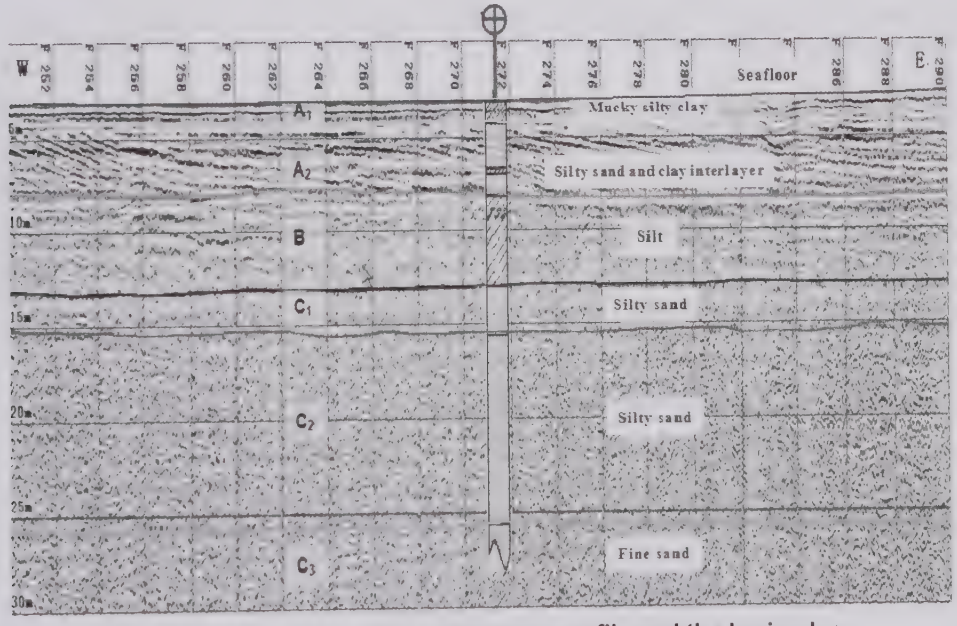

Fig. 2 Comparison of the subbottom profile and the boring log

The uncorrected interpreted geological profile (Fig. 3a) can be obtained from the measured original subbottom profile (Fig. 2). As can be seen from the Fig. 3a, there is an obvious deviation between the geological profile and the boring log, and all the layer interface boundaries cannot match well. The layer distortion rate and the corrected layer depth values can be calculated using formula (1) and formula (3), which are listed in the

Tab. 1. While the real seafloor depth is 1.96 m, the seafloor depth distortion rate (58.2%) is so large that correction calculations have to be conducted.

By inputting the real instrument placement parameters (a and d), the subbottom profile data can be corrected using formula (3) and each layer depth can be corrected to be right. As a result, the real geological profile depicted according to the corrected data can match with the boring log pretty well (Fig. 3b).

Tab. 1 Comparison of uncorrected and corrected layer depths

Interface	Uncorrected depth / m	Corrected depth / m	Error / m	Distortion rate
Seafloor	3.10	1.96	1.14	58.2%
A_1	1.10	1.48	0.38	25.7%
A_2	4.90	5.67	0.77	13.6%
B	9.90	10.81	0.91	8.4%
C_1	12.60	13.55	0.95	7.0%
C_2	22.90	23.93	1.03	4.3%

3 Correction of layer thickness related to the sound velocity

The sound velocity of seabed sediments has a relationship with sediments' physical and mechanical parameters. Since the 1950s, some meaningful results have been made about seabed sediments acoustical and physical characteristics at home and abroad [3-11]. Hamilton (1956, 1980), Anderson (1974), ZHOU Zhi-yu and MENG Jin-sheng (1983), Orsi and Dunn (1990), LU Bo et al (1995, 2006) and TANG Yong-lu (1998) established empirical equations for different sea areas based on the relationship between sound velocity and porosity data. In the investigation of marine oil platforms and artificial island sites, generally engineering geological drilling and subbottom profiling are implemented at the same time, so the porosity is an accessible parameter. Therefore, it is feasible that the sound velocity, which can be predicted by using seabed sediments' porosity data, is used to interpret subbottom profile data more accurately.

3.1 Seabed sediment sound velocity model

Seabed sediments are made up of two-phase media: solid particles and liquid seawater. Because of the difference of porosity, moisture, density, grain size and stacking mode of solid particle, et al., there may be high sound velocity sediment layers or low sound velocity sediment layers. After analyzing a large number of sediments data, Hamilton (1980) summarized two more kinds of sediments, sound velocity structure model:

high sound velocity model and low sound velocity model. And he pointed that in deep sea areas, low sound velocity model commonly existed, and in continental shelf, high sound velocity model was generally found. By studying a large number of seabed sediment data from sea area of China, LU Bo et al. (1995) thought there were not only two sound velocity models in continental shelf area of sea area in China. They established three kinds of sediment sound velocity structure models, which represented the basic characteristics of sediments, sound velocity structure in the offshore area of southeast China (Fig. 4).

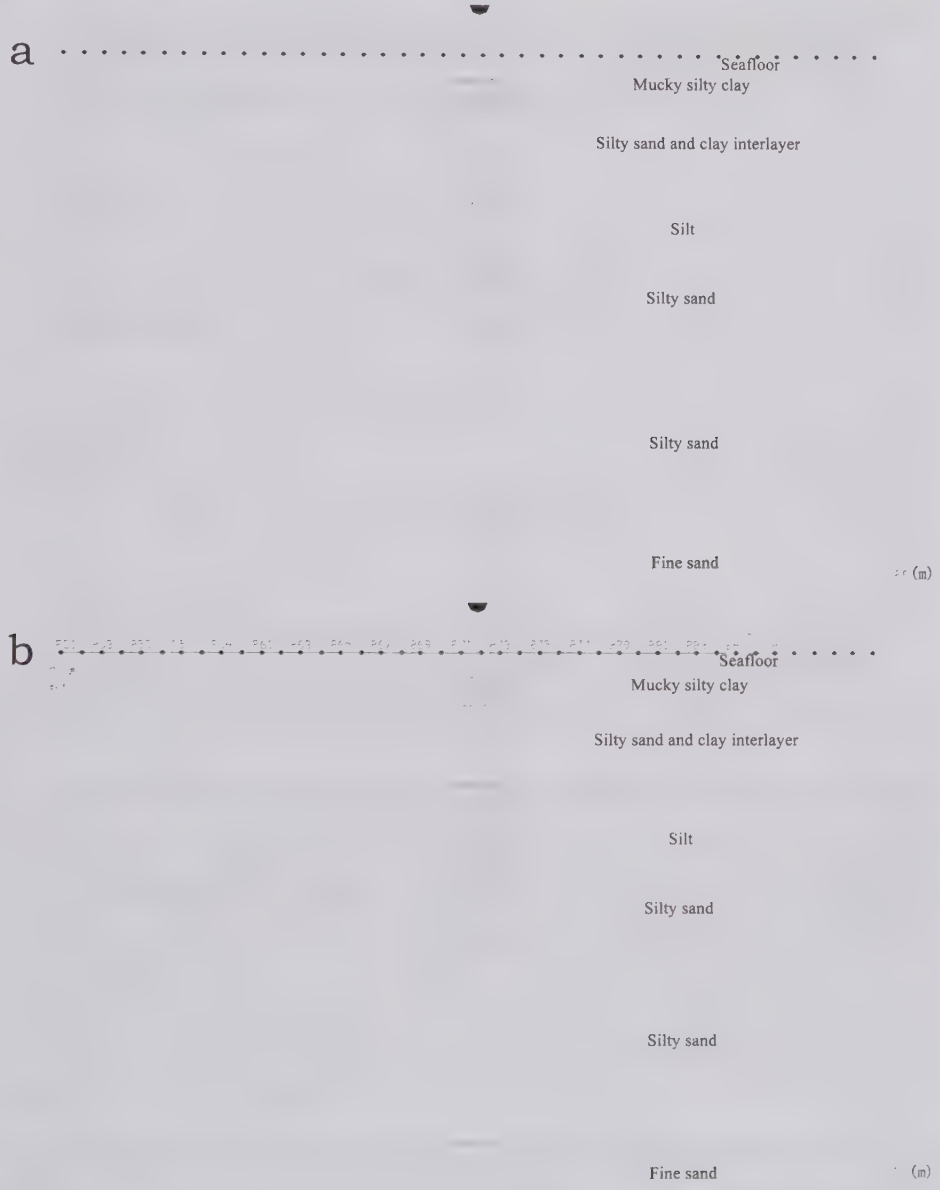

Fig. 3 Comparison of uncorrected (a)/corrected (b) geological profile and the boring log

Although these three models don't give us an accurate sound velocity calculation equation of seabed sediments, they are of great instructive significance and reference value to constructing detailed profile of sediments, sound velocity. They have the following meaning: 1) the sound velocity of seabed sediments is not a constant, and its structure is very complex, and the difference among the seabed layers may be significant; 2) the sound velocity of loose seabed sediments maybe lower than that of seawater; 3) the low sound velocity not only exists in the fluid mud on the seafloor surface, but in the interlayer of some high sound velocity sediments.

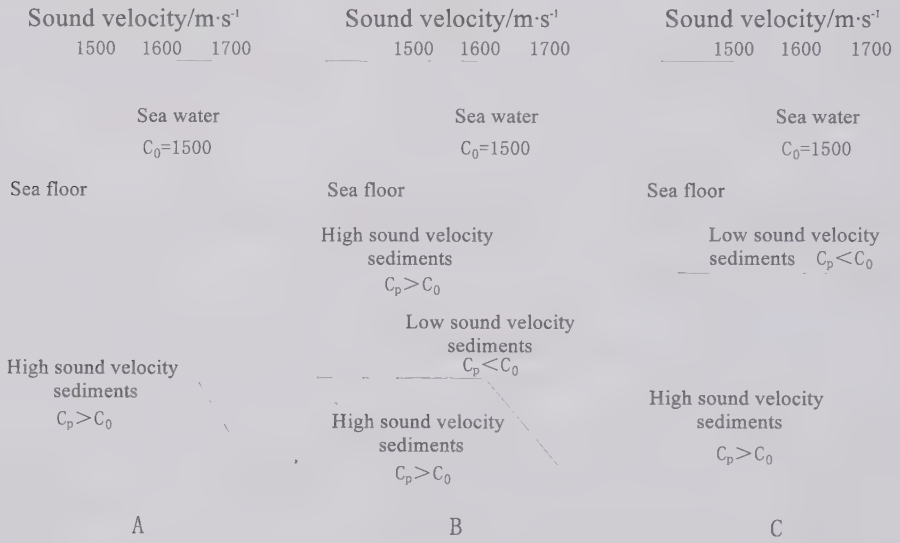

Fig. 4 Three seabed sediments' sound velocity models (by LU Bo)

3.2 Sound velocity profile for correcting the layer thickness

According to LU Bo et al. (1994), in the continental shelf of the southeast China, the seabed sediments' sound velocities vary greatly: 1 336 m/s - 1 885 m/s. While processing subbottom profile data, the sediments' sound velocity used is usually 1 600 m/s. Then the 1ms travel distances corresponding 1 336 m/s, 1 600 m/s, 1885 $m \cdot s^{-1}$ are respectively 1.336 m, 1.600 m, 1.885 m. Obviously, the difference is so large that greatly reduces the subbottom profile data interpretation accuracy, therefore, the layer depths must be corrected. In this paper, an artificial island site subbottom profiling is taken for an example to study the layer thickness correction related to the seabed sediments, sound velocity.

Obviously, the sediment sound velocity structure models (Fig. 4) cannot meet the requirement of subbottom profile correction, and more realistic sound velocity values corresponding to the seabed layers must be given. The seabed sediments' sound velocity is affected by many factors: density, porosity, moisture (water content), grain size, pressure,

temperature, burial depth and geologic age and so on. After plenty of research to the seabed sediments geophysics, most scholars at home and abroad have come to a common conclusion that the porosity is the best parameter to predict the seabed sediments' sound velocity. Here are 6 sound velocity prediction empirical equations based on the variable porosity.

Hamilton [3]:

$$C_p = 2455.9 - 21.716n + 1.126n^2 \tag{4}$$

Anderson [5]:

$$C_p = 2506 - 27.58n + 0.1868n^2 \tag{5}$$

ZHOU Zhi-yu and MENG Jin-sheng [6]:

$$C_p = 962 + C_0 - 27.58n + 0.1868n^2 \tag{6}$$

Orsi and Dunn [7]:

$$C_p = 2527.4 - 27.132n + 0.1782n^2 \tag{7}$$

TANG Yong-lu [10]:

$$C_p = 942 + C_0 - 25.02n + 0.156n^2 \tag{8}$$

LU Bo et al. [9]:

$$C_p = 2369.07 - 25.53n + 0.185n^2 \tag{9}$$

Where C_p is the sound velocity of seabed sediments, n is the porosity of sediments, C_0 is the sound velocity of sea water near the seafloor.

Because of limitations of measurement data and study sea area, each of above equations has a certain regional applicability. The study sea areas of equation (4), (5) and (7) are in abroad. The equation (6) is only an extended conclusion based on the introduction of seawater sound velocity C_0. The equation (8) is for the South China Sea. The equation (9) is a summary based on a large number of data from the southeast sea area of China, and it is applicable to most of the southeast sea area of China. In this paper, the equation (9) is selected to conduct a trial for the layer thickness correction related to sound velocity based on an artificial island project in Bohai Sea.

The Fig. 5 is the composite drilling log of borehole (L_3) for an artificial island geological investigation in Bohai Sea. The Tab. 2 is the laboratory soil testing data of the core. In the study, firstly the sediments are divided into 9 layers and all the porosity data within the scope

of each layer is extracted. Then, the equation (9) is applied to calculate sound velocity of each samples and the average sound velocity of each layer. Lastly, the sound velocity profile (Fig. 6) is plotted and is used to correct the layer thicknesses of 9 layers.

Because of the discretion of the porosity n from the geological drilling data and the dependence to the porosity of sound velocity calculation, the density of sound velocity calculated is determined by the porosity. The more dense the sound velocity is, the more detailed the sound velocity profile is, and the more close to the reality the average sound velocity of each layer is.

Tab. 2 **Laboratory soil testing data of an artificial island from Bohai Sea**

No.	Depth / m	Moisture / %	Density / g/m^3	Gravity	Porosity / %
L3-1	2.6-2.8	24.6	2.01	2.70	40.3
L3-2	4.2-4.4	27.6	1.97	2.72	43.2
L3-3	5.1-5.3	27.2	1.98	2.70	42.3
L3-4	6.2-6.4	17.7	1.97	2.70	38.0
L3-5	11.5-11.7	19.3	2.00	2.70	37.9
L3-7	15.1-15.3	17.6	2.03	2.70	36.1
L3-8	15.5-15.7	30.5	1.94	2.72	45.3
L3-9	17.2-17.4	35.1	1.82	2.72	50.5
L3-10	17.5-17.7	40.3	1.82	2.73	52.5
L3-11	17.7-17.9	37.0	1.83	2.75	51.4
L3-12	17.9-18.1	32.5	1.86	2.73	48.6
L3-13	18.6-18.8	23.3	1.97	2.69	40.6
L3-14	19.5-19.7	32.9	1.85	2.72	48.8
L3-15	20.0-20.2	35.0	1.87	2.74	49.4
L3-18	25.0-25.2	17.9	1.98	2.70	37.8
L3-21	27.0-27.2	18.6	2.03	2.69	36.4
L3-24	31.7-31.9	18.6	2.03	2.70	36.6
L3-25	34.5-34.7	21.2	1.97	2.69	39.6
L3-28	37.7-37.9	21.5	1.98	2.68	39.2
L3-29	40.2-40.4	19.5	1.99	2.70	38.3
L3-30	40.8-41.0	23.4	2.00	2.68	39.5
L3-31	41.4-41.6	19.3	1.94	2.68	39.3
L3-32	41.7-41.9	17.4	1.97	2.68	37.4
L3-34	45.8-46.0	20.1	2.01	2.68	37.6
L3-35	47.9-48.1	19.4	1.94	2.68	39.4
L3-36	48.8-49.0	19.0	1.97	2.68	38.2
L3-37	49.7-49.9	18.6	2.00	2.68	37.1

In the acquisition of subbottom profile data, the profiles are obtained in two modes: two-way travel time profile and depth profile. In fact, the depth profile is collected in order to make an overview of the sediments structure and it is obtained from the data acquiring software by time-depth conversion based on the two-way travel time and an preliminary

assuming sound velocity. Therefore, to the two-way travel time profile the depth can be calculated by one-way travel time and sound velocity profile; to the depth profile the one-way travel time must firstly be calculated according to the preliminary assuming sound velocity and then the depth can be calculated by one-way travel time and sound velocity profile either.

The Tab. 3 (Corrected depth) is the calculation result of the subbottom profile based on the sound velocity profile we plotted. As can be seen from the table, the average sound velocity of silty clay is smaller than the silty sand and fine sand, and the difference is about 80 - 100 m/s. By comparing the layer depths between those corrected before and after, the minimum deviation of layer depths is -0.1 m, and the maximum deviation is -1.3 m. It can be seen that the deviation is so large that must be corrected to ensure the interpretation accuracy of the subbottom profile data.

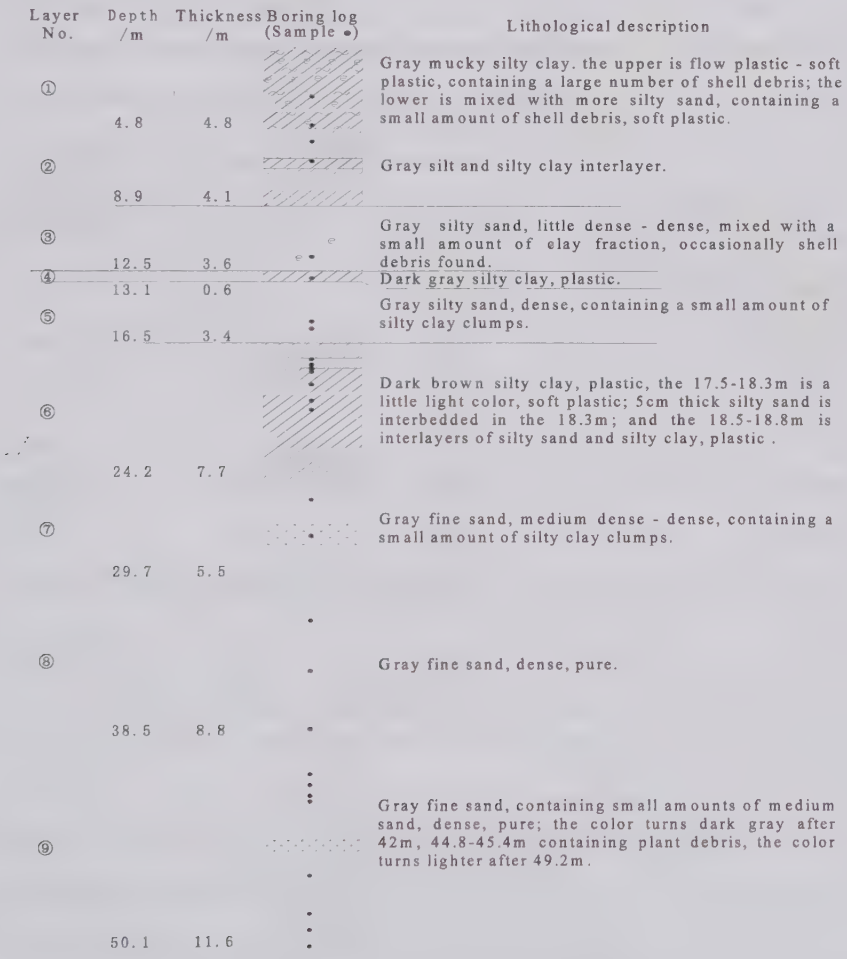
Layer No.
Depth /m
Thickness /m
Boring log (Sample •)
Lithological description
①
4.8
4.8
Gray mucky silty clay. the upper is flow plastic - soft plastic, containing a large number of shell debris; the lower is mixed with more silty sand, containing a small amount of shell debris, soft plastic.
②
8.9
4.1
Gray silt and silty clay interlayer.
③
12.5
3.6
Gray silty sand, little dense - dense, mixed with a small amount of clay fraction, occasionally shell debris found.
④
13.1
0.6
Dark gray silty clay, plastic.
⑤
16.5
3.4
Gray silty sand, dense, containing a small amount of silty clay clumps.
⑥
24.2
7.7
Dark brown silty clay, plastic, the 17.5-18.3m is a little light color, soft plastic; 5cm thick silty sand is interbedded in the 18.3m; and the 18.5-18.8m is interlayers of silty sand and silty clay, plastic .
⑦
29.7
5.5
Gray fine sand, medium dense - dense, containing a small amount of silty clay clumps.
⑧
38.5
8.8
Gray fine sand, dense, pure.
⑨
50.1
11.6
Gray fine sand, containing small amounts of medium sand, dense, pure; the color turns dark gray after 42m, 44.8-45.4m containing plant debris, the color turns lighter after 49.2m.

Fig. 5 Composite boring log of borehole (L3)

Fig. 6 Seabed sediment sound velocity profile of the artificial island site

Tab. 3 Comparison of stratum depth before and after correction

Layer No.	Stratum name	Sound velocity / m/s	Single travel time /ms	Uncorrected depth /m	Corrected depth /m	Error /m
①	Mucky silty clay	1 626	2.952	4.7	4.8	-0.1
②	Silt and silty clay interlayer	1 643	5.447	8.7	8.9	-0.2
③	Silty sand	1 667	7.607	12.2	12.5	-0.3
④	Silty clay	1 626	7.976	12.8	13.1	-0.3
⑤	Silty sand	1 640	10.049	16.1	16.5	-0.4
⑥	Silty clay	1 566	14.966	23.9	24.2	-0.3
⑦	Fine sand	1 677	18.246	29.2	29.7	-0.5
⑧	Fine sand	1 661	23.544	37.7	38.5	-0.8
⑨	Fine sand	1 662	30.523	48.8	50.1	-1.3

4 Conclusion and prospect

Because the exciting transducer and the receiving hydrophone of subbottom profiler are installed separately, in shallow water, the layer depth of seabed sediments will be distorted. The factors affecting the distortion include: the horizontal distance (d) between transducer and hydrophone and seawater depth of working sea area. The larger the distance d is, the more serious the distortion and the smaller the distance d is, the less

serious the distortion is; the larger the seawater depth is, the more serious the distortion is, the smaller the seawater depth is, the less serious the distortion is. Generally speaking, when the seawater depth is smaller than 15 m, the subbottom profile data must be corrected. In this paper, the equation (2) and (3) are deduced based on the working principle and they are of important guiding significance and reference value to process the subbottom profile data.

The seabed sediment sound velocity is one of the key parameters in acquiring and interpreting the subbottom profile data. On the basis of comparing some sound velocity forecasting empirical equations, the LU Bo's equation was considered the most appropriate to predict the seabed sediments sound velocity in the near-shore area of China. In the survey of an artificial island site, the porosity data obtained from geological drilling was utilized to predict the sediments sound velocity, and the sound velocity profile was drawn, which was applied in interpreting the subbottom profile data. The method of utilizing porosity to predict sound velocity in processing subbottom profile data can improve the interpretation accuracy and it's of important practical significance.

The sound velocity profile constructed based on the sediment porosity data is a layered structure. But in fact, the sound velocity distribution in sediments is very complex. Even within the same sedimentary layer, the sound velocity is changing with the depth increasing (generally increasing with the depth increasing affected by the pressure). Therefore, the layered structure cannot reflect the real sound velocity structure of the seabed sediments, and for studying the real continuous structure of sound velocity, our future efforts are needed.

References

[1] LIU J J, QI G J. Skewness and Correction Method of the Subbottom Profile from very Shallow Sea Water Zone [J]. Marine Geology and Quaternary Geology, 1996, 16(1): 111 - 116.

[2] ZHAO T H, ZHANG Z X, XU F. Analysis of Typical Problem for Shallow Acoustic Surveying in the Shallow Waters [J]. Computing Techniques for Geophysical and Geochemical Exploration, 2002, 24(3): 215 - 219.

[3] Hamilton E L, George S, Menard H W, et al. Acoustic and Other Physical Properties of Shallow-Water Sediments off San Diego [J]. Acoustical Society of America, 1956, 28(1).

[4] Hamilton E L. Geoacoustic Modeling of the Sea Floor [J]. Acoustical Society of America, 1980, 68: 1 313 - 1 340.

[5] Anderson R S. Statistical correlation of physical properties and sound velocity in sediments [A]. Physical of Sound in Marine Sediments [C]. NY: Plenum Press, 1974, 481 - 518.

[6] ZHOU Z Y, DU J C, ZHAO G C, et al. Measurement of seafloor sound velocity vertical distribution of South China Sea and Yellow Sea [J]. Acta Oceanologica Sinica, 1983, 5(5): 543 - 552.

[7] Orsi T H, Dunn D A. Sound velocity and related physical properties of fine-grained abyssal sediments from the Brazil Basin (South Atlantic Ocean) [J]. Acoustical Society of America, 1990, 88(3): 1 536 - 1 543.

[8] LU B. Model of sound velocity structure in seawater-sediments [J]. Marine Science Bulletin, 1995, 14(2): 42 - 47.

[9] LU B, LI G X, SUN D H, et al. Acoustic-physical properties of seafloor sediments from near shore southeast China and their correlations [J]. Journal of Tropical Oceanography, 2006, 25(2): 12 - 17.

[10] TANG Y L. The relationship between porosity of sea bed sediment and sound velocity [J]. Acta Oceanologica Sinica, 1998, 20(6): 39 - 43.

[11] LU B, LIANG Y B. The statistical correlation between marine sediments physical parameters and sound velocity along the southeast sea of China [J]. Science in China (B), 1994, 24(5): 556 - 560.

浅地层剖面资料处理中的地层厚度校正

王方旗，亓发庆，胡光海，董立峰，陶常飞

（国家海洋局 第一海洋研究所，山东 青岛 266061）

摘 要：浅地层剖面测量是海洋工程勘察、灾害地质调查和大陆架海洋地质科学研究的重要手段，资料解译的准确程度将对地质调查和研究成果的可靠性造成直接影响。由于发收分置型浅地层剖面仪的激发装置与接收装置是分开的，当调查区域的水深过浅时，将其近似为自激自收的单道地震系统会导致地层的畸变，水深越浅地层畸变率越大。根据浅地层剖面仪的基本原理，推导出了浅部地层厚度畸变校正公式，为用 C-View 软件更准确地解译此类浅地层剖面资料提供了参考。海底沉积物的声速直接影响浅地层剖面地层厚度解译的准确性，利用卢博等建立的适用于中国东南近海的声速经验公式，在某人工岛构造调查中，根据地质钻孔获取的孔隙度参数计算各沉积层的平均声速，建立相应的声速结构剖面，对地层厚度进行校正，取得较好的效果，用孔隙度预测声速的方法参数容易获取，能够提高浅地层剖面资料的解译精度，使地层的厚度更接近于实际，具有一定的实用意义。

关键词：浅地层剖面；地层厚度校正；畸变率；声速预测方程；孔隙度

Marine Science Bulletin

Marine Science Bulletin publishes papers on marine science and technology including physical oceanography, chemical oceanography, marine biology, marine geology, environmental oceanography, estuarine & coastal sciences, marine technology, digital ocean, coastal zone management, ocean engineering, marine economics, etc., and aims to promote international academic exchange.

Editor-in-Chief: XU Sheng (徐　胜)
Associate Editor-in-Chief: LI Dong-xu (李东旭)　XUE Hui-feng (薛惠芬)
Executive Editor: QIU Wen-jing (邱文静)　LI Xue (李　雪)　YANG Rui (杨　瑞)
LI Xiao-guang (李晓光)　DONG Yi (董　艺)　YUAN Ze-yi (袁泽轶)
English proofed by: WANG Qi (王　琦)

Semi-annually (started in 1999, sum 28)
Publication date: May 15th and Oct. 15th

Marine Science Bulletin **(Vol. 14, No. 2, Oct. 2012)**

Responsible Institution:
State Oceanic Administration of China
Sponsored by:
National Marine Data and Information Service
Edited by:
Office of Marine Science Bulletin (English edition)
Printed by:
Printery of National Marine Date and Information Service

Published by:
Office of Marine Science Bulletin (English edition)
E-mail: msb@mail.nmdis.gov.cn
Tel: (022) 24011287
Address: 93 Liuwei Rd., Hedong District, Tianjin 300171, China

---

ISSN1000-9620
CN12-1271/N

Price: $ 30.00 / ￥40.00 Per year

ISSN 1000-9620

02>